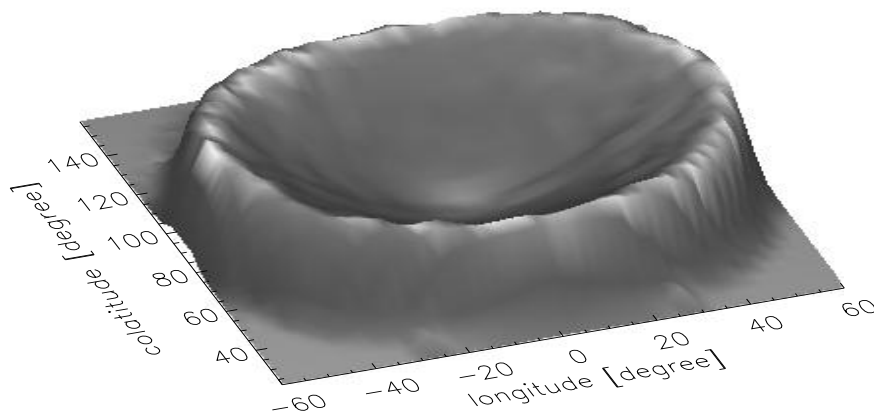


Diss. ETH No. 15514

# Interplay of Solar Oscillation Modes and Noise in Helioseismic Power Spectra



**Richard Wachter**

2004

ETH Diss. 15514

# **Interplay of Solar Oscillation Modes and Noise in Helioseismic Power Spectra**

A thesis submitted to the

**SWISS FEDERAL INSTITUTE OF TECHNOLOGY  
(ETH)  
ZÜRICH**

for the degree of

**Doctor of Natural Science**

presented by

**Richard Wachter**

Dipl. Phys., Universität Augsburg

born 19 June 1973

from Germany

accepted on the recommendation of

Prof. Dr. J. O. Stenflo, examiner

Prof. Dr. Werner Schmutz, co-examiner

Dr. Alexander Kosovichev, co-examiner

2004

**Cover illustration:** Estimator for the local noise level in Doppler velocity at  $78 \mu\text{Hz}$  as measured by the MDI instrument. From the center to the top, the crater-like structure reflects the line-of-sight component of the predominantly horizontal supergranular velocities. The outer decay is determined by instrumental effects and data processing.

# Acknowledgement

First of all I would like to thank Jan O. Stenflo for accepting me as a Ph.D. student at his chair and providing me the framework to prepare this thesis. My advisors Werner Schmutz and Claus Fröhlich at the Davos Observatory introduced me to the subject and to the community of helioseismologists, and were always helpful during my dissertation. As a member of the PHOEBUS team, I learned a lot about solar physics, and I had the opportunity to meet interesting people. I would also like to thank the GOLF team, who provided me with a GOLF time series. The staff members of the Davos Observatory, who were working on quite different fields in solar and atmospheric physics helped me to broaden my view and gave me insight into various kinds of research. Special thanks go to Margit Haberreiter, who performed the radiative transport calculations described in Section II.6.

During three months in 2001, I had the opportunity to visit and work with the helioseismology group at Stanford University. It was during this time that essential ideas for this thesis arose. Many discussions with the various members of the group helped me to get familiar with the data. I would like to express special thanks to Phil Scherrer, Jesper Schou, and in particular, to Sasha Kosovichev, my wise and patient teacher in helioseismology ever since.

During two visits I had the pleasure to meet the helioseismologists of the Tashkent Astronomical Institute, Uzbekistan, in the frame of the SCOPES project of the Swiss National Science Foundation. This was a unique experience. Thanks to everyone who helped me survive in Tashkent (a lot of people were involved in this project).

For proofreading this thesis, I would like to thank Alexander Serebryanskiy, Martin Maurer, and James Goodell (Chapter 3).

This research was supported by the Swiss National Science Foundation grant number 20-65134.01.



# Zusammenfassung

Helioseismologie untersucht akustische Eigenschwingungen und stehende Schwingungen im Inneren der Sonne. Geschwindigkeiten und Intensitäten oszillieren den Schwingungsperioden entsprechend an der Sonnenoberfläche. Viele weitere Prozesse hinterlassen ihre Spuren in den Spektren. Die bedeutendsten darunter sind Granulation, Supergranulation und Aktivitätsrauschen. Die vielseitigen Wechselwirkungen von solaren Eigenschwingungen und dem Hintergrundrauschen bei den jeweiligen Frequenzen stehen im Zentrum dieser Arbeit.

G-Moden sind stehende Wellen in der Strahlungszone der Sonne. Ihre äussere Grenze ist tief im Sonneninneren, so dass G-Moden in einer Kavität sehr hoher Güte eingeschlossen sind. G-Moden sind deshalb extrem langlebig: Ihre Lebenszeit übersteigt vermutlich die Länge aller vorhandenen helioseismologischen Zeitreihen. Wegen ihrer extrem kleinen Amplituden an der Photosphäre konnten sie bislang nicht detektiert werden.

Durch ein einfaches Modell der räumlichen Variation des supergranularen Rauschens auf der beobachteten Sonnenscheibe lässt sich das Signal-Rausch-Verhältnis optimieren, wie in dieser Arbeit gezeigt wird. Da auch in diesen optimierten Spektren keine signifikanten Peaks identifizierbar sind, kann eine genaue obere Grenze für die Amplitude von G-Moden angegeben werden. Es wird gezeigt, dass diese obere Grenze nicht allein von der Frequenz abhängt, sondern auch von der Ordnung der der Eigenschwingung zugeordneten Kugelflächenfunktion. Weiter wird gezeigt, dass eine moderate räumliche Auflösung der Beobachtungsinstrumente eine mögliche Detektion der G-Moden erleichtert. Die Kenntnis ihrer Eigenfrequenzen wäre von grosser Bedeutung für eine exakte Bestimmung der thermodynamischen Verhältnisse im energiereicheren Kern der Sonne.

Granulation ist die wahrscheinliche Anregungsquelle der akustischen Schwingungen (P-Moden). Simulationen der solaren Granulation von Stein & Nordlund (2001) zeigen, dass die Anregung in schnellen Abwärtsströmungen im zwischengranularen Bereich konzentriert ist. Granulare Abwärtsströmungen sind stark turbulent, während die granulare Aufwärtströmung weitgehend laminar erfolgt. Die gleichen Simulationen zeigen, dass die Quelle leicht unterhalb des photosphärischen Niveaus liegt, dass

aber ein damit korrelierter Prozess an der Oberfläche sichtbar ist. In P-Moden-Spektren wird dieser Prozess als korreliertes Rauschen sichtbar. Durch helioseismologische Datenanalyse wird gezeigt, dass der Schätzwert für die Amplitude und Phase des korrelierten Rauschens empfindlich vom Modell für die Resonanz abhängt. Bei der Analyse von Daten des Michelson Doppler Imagers (MDI) wird angenommen, dass die Oszillationsgleichungen bei Berücksichtigung des Strahlungstransports in der Diffusionsnäherung P-Moden niedriger Frequenz ausreichend gut beschreiben, um eine physikalisch glaubhafte Abschätzung für das korrelierte Rauschen zu erhalten. Bezogen auf den gesamten additiven Hintergrund liegt das korrelierte Rauschen für das Geschwindigkeitssignal demnach unter 2%, und zwischen 5% und 20% für das Intensitätssignal. Dieses Ergebnis ist qualitativ konsistent mit der Anregung in konzentrierten, isolierten Abwärtsströmungen. Die Tiefe der Anregung lässt sich hingegen nur unzureichend bestimmen. Die berechneten Spektren stimmen mit der Beobachtung überein, wenn sich eine Dipolanregung in beliebiger Tiefe unterhalb des photosphärischen Niveaus befindet, beziehungsweise eine Quadrupolanregung mindestens 120 km darunter liegt.

Um möglichst genaue Oszillationsspektren zu erhalten, wurde die Antwort des MDI auf Oszillationen der Sonne mittels Strahlungstransportrechnungen untersucht. Verglichen mit Modenprofilen, die man für einen vereinfachten Strahlungstransport in der Diffusionsnäherung erhält, zeigen die so gewonnenen Profile keine bedeutenden Änderungen in den Leistungsspektren der Intensitätszeitreihen, wie sie von Georgobiani, Stein & Nordlund (2003) vorgeschlagen wurden. Dadurch wird die Annahme bestärkt, dass in der Tat korreliertes Rauschen für die verschiedenen Asymmetrien von P-Moden Peaks in Intensitäts- und Geschwindigkeitsspektren verantwortlich ist. Kleine Änderungen in der gegenseitigen Phasenbeziehung von Intensitäts- und Geschwindigkeitssoszillationen, die sich durch eine sorgfältigere Behandlung des Strahlungstransports ergeben, können jedoch die Werte für die Amplitude des korrelierten Rauschens beeinflussen.

Pseudomodern sind auswärts propagierende akustische Wellen in der solaren Atmosphäre. MDI misst die Tiefe der Absorptionslinie: In diesen Messungen haben Pseudomodern eine aussergewöhnlich hohe Amplitude. Die Untersuchungen dieser Arbeit zeigen, dass diese möglicherweise durch den Strahlungstransport erklärbar ist. Korreliertes Rauschen hätte somit keinen wesentlichen Einfluss auf die Spektren der Absorptionslinientiefe. Sollte es gelingen, das helioseismische Spektrum bei hohen Frequenzen korrekt zu beschreiben, so könnte die Lage der gut sichtbaren Pseudomodernpeaks zur Bestimmung der Anregungstiefe herangezogen werden.

# Abstract

Helioseismology investigates acoustic modes and standing gravity waves in the Sun's interior. Various processes in the solar convection zone which are visible at the solar photosphere leave their traces in the observed helioseismic spectra. The most prominent of them are granulation, supergranulation, and solar activity noise. Various aspects of the complex interaction between the solar oscillations and the nonoscillatory background are the focus of this thesis.

G-modes are standing internal gravity waves in the radiative interior of the Sun. They are expected to live much longer than any available helioseismic time series, but due to their very small amplitudes on the photosphere they are buried in the supergranular noise and could not yet be detected. A new method for optimizing the signal-to-noise ratio, based on spatially resolved data, is given in this thesis. To do so, we model the spatial variation of the supergranular noise across the solar disk. We will show that the upper limit for a mode's amplitude depends not only on its frequency, but also on its angular degree and tesseral order. We also show that a low spatial resolution of the observing instruments increases the chance to detect low- $l$  g-modes in helioseismic data. Knowing their frequencies would be a crucial premise to determine the conditions in the Sun's energy generating core in greater detail.

Granular noise is presumably responsible for the excitation of p-modes. Simulations of Stein & Nordlund (2001) of the upper solar convection zone suggest that their excitation occurs in the rapid downdrafts of intergranular lanes, where turbulence is highly developed. The same simulation show that the excitation occurs slightly below the photosphere. Still, there are visible imprints of this excitation process from radiative cooling at the solar photosphere. In p-mode spectra, this imprint is perceivable as correlated noise. The amount of correlated noise can be different in velocity and continuum intensity spectra. It is shown that estimates of amplitudes and phases of this correlated noise depend crucially on the models for solar oscillations. Investigating medium- $l$  p-modes using data from the Michelson Doppler Imager (MDI), we assume that low frequency p-modes are described accurately enough by oscillation equations which include the radiative transfer in the diffusion approximation to infer reliable results for the correlated noise. In fractions of the entire additive background signal, the



correlated noise is below 2% in velocity, and between 5% and 20% in intensity spectra. This result is qualitatively consistent with an excitation in narrow isolated downdrafts in intergranular lanes. Our results confirm that the correlated photospheric signal is lowering the emitted intensity during the excitation events. The source location can be at any depth below the photosphere for a dipole source, but must be deeper than 120 km below the photosphere for a quadrupole source. A more accurate determination of the source depth is not possible with our analysis.

The MDI response to solar oscillations is examined in more detail through radiative transfer calculations for the Ni I absorption line at 6768 Å. Compared to intensity spectra obtained by including the radiative energy flux in the diffusion approximation, intensity spectra calculated with a radiative transfer code don't show significant modifications of mode peak asymmetries as suggested by Georgobiani, Stein & Nordlund (2003). Thus, correlated noise seems to be indeed responsible for the different mode asymmetry observed in velocity and intensity spectra. This strengthens the credibility of the results we obtained for the correlated noise. However, small phase differences between the calculated MDI-intensity and the calculated luminosity will probably modify the estimates for the fraction of correlated noise.

*High frequency interference peaks* or *pseudo-modes* are outward travelling acoustic waves in the solar atmosphere. They show particular high amplitudes in the spectra obtained from MDI measurements of the depth of the absorption line. We suggest that the high amplitudes can probably be explained by radiative transfer effects and that there is no strong influence of correlated noise on line depth spectra. This means that if the high frequency part of helioseismic spectra could be correctly described by theoretical models, the location of the pseudo-mode peaks could be used to infer the depth of the excitation source.

# Contents

<b>I</b>	<b>Introduction</b>	<b>1</b>
I.1	Oscillations of a Star . . . . .	2
I.2	Hydrodynamic Equations . . . . .	3
I.3	Equilibrium Equations . . . . .	4
I.4	Equations of Oscillation . . . . .	5
I.4.1	Perturbation Analysis . . . . .	5
I.4.2	Separation of Radial and Horizontal Part . . . . .	6
a)	Basic Structure of the Radial Equations . . . . .	7
I.5	Solar Models . . . . .	8
I.6	Adiabatic Oscillations . . . . .	10
I.7	Properties of the Solar Noise . . . . .	13
I.8	Observational Aspects . . . . .	15
I.8.1	Instruments . . . . .	15
a)	Whole Disk Measurements . . . . .	15
b)	Resolved Instruments . . . . .	16
I.8.2	Mode Leakage . . . . .	17
<b>II</b>	<b>Solar Noise and the Excitation of P-Modes</b>	<b>21</b>
II.1	Stochastic Excitation . . . . .	21
II.1.1	Statistics of the Spectra . . . . .	21
II.1.2	Turbulent Convection . . . . .	22
II.1.3	Seismic Events . . . . .	22
II.2	Theoretical Oscillation Spectra . . . . .	23
II.2.1	Potential Well Model . . . . .	24
II.2.2	Adiabatic Greens Functions . . . . .	26
II.2.3	Nonadiabatic Greens Functions and Eigenfrequencies . . . . .	27
a)	Mode Asymmetry and Nonadiabatic Pseudo-Mode Spectra . . . . .	29
b)	Numerical Calculations . . . . .	30

c)	Calculated and Observed Spectra . . . . .	31
II.3	Fitting Medium- $l$ Spectra . . . . .	32
II.3.1	Estimators for Power and Cross Spectra . . . . .	32
II.3.2	Modelling Power and Cross Spectra . . . . .	36
II.3.3	Previous Results . . . . .	37
II.3.4	Source Depth and Noise Parameters from Power and Cross Spectra . . . . .	38
a)	Results for a Dipole Source . . . . .	39
b)	Fitting Modes with a Quadrupole Source . . . . .	43
II.4	Fitting Pseudo-Mode Spectra . . . . .	45
II.5	Fitting Low- $l$ Spectra . . . . .	48
II.6	Helioseismic Spectra Calculated by Radiative Transfer . . . . .	52
II.6.1	Radiative Transfer Calculations . . . . .	54
II.6.2	Intensity Spectra from Radiation Transfer Model . . . . .	55
II.6.3	<i>Real Intensity</i> Oscillations versus <i>MDI Intensity</i> Oscillations . . . . .	57
II.6.4	Comparison of Intensity, Velocity, and Line Depth Spectra . . . . .	57
II.7	Conclusions . . . . .	61
<b>III</b>	<b>Search for G-Modes in the Supergranular Noise</b>	<b>65</b>
III.1	Data . . . . .	66
III.2	Horizontal and Radial Components in Noise and Modes . . . . .	66
III.3	Estimation of the Noise Level . . . . .	67
III.4	Optimal Masks . . . . .	70
III.5	Masks for $l = 1$ , $l = 2$ , and $l = 3$ . . . . .	72
III.6	Detection Limits . . . . .	73
III.7	Results . . . . .	73
III.8	Discussion and Conclusions . . . . .	76
<b>A</b>	<b>Basic Equations of Nonadiabatic Oscillations</b>	<b>79</b>
<b>B</b>	<b>Filling of Attractors in the SPM Data</b>	<b>81</b>
<b>C</b>	<b>Leakage in the Pseudo-Mode Range</b>	<b>85</b>
<b>D</b>	<b>Optimal Masks</b>	<b>87</b>
<b>E</b>	<b>Normalization of Optimal Masks</b>	<b>89</b>

# Chapter I

## Introduction

*Der strahlenreichste Stern am Himmelszelt,  
Wenn er den Schnupfen kriegt, herunterfällt.  
Der beste Apfelwein schmeckt nach der Tonne,  
Und schwarze Flecken sieht man auf der Sonne.*

*Heinrich Heine: Romanzero*

Heinrich Heine backbites in his poem “Unvollkommenheit” (Imperfection) plenty of things supposed to be perfect, but indeed are not. Among them is the Sun, having “black spots”. Although this thesis has little to do with sunspots, I decided to put this stanza at the beginning of it: Helioseismic spectra are never perfect, either, but always “contaminated” by noise. This is trivially true. However, the high quality helioseismic observations from space which are available since the start of the SOHO mission in 1995 have only a small contribution from instrumental noise which could be classified as contamination. Most of the noise is of solar origin, caused by solar granulation, supergranulation, and activity noise, depending on frequency, and is therefore an essential part of the signal. “Noise in helioseismic spectra” is just a collective term for nonoscillatory signals of various processes on the Sun, which influence the spectra in the  $\mu\text{Hz}$  and the  $\text{mHz}$  region. These processes interact in a complicated way with the modes of solar oscillation. P-modes are probably excited very close to the surface, so that parts of the noise are strongly connected to the still controversial excitation process of solar p-modes. In the frequency range below  $500 \mu\text{Hz}$ , where g-modes are expected, the observed spectra are completely dominated by the solar noise, so that a precise knowledge of the spatial and temporal behavior of the noise can help in the search for the tiny signal. Information about g-mode amplitudes in turn is crucial for the discussion about excitation mechanisms for solar g-modes.

As we have seen, the term “contamination” does not adequately describe the role of the noise in helioseismic spectra, just like sunspots should not be seen as annoying imperfections, but as interesting physical phenomena. The subtle influence of solar noise on spectra will be the guideline of this thesis. Chapter I gives an introduction to the formalism of helioseismology, the observing instruments, and the various sources of noise. Chapter II discusses the influence of solar noise on p-modes and its implications on the excitation source of the modes. Chapter III presents a method to detect g-modes in the noise-dominated low-frequency spectrum, taking into account the spatial distribution of supergranulation.

## I.1 Oscillations of a Star

In a simple picture, stars are balls of gas, kept from falling apart by their own gravitational field. Modes exist as small amplitude oscillations around the hydrostatic equilibrium. For the Sun, a sharp decrease of pressure and density at the photospheric level provides reflective boundary conditions for acoustic waves, so that the modes can only exist at discrete wavelengths and frequencies. They are the eigenmodes of a gaseous sphere.

The requirements for an oscillation are initial displacement, a restoring force and an inertial force. The latter is always provided by the inertia of accelerated masses. The restoring force however depends on the type of oscillation.

Pressure (p) modes are essentially global sound waves: The restoring force is provided by the increased pressure of the denser regions. It is important that this happens in a stratified medium with radius dependent sound speed, so that the ratios of the basic frequencies and respective overtones are different from a usual acoustic resonator like an organ pipe. Scaling the eigenfrequencies of the Sun up to perceivable frequencies shows that the ratio of the keynote and its respective harmonics is substantially out of tune.

The second type of modes are internal gravity (g) modes. There, the restoring force is provided by buoyancy. Roughly speaking, g-modes exist in a subadiabatically stratified, hence nonconvective, medium. If an adiabatically displaced parcel of gas is heavier than its new surrounding, it is driven back to its equilibrium position.

The third type of stellar oscillations are surface gravity waves, the so-called f-modes. At the boundary of different fluids (like the solar surface), a displacement experiences a back driving force because of the enhanced potential energy in the gravitational field.

Without the initial displacement, the mode remains unexcited and nothing happens.

The initial displacement has to be provided by an excitation force, which will be part of the investigations of this thesis. Modes can be self excited when their damping rate is lower than the excitation rate, so that finally nonlinear effects release the energy, which can excite the modes again (Unno et al., 1989). For the Sun, excitation by other (nonoscillatory) velocity fields is predominant. In the case of p-modes, turbulent convection seems to be most important for the excitation. A lot of work has already been done for a specification of these excitation mechanisms, both numerically (Stein & Nordlund, 2001) and in data analysis (e.g., Kumar , 1994). For g-modes, the same excitation mechanism is widely assumed, but because they have not yet been detected, the situation is much more unclear (Andersen, 1996; Kumar et al., 1996).

Solar oscillations give us the chance to examine the interior of the Sun. Helioseismology can refine standard solar models which are obtained from models of stellar evolution and investigate variations of the solar structure with the activity cycle. Small scale features like sunspots can be assessed with the techniques of local helioseismology.

## I.2 Hydrodynamic Equations

In the following sections, we will present the basic formalism of stellar oscillations. Doing so, we follow basically the book of Unno et al. (1989).

The basis of hydrodynamics are the conservation laws of mass, momentum and energy. Neglecting viscosity, magnetic fields, and convective velocities is a good choice to get insight in the basic formalism of helioseismology. The convective flux is taken into account when equilibrium models are built, predominantly by using the formalism of the mixing length theory. A perturbation of the convective energy flux through oscillation however needs a time-dependent theory of convection. This is not well established (Unno et al., 1989). Therefore, the convective flux will be neglected in all calculations of this thesis. Without convective flux, the equations are given in the following form:

$$\frac{\partial \rho}{\partial t} + \nabla(\rho \mathbf{v}) = 0, \quad (\text{I.1})$$

$$\rho \left( \frac{\partial}{\partial t} + \mathbf{v} \cdot \nabla \right) \mathbf{v} = -\nabla p - \rho \nabla \Phi, \quad (\text{I.2})$$

$$\rho T \left( \frac{\partial}{\partial t} + \mathbf{v} \cdot \nabla \right) S = \rho \epsilon_N - \nabla \cdot \mathbf{F}_R, \quad (\text{I.3})$$

where  $\rho$ ,  $p$ ,  $S$ ,  $T$  are density, pressure, specific entropy, and temperature, respectively.  $\mathbf{v}$  is the velocity,  $\Phi$  is the gravitational potential,  $\epsilon_N$  is the nuclear energy generation

rate and  $\mathbf{F}_R$  is the radiative flux vector. Microphysical properties of the gas determine the two equations of state  $p(\rho, T)$  and  $S(\rho, T)$ , as well as the dependence of opacity  $\kappa$  and energy generation rate  $\epsilon_N$  on density and temperature.

The Poisson equation

$$\nabla^2 \Phi = 4\pi G \rho, \quad (\text{I.4})$$

and an equation of radiative energy transport

$$\mathbf{F}_R = -K \nabla T \quad (\text{I.5})$$

are needed to complete the description of the system. An expression for the radiative flux which is proportional to the gradient of the temperature (called “diffusion approximation”) can be derived on the assumption of local thermodynamic equilibrium.  $G$  is the gravitational constant, and  $K$  is the “radiative conductivity”, given by

$$K = \frac{4a_R c_*}{3\kappa \rho} T^3, \quad (\text{I.6})$$

where  $a_R$  is the radiation density constant, and  $c_*$  is the velocity of light.

### I.3 Equilibrium Equations

For the equilibrium state we set all velocities and time derivatives to zero. This implies a nonrotating star without convection. Due to spherical symmetry of this equilibrium state, we get

$$\frac{dp_0}{dr} = -\rho_0 g_0, \quad (\text{I.7})$$

$$\frac{dM_{r,0}}{dr} = 4\pi r^2 \rho_0, \quad (\text{I.8})$$

$$\frac{dL_{R,0}}{dr} = 4\pi r^2 \rho_0 \epsilon_{N,0}, \quad (\text{I.9})$$

$$\frac{dT_0}{dr} = -\frac{1}{K_0} \frac{L_{R,0}}{4\pi r^2}, \quad (\text{I.10})$$

where  $g$  is the gravitational acceleration and  $L_R$  is the radiative Luminosity given by  $L_R = 4\pi r^2 F_R$ .  $M_r$  is the mass within a sphere of radius  $r$ . The subscript “0” denotes the equilibrium quantities. Boundary conditions are the total luminosity and mass, and  $L_{R,0} = 0$  and  $M_{r,0} = 0$  at the center.

## I.4 Equations of Oscillation

### I.4.1 Perturbation Analysis

Oscillations arise as small perturbations from the equilibrium state. The oscillations are considered small enough for the linear approximation to be sufficient. Terms second order and higher are neglected.

In hydrodynamics, two different forms of perturbations are considered: Eulerian perturbations (indicated by a prime) denote the perturbation of a physical quantity at a fixed point in space, whereas the Lagrangian perturbations (indicated by  $\delta$ ) express the perturbation of a quantity for a given fluid element. When  $\delta\mathbf{r} = \mathbf{r} - \mathbf{r}_0$  is the displacement vector of a fluid element, the Lagrangian and the Eulerian perturbation of a quantity  $f$  are connected by

$$\delta f = f' + \delta\mathbf{r} \cdot \nabla f_0. \quad (\text{I.11})$$

Perturbation analysis is performed by superimposing small perturbations onto the equilibrium state. A physical quantity  $f$  is written either

$$f(\mathbf{r}, t) = f_0(\mathbf{r}) + f'(\mathbf{r}, t), \quad (\text{I.12})$$

or

$$f(\mathbf{r}, t) = f_0(\mathbf{r}_0) + \delta f(\mathbf{r}_0, t). \quad (\text{I.13})$$

Equations (I.1)–(I.5) can be rewritten in the perturbed variables as

$$\frac{\partial \rho'}{\partial t} + \nabla \cdot (\rho_0 \mathbf{v}) = -\nabla \cdot (\rho' \mathbf{v}), \quad (\text{I.14})$$

$$\rho_0 \frac{\partial \mathbf{v}}{\partial t} + \nabla p' + \rho_0 \nabla \Phi' + \rho' \nabla \Phi_0 = -\rho' \frac{\partial}{\partial t} \mathbf{v} - \nabla \cdot (\rho_0 \mathbf{v}' \mathbf{v}') - \rho' \nabla \Phi', \quad (\text{I.15})$$

$$\rho_0 T_0 \frac{\partial}{\partial t} (S' + \delta\mathbf{r} \cdot \nabla S_0) - (\rho \epsilon_N)' + \nabla \cdot \mathbf{F}'_R = \rho' \epsilon'_N - \rho_0 T_0 \mathbf{v} \cdot \nabla S' - \left( (\rho T)' + \rho' T' \right) \left( \frac{\partial S'}{\partial t} + \mathbf{v} \cdot \nabla S_0 + \mathbf{v} \cdot \nabla S' \right), \quad (\text{I.16})$$



$$\nabla^2 \Phi' - 4\pi G \rho' = 0, \quad (\text{I.17})$$

$$F'_R + K_0 \nabla T' + K' \nabla T_0 = -K' \nabla T'. \quad (\text{I.18})$$

In the equations denoted above, the linear terms are collected on the left hand side, while the nonlinear terms appear on the right hand side. The latter represent the source for the linear oscillations or account for the modes' damping. The first term on the right hand side of equation (I.15) is a force term (dipole source), the second term is the Reynolds stress (quadrupole source), according to Lighthill's theory of acoustic emission (for a short description, see Nigam (1999)). The third term  $\rho' \nabla \Phi'$  is usually small and can be neglected. The term on the right hand side of equation (I.15) is a mass source (monopole term). In this work, we will concentrate on the Reynolds stress source and momentum source on the right hand side of equation (I.15).

The terms on the right hand side of equations (I.16) and (I.18) are important source terms for certain types of stellar oscillations. For solar oscillation, they provide significant contribution to the damping.

## I.4.2 Separation of Radial and Horizontal Part

The equilibrium state is taken to be spherically symmetric and time independent. The left hand side of equations (I.15)–(I.18) gives a set of linear equations which contain the angular variables  $(\Theta, \Phi)$  only in the form of the horizontal Laplace operator  $\nabla_{\perp}^2$ . This allows a factorization of the perturbation in a function of radius, spherical coordinates  $(\Theta, \Phi)$ , and time, where the dependence on  $(\Theta, \Phi)$  is derived from spherical harmonic functions  $Y_l^m$  which are eigenfunctions of the horizontal Laplace operator in spherical coordinates. It follows that scalar quantities, for example a Eulerian pressure perturbation of amplitude  $\tilde{p}$  can be written as the real part of

$$p'(r, \Theta, \Phi, t) = \sqrt{4\pi} \tilde{p}'(r) Y_l^m(\Theta, \Phi) e^{i\omega t}, \quad (\text{I.19})$$

and the displacement vector is given by the real part of

$$\delta \mathbf{r} = \sqrt{4\pi} \left[ \tilde{\xi}_r(r) Y_l^m \mathbf{e}_r + \tilde{\xi}_h(r) \left( \frac{\partial Y_l^m}{\partial \Theta} \mathbf{e}_{\Theta} + \frac{1}{\sin \Theta} \frac{\partial Y_l^m}{\partial \Phi} \mathbf{e}_{\Phi} \right) \right] e^{i\omega t}, \quad (\text{I.20})$$

where  $\mathbf{e}_r$ ,  $\mathbf{e}_{\Theta}$ , and  $\mathbf{e}_{\Phi}$  are unit vectors in radial, latitudinal and longitudinal direction, respectively, and  $\tilde{\xi}_r$  and  $\tilde{\xi}_h$  are the amplitudes of radial and horizontal displacement.

The ratio of horizontal and radial wave amplitude can be derived from the outer boundary conditions. Assuming a vanishing Lagrangian pressure perturbation at the photospheric level, and applying the Cowling approximation, which neglects the distortion of the gravitational potential by the oscillations, we get

$$\frac{\tilde{\xi}_h}{\tilde{\xi}_r} = \frac{g(R)}{R\omega^2}, \quad (\text{I.21})$$

where  $R$  is the solar radius<sup>1</sup>, and  $g(R)$  is the gravitational acceleration at the Sun's surface (Christensen-Dalsgaard, 1998). It follows immediately from equation (I.21) that the visible p-modes of low and medium  $l$  (with frequencies above 1 mHz) are almost radial, whereas for the g-modes (with frequencies below 0.47 mHz), the horizontal component becomes important.

#### a) Basic Structure of the Radial Equations

After separating the radial and horizontal part, a system of linear ordinary differential equations in the radial amplitudes  $\tilde{p}'(r)$ ,  $\tilde{S}'$ ,  $\tilde{\xi}_r(r)$  etc. determines the frequencies and eigenfunctions of the Sun's oscillations. It may be noted that although the equilibrium state has been taken as spherically symmetric, the oscillations are generally not. Only in the case of  $l = 0$  the spherical harmonics are constants, and the oscillations are radial. Generally, the modes form a pattern according to spherical harmonic functions on the surface of the Sun. This fact will become very important in the investigations of Chapter III.

The equations of oscillation for a symmetric, nonmagnetic, nonrotating star without convection can be formulated as a system of six first order ordinary differential equations. Together with the boundary condition, which depend on frequency and will be discussed later on, this formalism provides a basic description of stellar oscillations, and in particular solar oscillations. If one applies the Cowling approximation, which is appropriate for high angular degree or high radial order, the dimensionality of the equations is reduced to four. If we further assume adiabaticity, which is a good approximation for low frequency oscillations we finally get second order ordinary differential equations.

The frequencies of the oscillations are eigenvalues of the two point boundary value problem. Numerical techniques such as the so-called "Shooting Method" or "Relax-

---

<sup>1</sup>The solar radius is defined as the height where the Rosseland mean optical depth, defined as  $\tau(r) = \int_r^\infty \kappa_{Ross}(r')\rho(r') dr'$  equals  $2/3$ . At this depth, the temperature is equal to the effective temperature of the Sun.

ation Method” have to be applied to calculate the eigenvalues, eigenfunctions, or response functions (Press et al., 1986).

The influence of magnetic field and (differential) rotation can be examined from that starting point with the help of perturbation analysis, depending on the respective problem. The nonadiabatic linear oscillation equations, and the formal realization of some commonly applied approximations will be denoted in Appendix A. For a nondimensional formulation of these equations, which is convenient for numerical calculations, we refer to Chapter 24 of Unno et al. (1989).

## I.5 Solar Models

So-called “standard models” of the thermodynamic quantities in the solar interior are calculated from the theory of stellar evolution under simplified assumptions concerning the physical processes during stellar evolution. An overview of these simplifications and assumptions is given in Gough (1991).

An entirely correct description of the solar interior cannot be expected from that approach. The forward problem consists of calculating eigenfrequencies for a particular solar model. The model frequencies can be compared to the observed peaks in the measured power spectra. More sophisticated models can be developed, and their frequencies can be tested for better correspondence to reality.

The adiabatic eigenvalue problem can be inverted, so that deviations of density and sound speed from a given reference model can be obtained from the observed frequencies (Kosovichev, 1999). Inversions show that the relative deviations from the standard model are within the range of a few percent. This is a confirmation of general theory of stellar evolution. Very accurate models of the solar interior, except for uncertainties of the very deep interior and a small surface layer, are among the main achievements of helioseismology.

The Sun is convectively stable from the center to about 2/3 of the solar radius. The outer 1/3 is convectively unstable. The inner part is called the *radiative interior*, because radiation is its dominant mechanism of energy transport. In the convectively unstable part, the *convection zone*, convection provides such an efficient transport of energy (and mass) that radiative energy flux becomes negligible.

The criterion for convective stability is the Ledoux condition

$$\frac{d \ln \rho_0}{d \ln p_0} > \frac{1}{\Gamma_{1,0}}. \quad (\text{I.22})$$

Here,  $\Gamma_{1,0}$  is the first adiabatic exponent. This is equivalent to the condition that the square of the Brunt-Väisälä frequency, which is defined by

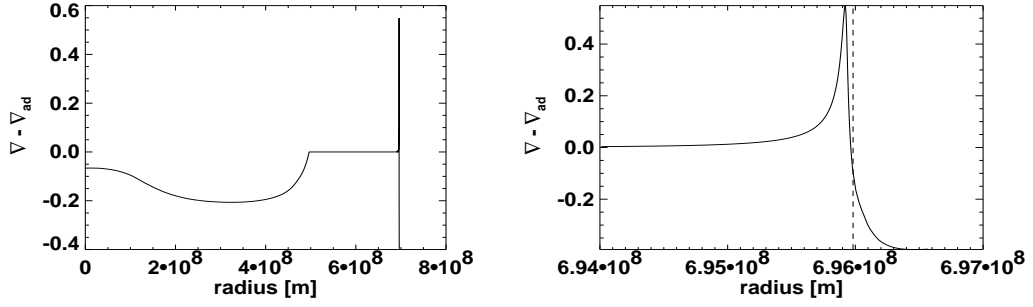


**Figure I.1:** *Left panel:* Difference between temperature gradient and adiabatic temperature gradient from the center to the photospheric level. In the convection zone, the stratification is almost adiabatic, below it is subadiabatic. *Right panel:* The surface layer is substantially superadiabatic. The vertical dashed line indicates the location of the solar radius.

$$N^2 = g_0 \left( \frac{1}{\Gamma_{1,0}} \frac{d \ln p_0}{dr} - \frac{d \ln \rho_0}{dr} \right), \quad (\text{I.23})$$

is positive (Christensen-Dalsgaard, 1998). For a homogenous chemical composition, which is realized in the convection zone, this condition is equivalent to the Schwarzschild criterion:

$$\frac{d \ln T_0}{d \ln p_0} < \left( \frac{\partial \ln T_0}{\partial \ln p_0} \right)_s. \quad (\text{I.24})$$

That means that at least a small superadiabatic temperature gradient is necessary to drive convection.

Figures I.1 and I.2 show the deviation of the solar stratification from the adiabatic stratification, and the Brunt-Väisälä frequency, respectively. The bulk of the convection zone is almost adiabatically stratified: A small superadiabatic gradient is sufficient to drive convection. Only the top of the convection zone is substantially superadiabatic. There, convective velocities are highest. In the radiative interior, the stratification is subadiabatic. The chemical inhomogeneity due to hydrogen burning in the core increases the convective stability, because lighter material (hydrogen) is placed on top of heavier material (helium).

Modes which are substantially influenced by the conditions in the radiative interior (g-modes and low-degree p-modes) are nonetheless adiabatic. When opacity is high, like in the solar interior, radiation transports energy rather slowly: The corresponding time scale is the Kelvin-Helmholz time ( $\approx 3 \times 10^7$  years, Stix (1989)). This is of course much longer than any measured helioseismic time series. Modes that are substantially influenced by the superadiabatic surface layer are distinctively nonadiabatic.

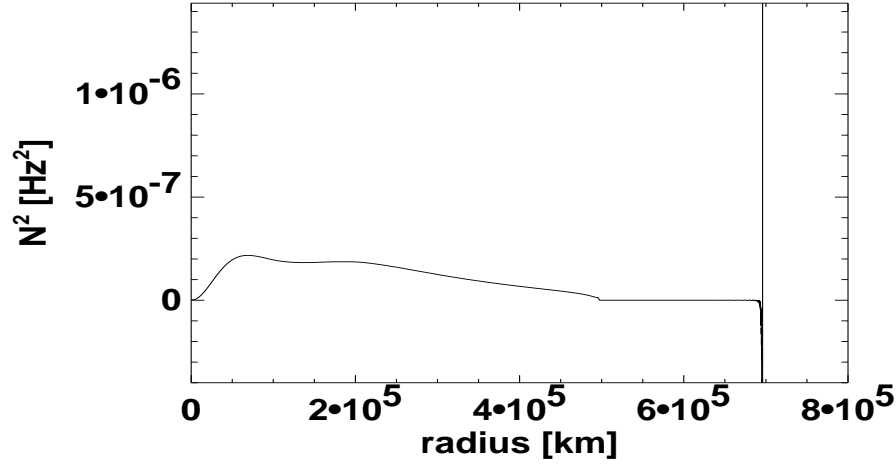


**Figure I.2:** Square of the Brunt-Väisälä frequency. Its value is positive in the radiative interior. Positive values indicate a cavity for g-modes. In the bulk of the convection zone it is close to zero and slightly negative. Close to the surface it is large and negative, exceeding the scale of the plot. In the chromosphere, it becomes positive again, indicating a second cavity for g-modes.

There, heat can be transported by convection quite efficiently during one period of oscillation.

## I.6 Adiabatic Oscillations

Basic properties of solar oscillations can be inferred from the adiabatic approximation. Further, we apply the Cowling and plane parallel approximation (see Appendix A). Solar oscillations can be interpreted as modes which are partially trapped in a cavity.

We start with equations (A.1) and (A.2) and apply the above approximations. After some manipulations, which are denoted in more detail in Christensen-Dalsgaard (1998), we get a second order differential equation in the quantity  $\chi = \rho^{-\frac{1}{2}}\delta p$ :

$$\frac{d^2\chi}{dr^2} + K(r)\chi = 0, \quad (\text{I.25})$$

where  $K(r)$  is given by:

$$K(r) = \frac{\omega^2}{c^2} \left[ 1 - \frac{\omega_{ac}^2}{\omega^2} - \frac{S_l^2}{\omega^2} \left( 1 - \frac{N^2}{\omega^2} \right) \right] \equiv \frac{\omega^2}{c^2} \left( 1 - \frac{\omega_{l,+}^2}{\omega^2} \right) \left( 1 - \frac{\omega_{l,-}^2}{\omega^2} \right), \quad (\text{I.26})$$

where  $S_l^2$  is the squared Lamb frequency  $l(l+1)c^2/r^2$ , and  $v_{ac} = \omega_{ac}/(2\pi)$ , where

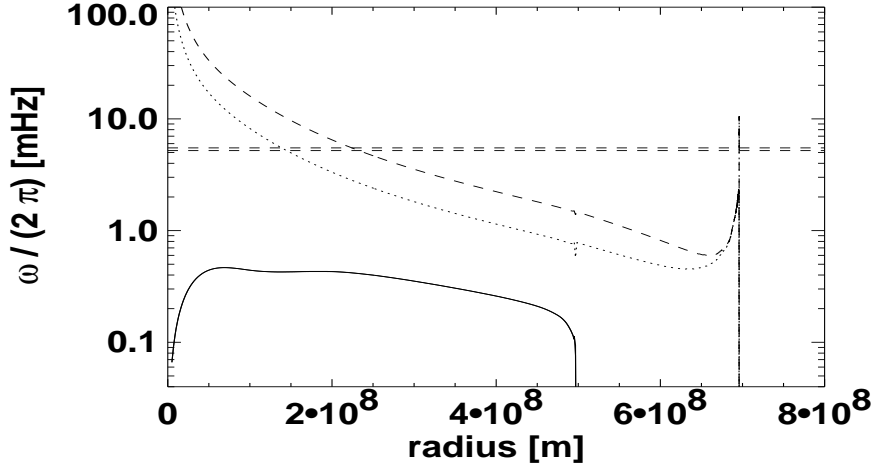


**Figure I.3:** Dotted line:  $\omega_{10,+}/(2\pi)$ ; dashed line:  $\omega_{20,+}/(2\pi)$ . Solid line:  $\omega_{10,-}/(2\pi)$ ,  $\omega_{20,-}/(2\pi)$ : This frequency has almost no  $l$  dependence, so that the two lines can not be distinguished. The horizontal dashed lines indicate the global acoustic cutoff frequency  $\nu_c$  of the Sun.

$\nu_{ac}$  is the local acoustic cutoff frequency<sup>2</sup>, defined by:

$$\nu_{ac}^2 = \frac{c^2}{16\pi^2 H_\rho^2} \left( 1 - 2 \frac{dH_\rho}{dr} \right), \quad (\text{I.27})$$

where  $H_\rho$  is the density scale height  $H_\rho^{-1} = -d \ln \rho / dr$  (Christensen-Dalsgaard, 1998).

Figure I.3 shows the two frequencies  $\omega_{l,+}/(2\pi)$  and  $\omega_{l,-}/(2\pi)$  which are defined by equation (I.26) for  $l = 20$  and  $l = 10$  based on a model of Provost, Berthomieu, & Morel (2000). The solution is locally oscillatory where  $K(r)$  is positive, that means where  $\nu < \omega_{l,-}/(2\pi)$  or  $\nu > \omega_{l,+}/(2\pi)$ . Anywhere else it is evanescent. Therefore, these two frequencies represent cavities for the modes, the lower one for the g-modes, the upper one for the p-modes. The g-mode cavity for higher  $l$  is almost entirely determined by the Brunt-Väisälä frequency (I.23). It provides a high-quality cavity for modes with a frequency below its maximum.

The p-mode cavity is dominated by the Lamb-frequency in the interior, whereas in the outer part it is dominated by the local acoustic cutoff frequency (I.27). Modes can be efficiently trapped by the outer boundary up to a frequency  $\nu_c$  slightly below the maximum of  $\nu_{ac}$ . The (global) acoustic cutoff frequency of the Sun  $\nu_c = \omega_c/(2\pi)$  is between 5.2 mHz and 5.5 mHz (Fossat et al., 1992). The frequency dependent

<sup>2</sup> $c$  is the equilibrium sound speed. In the remainder of this thesis, the subscript “0” for equilibrium quantities will be dropped, unless confusion is possible.

mode damping makes the determination of  $\nu_c$  nontrivial. Oscillations with frequencies above  $\nu_c$  are still influenced by the acoustic cavity, but they are outward propagating waves instead of trapped modes. This part of the spectrum is called the *pseudo-mode spectrum*.

Several general properties of helioseismic spectra can be obtained from the shape of the cavities:

1. G-modes exist only in the radiative zone. They are evanescent in the whole convection zone. Therefore, they have small surface amplitudes which are hard to detect.
2. There is an upper frequency limit for the existence of g-modes at about  $470 \mu\text{Hz}$ .
3. There are trapped pressure modes below  $\nu_c$ . For low frequencies, the trapping is strong, which results in low surface amplitudes and sharp peaks.
4. Modes of low angular degree  $l$  penetrate more deeply into the interior of the Sun than modes of high angular degree. Thus, low degree modes are helpful to probe the conditions in the Sun's core. The trapping at the surface is independent of  $l$ .
5. Above the acoustic cutoff frequency there are propagating waves which are only partially trapped by the acoustic cavity. This results in the so-called *pseudo-mode spectrum*.

In order to describe the p-mode spectrum, we apply the high frequency limit  $\omega \gg \omega_{l,-}$ . Then,  $K(r)$  can be approximated by

$$K(r) \approx \frac{\omega^2 - \omega_{l,+}^2}{c^2}. \quad (\text{I.28})$$

In this approximation, equation (I.25) has the form of a stationary Schrödinger equation with a radial symmetric potential. Therefore, the p-mode spectrum can be classified like atomic states with “quantum numbers”  $n$ ,  $l$ , and  $m$ . The variation of the depth of the acoustic cavity with frequency results in an approximately linear dependence of the resonance frequencies on  $n$  (Christensen-Dalsgaard, 1998).  $n$  corresponds generally to the number of radial nodes. “Quantum number” zero is assigned to the f-mode, which has no radial node. The g-modes are numbered with negative  $n$ . For the g-modes, the frequency decreases with  $|n|$ . It may be noted that there are no radial ( $l = 0$ ) g-modes, because buoyancy oscillations require horizontal density variation.

There are boundary conditions at the center and at the surface. Usually, solar models run from the center to the temperature minimum level, about 500 km above the

photospheric level. For p-modes far below the maximum of the acoustic cutoff frequency (as well as for g-modes), we may apply reflecting boundaries at the center *and* at the surface. The reflection is provided by the acoustic potential. However, for frequencies above that limit, the waves propagate further out into the upper atmosphere. This can be modelled by the boundary conditions of outgoing waves at the outer boundaries of the model. For a formal realization of this boundary condition in the adiabatic approximation, we refer to Unno et al. (1989).

## I.7 Properties of the Solar Noise

The solar velocity and intensity spectra are substantially influenced by solar noise. In helioseismology, the term “solar noise” is used for a variety of phenomena in different frequency ranges.

Granulation is the dominant source of noise in the p-mode range. Granules are convective cells with a lifetime between 5 and 8 minutes on a spatial scale of about 1 Mm. Granulation is visible in Doppler measurements as mainly vertical flow. It may be noted that Doppler measurements are usually performed in layers which are convectively stable, so that convective overshoot is observed. Simulation and observations show, that granules consist of relatively smooth and slow convective updrafts of hot gas, and fast and narrow downdrafting plumes (Title et al., 1989). As the updrafting gas is hotter than the downdrafting, granules have bright centers and dark boundaries. The fast downdrafts are probably responsible for the excitation of the p-modes (Goode et al., 1998; Rimmele et al., 1995; Stein & Nordlund, 2001). Being involved in the excitation, parts of the granular noise represent multiplicative noise, rather than additive noise.

Beside its ability to excite p-modes, granulation changes the equilibrium stratification of the solar atmosphere through the influence of turbulent pressure that adds to the gas pressure (Kosovichev, 1995). Mode cavities are enlarged through consideration of turbulent pressure, so that model frequencies in the vicinity of the acoustic cutoff frequency fit better to observations.

There is a bigger convective pattern on a scale of 30 Mm called “supergranulation” with a lifetime  $\approx 1$  day. Supergranules consist of upflowing centers and unconnected regions of downflows, where the magnetic field is concentrated. The predominant flow however is *horizontal*. There are still discussions about the origin of supergranulation. It is probably convection, driven by the recombination of ionized Helium (Stix, 1989).

Other scales of convective noise, like mesogranulation and giant cells, are widely discussed but it is not sure whether they are independent phenomena with their own



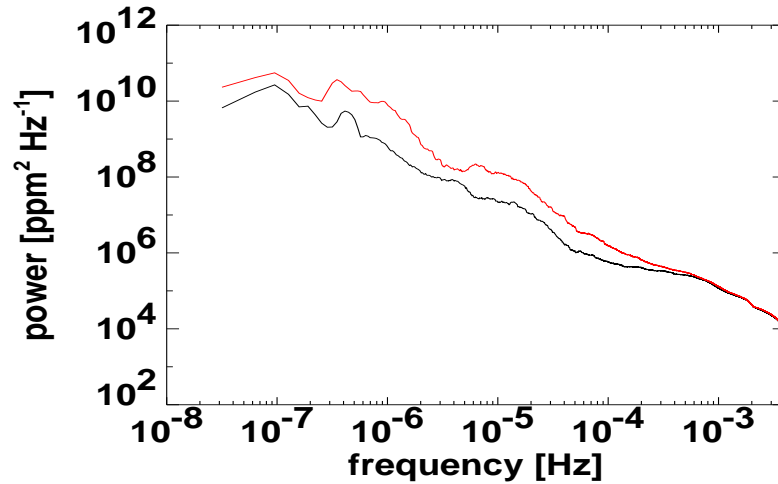


**Figure I.4:** Estimator for the noise level during solar maximum (red line) and solar minimum (black line), obtained from 1 year measurements of the SPM red channel. The prominent maximum in the black line corresponds to the solar rotation frequency of about  $0.4 \mu\text{Hz}$ . Above about  $400 \mu\text{Hz}$ , the noise levels of solar minimum and solar maximum are roughly equal.

physical driving force (Hathaway et al., 2000). Large scale flows which are time independent flow patterns on large spatial scales can interact with oscillations. Roth, Howe & Komm (2002) showed that large-scale flows of poloidal velocity fields (e.g. giant cells) with substantial amplitude would lead to distortions of the mode-multiplets. These distortions are not observed, so that an upper limit for the amplitudes of large scale flows can be set.

For frequencies below  $400 \mu\text{Hz}$ , the noise level is different at solar minimum and solar maximum (see figure I.4). The additional noise at solar maximum can be interpreted as a contribution from activity features which are rotating over the solar disk. It is mainly visible in intensity spectra. This part of the solar noise has an explicit dependence on the solar cycle. At solar minimum a prominent peak is visible at the solar rotation frequency ( $\approx 0.4 \mu\text{Hz}$ ), because only few sunspots are simultaneously visible on the solar disk. The simultaneous presence of many sunspots on the solar disk at solar maximum smears out that feature. It is remarkable that activity influences the intensity spectra at frequencies up to about  $400 \mu\text{Hz}$ , which corresponds to periods of about 40 minutes. Solar activity changes mode frequencies, as well as mode amplitudes and mode widths (Chaplin et al., 2000).

## I.8 Observational Aspects

### I.8.1 Instruments

Helioseismic oscillations are visible in the continuum intensity, the Doppler velocity (which is measured in a suitable absorption line), and the depth of this absorption line. Long time series of high quality exist only for continuum intensity and Doppler velocity.

The intensity signal is usually detected in a narrow frequency band in the continuum. Velocity measurements need more sophisticated instruments. Narrow profile filters have to be applied in the red and blue wing of a Fraunhofer line. Doppler shifts caused by velocity fluctuations lead to rising and falling intensities in the red and blue wing of the line, respectively. A calibration function describes the relationship between velocity and intensity differences in the opposing wings.

Time series can be obtained either as whole disk measurements or resolved images. SPM and GOLF are space borne instruments on SOHO, a spacecraft on a non-eclipsing orbit around the Sun-Earth Lagrange point L1 carrying many space instruments which have been measuring the Sun almost continuously since 1996. BISON and IRIS are global networks of ground based instruments for the full solar disk. MDI is a space borne instrument on SOHO with spatial resolution, while GONG and TON are global networks of spatially resolved ground based instruments. With whole disk measurements, only low  $l$  modes ( $l = 0 \dots 5$  for velocity,  $l = 0 \dots 3$  for intensity) are visible. For higher  $l$ , positive and negative contributions on the solar disk cancel each other almost completely out.

#### a) Whole Disk Measurements

The three channels of the SPM instrument are part of the VIRGO experiment (Fröhlich et al., 1995) onboard SOHO. They measure the continuum intensity in the visible part of the electromagnetic spectrum in bands of 5 nm width around 862 nm, 500 nm, and 402 nm (red, green, and blue channel). The instrument consists of wavelength filters in front of photo detectors. The resulting signal is processed in a voltage-to-frequency converter. The time series suffer from malfunction during periods which cover about 8 – 10 % of the entire measurement time. An efficient filling procedure for these periods is presented in Appendix B.

The GOLF instrument (Gabriel et al., 1995) uses the optical resonance of Na atoms in order to infer Doppler velocities from measurements of the photometric signal in the two wings of a Na D Fraunhofer line. Due to a malfunction of the instrument shortly after the beginning of the SOHO mission, the instrument's mode has been switched

to blue-wing-only measurement. Therefore, a significant contribution from intensity oscillations (about 15 % (Palle et al., 1999)) influences the signal in the p-mode range.

### b) Resolved Instruments

The MDI (Scherrer et al., 1995) instrument has five filters  $F_0$  through  $F_4$ , separated by  $75 \text{ m}\text{\AA}$  covering the width of the Ni I absorption line at  $6768 \text{ \AA}$ , which are realized by a Lyot filter and two tuneable Michelson interferometers. These filtergrams are measured continuously with a spatial resolution of  $1024 \times 1024$  pixels. The filter  $F_0$  is placed besides the line, being nearly continuum. The profiles of the five filters as a function of wavelength are displayed in figure I.5. Values for velocity, continuum intensity and line depth are obtained from the 5 filtergrams. The filtergrams are combined onboard the SOHO spacecraft to produce time series of velocity, intensity, and line depth. From the function  $\alpha$

$$\begin{aligned}\alpha_{>} &= ((F_1 - F_3) + (F_2 - F_4)) / (F_1 - F_3), \\ \alpha_{<} &= ((F_1 - F_3) + (F_2 - F_4)) / (F_4 - F_2),\end{aligned}\tag{I.29}$$

( $\alpha = \alpha_{>}$  for a positive numerator,  $\alpha = \alpha_{<}$  for a negative numerator), the velocity is obtained by a nearly linear calibration function. The MDI-velocity is calibrated to be positive for downward directed flows. Line depth is obtained by:

$$I_{ld} = \sqrt{2((F_1 - F_3)^2 + (F_2 - F_4)^2)}.\tag{I.30}$$

The continuum intensity is given by:

$$I_{cont} = 2F_0 + (F_1 + F_2 + F_3 + F_4)/4 + I_{ld}/2.\tag{I.31}$$

Examples for MDI velocity, line depth, and continuum intensity spectra are given in figures I.6 through I.8. It is important to note that  $I_{ld}$  is insensitive to Doppler velocities only in the idealized case of a perfectly symmetric absorption line and perfectly symmetric filter transfer functions. In reality, both line depth and continuum intensity are contaminated by velocity signals.

A compact and comprehensive description of how MDI works is given in Rasmussen (1999).

The LOI (Appourchaux et al., 1997) provides a low resolution solar image of continuum intensity at 500 nm with the same wavelength filter as the SPM green channel.

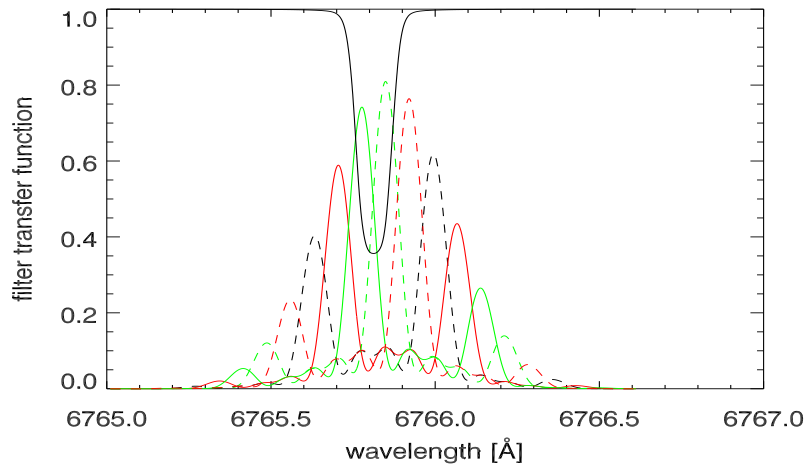


**Figure I.5:** The MDI Ni I line, normalized to the continuum level (black solid line), together with the five MDI filters as a function of wavelength. The filters are displayed with the line-styles and colors: black dashed (F0), red solid (F1), green solid (F2), green dashed (F3), and red dashed (F4).

It consists of 12 scientific and 4 guiding pixels. Modes of angular degree  $l = 0 \dots 7$  can be isolated using spherical harmonic masks. The LOI measurements can be compared to the data sets obtained from the LOI-proxy masks for the MDI which provide measurements of Doppler velocities with the same spatial resolution as the LOI.

### I.8.2 Mode Leakage

Resolved measurements provide the opportunity of additional spatial data processing. Spatial filters (“masks”) are applied to obtain time series from the images. Masks should be able to extract single modes from the spectrum. According to equations (I.19)–(I.21), the eigenfunctions of p-modes are close to spherical harmonics, with well defined modification from a limb darkening function for intensity spectra, or a projection factor for velocity spectra. Spherical harmonic functions form a complete and orthogonal system on the surface of a sphere. Hence, applying spherical harmonic masks on the visible part of the Sun provides a useful but incomplete filtering of a single mode. The filter properties of the mask function is described by the so called leakage matrix (Schou & Brown, 1994; Appourchaux, Gizon, & Rabello-Soares, 1998).

A spherical harmonic transform of the spatially resolved data set  $q$ , remapped onto the Sun’s surface, is obtained by:

$$y_l^m(t) = \int_D q(\Theta, \Phi, t) (Y_l^m(\Theta, \Phi))^* d\Omega, \quad (\text{I.32})$$

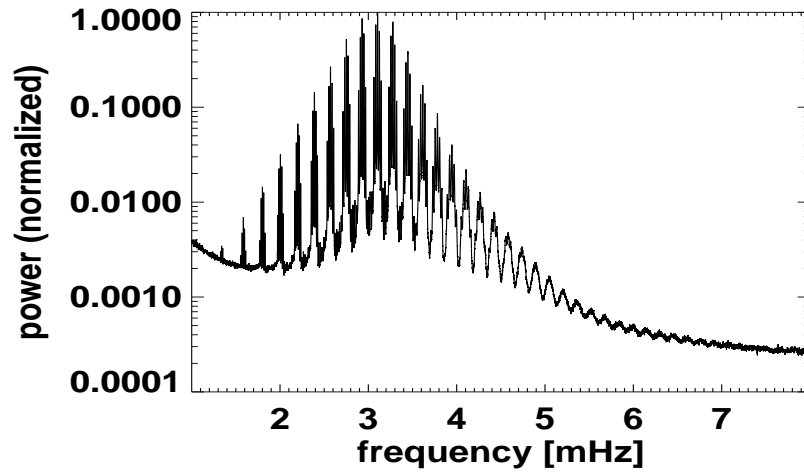


**Figure I.6:** Normalized velocity spectrum for  $l = 44$ , obtained from 59 days of full disk MDI Doppler velocity data, starting April 13, 1997.

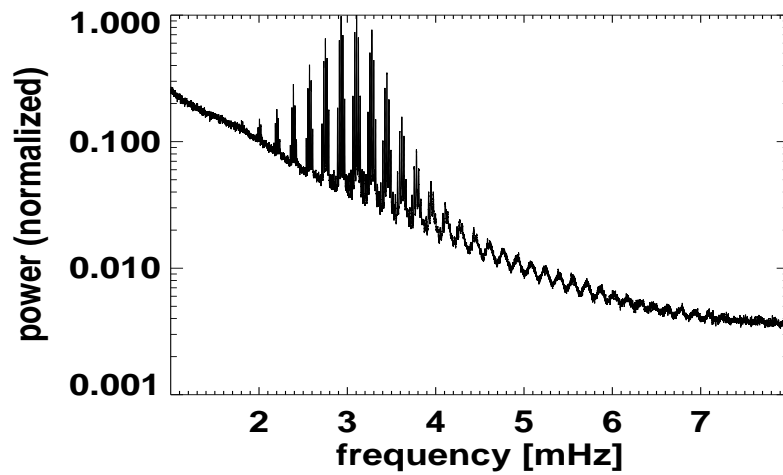


**Figure I.7:** Normalized intensity spectrum for  $l = 44$ , obtained from 59 days of full disk MDI continuum intensity data, starting April 13, 1997.

where  $D$  is the visible part of the Sun's surface. The resulting signal is linked to the Fourier spectra  $x_{l'}^{m'}$  of the modes with degree  $l'$ ,  $m'$  by

$$y_l^m(v) = \sum_{l'} \sum_{m'=-l'}^{l'} C_{l,l'}^{m,m'} x_{l'}^{m'}. \quad (\text{I.33})$$

For fixed  $l$  and  $l'$ ,  $C$  reduces to a matrix, which simplifies the notation.  $C_{l,l'}^{m,m'}$  is given by:

$$C_{l,l'}^{m,m'} = \frac{1}{n_{l,m}} \int_D \tilde{Y}_{l'}^{m'} (Y_l^m)^* A_n A_d d\Omega. \quad (\text{I.34})$$

Here  $n_{l,m}$  is a normalization factor,  $A_n$  is the natural apodization, containing e.g. a limb darkening function for the intensity data;  $A_d$  is the data apodization, which is applied e.g. for smooth transition at the solar limb.  $\tilde{Y}_l^m$  is the mode pattern on the solar surface. For velocity,  $\tilde{Y}_l^m$  is the mode's displacement eigenfunction, projected onto the line of sight. For intensity, there is no projection, but the perturbation pattern might deviate from spherical harmonics due to the influence of opacity perturbations and perturbations of the solar surface on intensity (Berthomieu & Provost, 1990).

The visible modes besides the target mode are called "leaks". They appear as non-diagonal elements of the leakage matrix. Leaks are of special importance for members of the same multiplet because the respective frequency separation is very small. Other multiplets are usually visible up to a difference in  $l$  of 6.

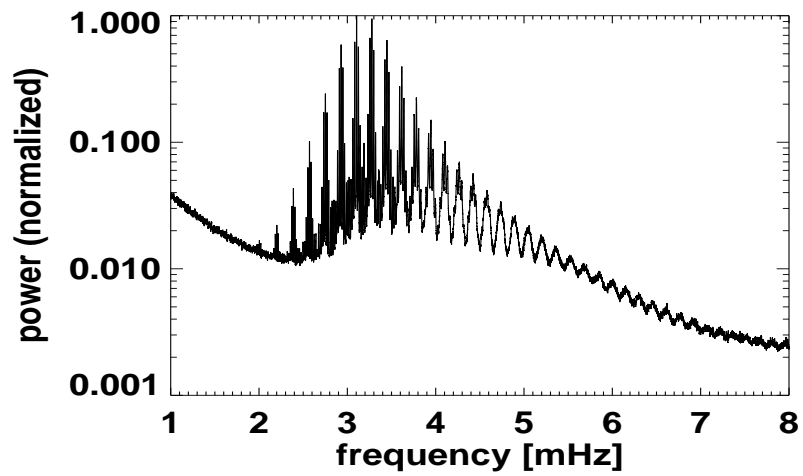


**Figure I.8:** Normalized line depth spectrum for  $l = 44$  obtained from 59 days of full disk line depth data, starting May 23, 1996.

# Chapter II

## Solar Noise and the Excitation of P-Modes

### II.1 Stochastic Excitation

#### II.1.1 Statistics of the Spectra

Solar p-modes are damped, stable oscillations, and turbulent convection associated with granulation provides a continuous stochastic excitation of the modes. A harmonic oscillator driven by a normally distributed source results in a  $\chi^2$  distribution with two degrees of freedom in the power spectrum of the linear response. Because the granular noise is also normally distributed, mode and granulation signals obey the same statistics. The normal distribution is a consequence of the fact, that the mode source is a sum of many independent sources. Mode parameters like amplitude and width are estimated with maximum likelihood estimators (MLE) (Anderson, Duvall, & Jefferies, 1990).

For spatially resolved data, the rotationally split members of a multiplet can be regarded as different realizations of a stochastic process. Therefore, in order to get a spectral estimator, the spherical harmonic transform power spectra are shifted in frequency to compensate the splitting. After that, the shifted spectra are averaged. In the simplest approach, the spectra are regarded as independent, and the averaged spectrum has a  $\chi^2$  distribution with  $2(2l + 1)$  degrees of freedom for each frequency bin, which approaches a normal distribution for high  $l$ . However, the averaged spectra are not completely independent (due to offdiagonal elements in the leakage matrix), and the MLE fit has to be performed for a set of multi-normally distributed Fourier spectra, where the distribution is described by the mode leakage matrix and the noise covariance matrix (Schou, 1992).



### II.1.2 Turbulent Convection

Eddies close to the upper convection zone have correlation times that are comparable to the mode periods, and therefore they are able to transfer energy to the modes. Goldreich, Murray, & Kumar (1994) suggest that only below the observed maximal oscillation power at about 3 mHz, energy-bearing eddies exist with the appropriate correlation time to excite the modes. Together with the frequency dependence of mode reflection at the solar photosphere, the observed dependence of the excitation rate on frequency can be explained.

Generally, convective upflows in granules are slow and laminar, while convective downflows in intergranular lanes are fast and turbulent. Simulations of convection of Stein & Nordlund (2001) suggest that turbulent pressure fluctuations (Reynolds stress source) are coherent structures in depth and time. They are isolated and concentrated in intergranular lanes, and provide the most essential energy supply for the p-modes through stochastic excitation. Fluctuations of the gas pressure due to radiative cooling of upflowing gas are concentrated near the surface. They represent a entropy (monopole) source. They are less effective in exciting oscillatory modes (Stein & Nordlund, 2001).

### II.1.3 Seismic Events

So-called “Seismic Events” have been observed by Goode et al. (1998) and Rimmele et al. (1995). There are dark lanes between granules, where high vertical velocities and an enhanced phase difference with altitude have been observed. Acoustic power from the f-mode ridge can be observed in the immediate neighborhood of these events. The power of the acoustic events would be sufficient to drive the entire p-mode spectrum. In analogy to terrestrial seismology, these events can be called “sunquakes”, being surface events giving rise to global oscillations. Stein & Nordlund (2001) suggest, that these events represent the upper tail in the strength distribution of the stochastic excitation process which is concentrated in the intergranular lanes.

Numerical investigations (Rast, 1999) suggest, that these events are comprised of three successive stages: radiative cooling at the surface, buoyant downward acceleration and horizontal inflow in the evacuated volume. The three stages can result in monopolar, dipolar, and quadrupolar acoustic emissions, where monopolar emissions result from volumetric changes, dipolar emissions result from momentum input, and quadrupolar emissions result from internal stresses, which are associated with Reynolds stresses in the Sun (Goldreich & Kumar, 1990).

## II.2 Theoretical Oscillation Spectra

Originally, the acoustic resonances of the Sun have been described by a damped harmonic oscillator, which results in a symmetric Lorentzian peak shapes. However, asymmetry is observed for the peaks (Duvall et al. , 1993).

For a linear system, the response power spectrum  $P$  for an arbitrary source  $S$  can be calculated by:

$$P(\omega, r_{obs}) = \left| \int dr_s S(r_s, \omega) G(r_{obs}, r_s, \omega) \right|^2, \quad (\text{II.1})$$

where  $G(r_{obs}, r_s, \omega)$  is the Green's function depending on observation height  $r_{obs}$ , source depth  $r_s$ , and frequency  $\omega$ . The excitation is likely to occur in the shallow, strongly superadiabatic layer close to the photospheric level where convective velocities are highest (see figure I.1). The source consists of mass terms, force terms, and Reynolds stress terms, and it is not clear, which one is dominant. The frequency and radius dependence of these terms can not be easily specified. However, for a single mode a frequency independent source which is well localized in the superadiabatic layer close to the surface is a reasonable assumption. The relevant scale for the radial extension of the source is the local pressure scale height close to the surface. If the radial mode wavelengths are much higher, the spatial distribution of the source can be described by a delta function. Removing derivatives (see equations (I.14), (I.15)) in the source terms through integration by parts, it is straightforward to show, that the response to a delta function excitation is given by:

$$P(\omega, r_{obs}) \propto \left| \sum_{n=0}^2 a_n \frac{d^n G(r_{obs}, r_s, \omega)}{dr_s^n} \right|^2, \quad (\text{II.2})$$

(Kumar & Basu, 1999b; Kumar , 1994). Note that the derivative has to be taken with respect to the source location. In a stratified medium, the order of the derivative  $n$  can not unambiguously be assigned to a particular multipole moment. But as pointed out by Kumar (1994), a quadrupole source is predominantly described by a term with  $n = 1$ , whereas a dipole source is represented by  $n = 0$ . Both cases will be examined.

For consistency with other authors, the value of the radial oscillation function at a uniform observation height 300 km above the solar radius has been taken to calculate the theoretical spectra. As examined in detail by Rasmussen (1999), the effective observation height at a particular wavelength (i.e.  $\tau = 1$ ) depends on the position on the solar disk. Furthermore, the core of the line is formed higher up in the atmosphere

than its wings. For the MDI absorption line, Rasmussen (1999) gives a formation height between from 100 km (wings) and 360 km (core) above the solar radius. The particular profiles of the MDI filters causes the signal to experience more influence from the center of the line than from the wings. When theoretical spectra are fitted to observed power spectra later in this thesis, varying the observation height between 180 km and 400 km above the solar radius leads to no significant difference in the fitted parameters.

A localized source introduces intrinsic asymmetry in the mode peaks. Asymmetry of the resonance peaks is a general property of acoustic cavities excited by a localized source. Sign and value of the asymmetry depend on the exact location of the source with respect to the radial nodes of the mode under regard.

A lot of different approaches to calculate artificial spectra, both analytical and numerical, have been developed to model the observed helioseismic spectra. Some of them will be presented in the next subsections. We will start with the analytically resolvable potential well model, then we will present the numerical solution of the adiabatic approximation, and finally we will present the solution of the full set of linear equations given in Appendix A (nonadiabatic solution). All these models are described in literature (e.g., Unno et al., 1989; Christensen-Dalsgaard, 1998). We will use the most detailed (nonadiabatic) description of solar oscillations modes to fit power and cross spectra of intensity and velocity to infer properties of the mode excitation process.

### II.2.1 Potential Well Model

Abrams & Kumar (1996) used a analytical approach to examine the shape of adiabatic p-modes. The acoustic potential  $\omega_{l,+}^2$  for the equation (see equations (I.25) and (I.28), and figure I.3):

$$\frac{d^2\chi}{dr^2} + \frac{\omega_1^2 - \omega_{l,+}^2}{c^2}\chi = S(\omega)\delta(r - r_s) \quad (\text{II.3})$$

is approximated by a square well potential with:

$$\omega_{l,+}^2 = \begin{cases} 0 & \text{for } r < a_l \\ \omega_c^2 & \text{for } r \geq a_l. \end{cases} \quad (\text{II.4})$$

Here,  $a_l$  is the angular degree dependent depth of the cavity,  $\omega_c$  is the acoustic cutoff frequency, and  $\omega_1^2 = \omega^2 + i\Gamma\omega$ .  $\Gamma$  is the damping coefficient. This acoustic potential is regarded as approximation for the potential shown in figure I.3.

Together with the boundary condition of outgoing waves for  $\omega > \omega_c$ , and outward exponential decay for  $\omega < \omega_c$ , the solution of the differential equation (II.3) is given by:

$$\chi^{in}(\omega) = -S(\omega) \frac{c \sin(\omega_1 r_s / c)}{\omega_1 \cos(\omega_1 a_l / c) + \omega_2 \sin(\omega_1 a_l / c)} e^{-\omega_1 (r - a_l) / c} \quad (\text{II.5})$$

for  $r_s < a_l$ , and

$$\chi^{out}(\omega) = S(\omega) \frac{c \omega_1 \cos \frac{\omega_1 a_l}{c} \sinh \frac{\omega_2 (r_s - a_l)}{c} + \omega_2 \sin \frac{\omega_1 a_l}{c} \cosh \frac{\omega_2 (r_s - a_l)}{c}}{\omega_1 \cos \frac{\omega_1 a_l}{c} + \omega_2 \sin \frac{\omega_1 a_l}{c}} e^{-\frac{\omega_1 (r - a_l)}{c}} \quad (\text{II.6})$$

for  $r_s \geq a_l$ .  $\omega_2^2$  is given by  $\omega_c^2 - \omega_1^2$ .  $c$  is the uniform sound speed. Note that  $\chi^{in} = \chi^{out}$  for  $r_s = a_l$ , so that it is possible to define a continuous function  $\chi = \chi^{in}$  for  $r_s < a_l$ , and  $\chi = \chi^{out}$  for  $r_s \geq a_l$ .

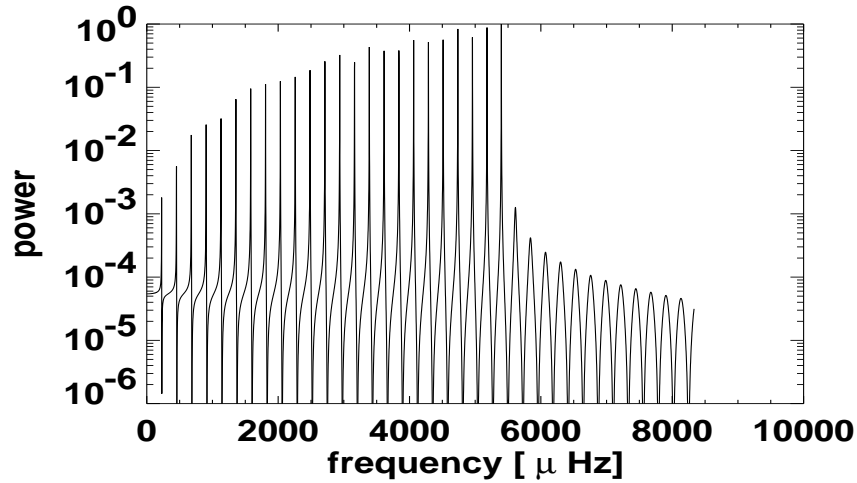


**Figure II.1:** The solution for the potential well model for  $r_s = a_l$ , and  $r_s/c = 2182s$ . The peaks are strictly equidistant. Above the acoustic cutoff frequency, propagating waves produce the pseudo-mode spectrum.  $\nu_c$  has been set to 5.5 mHz. The power is normalized to the maximum.

Figure II.1 shows an example for  $|\chi|^2$ . Qualitatively, the properties of a p-mode spectrum of a single angular degree  $l$  are reproduced. The asymmetry is negative for an excitation close to the surface, which means that more power is in the low frequency wing than in the high frequency wing. Asymmetry is most distinctive for the lowest frequencies. The degree of asymmetry depends on the source depth and changes its sign, when the source location crosses the node of the eigenfunction.

Close to the resonance, an asymptotic expression can be derived from equation (II.5). By adding a correlated<sup>1</sup> and an uncorrelated background and expanding the expression given by equation (II.5) in the neighborhood of a resonance, Nigam & Kosovichev (1998) derived a modified Lorentzian profile given by:

$$P(x) = A \frac{(1 + \beta x)^2 + \beta^2}{1 + x^2} + B, \quad (\text{II.7})$$

where  $x = 2(\nu - \nu_0)/\Gamma$ ,  $B$  is the additive background parameter, and  $A$  is the amplitude parameter. The asymmetry parameter  $\beta$  depends in a complicated way on the source depth and correlated background, and can be assumed to be a (frequency independent) complex number for each mode multiplet. Because phase and amplitude of this parameter are difficult to fit simultaneously, it is usually fitted as a real number. A real parameter  $\beta$  is able to sufficiently describe the observed skew symmetric profiles of the peaks, but does not give direct information about the source depth and strength of the correlated noise.

## II.2.2 Adiabatic Greens Functions

Solving equation (II.3) by using an acoustic potential calculated from a solar model with the help of equation (I.26) in the high frequency approximation (see equation (I.28)), results in spectra which are, compared to the simple potential well model, closer to reality. In particular, low frequency peaks hit the observed mode frequencies within a few  $\mu\text{Hz}$ . Figure II.2 shows a power spectrum for the solar model of Provost, Berthomieu, & Morel (2000).

Temperature oscillations are usually used as a proxy for intensity oscillations, which can be obtained from the Green's function  $\chi(\omega)$  by:

$$\frac{\delta T}{T} = -\nabla_{ad} \frac{\Gamma_1 \chi}{p}. \quad (\text{II.8})$$

The velocity perturbation can be obtained directly from:

$$v = i\omega \frac{\Gamma_1 \left( p\chi + \omega^2 c^2 / g / S_l^2 \left( p \frac{d\chi}{dr} - g\rho\chi + p \frac{d \ln \Gamma_1}{dr} \chi \right) \right)}{\rho(g - \omega^4 c^2 / g / S_l^2)} \quad (\text{II.9})$$

(see Christensen-Dalsgaard (1998)).

<sup>1</sup>The concept of correlated noise will be explained in Section II.3.

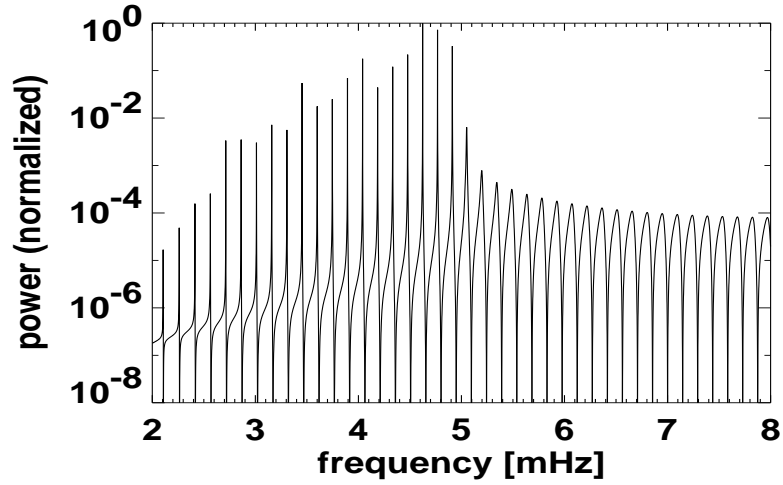


**Figure II.2:** Adiabatic Green's function for the Lagrangian pressure perturbation of angular degree  $l = 22$ , an imaginary part of the frequency of  $1 \mu\text{Hz}$ , and a source at the solar radius. The solar model is described in Provost, Berthomieu, & Morel (2000).

For higher frequencies, the difference between the adiabatic model frequencies and the observed frequencies is substantial. This is because high frequency modes have upper turning points in the superadiabatic surface layers, where the oscillations are poorly described by the adiabatic equations, and where the equilibrium model is most inaccurate.

### II.2.3 Nonadiabatic Greens Functions and Eigenfrequencies

Solving the equations (A.1)–(A.5) with an appropriate source gives the best estimate of the spectrum. As in Kumar (1994), the force term  $\rho' \frac{\partial}{\partial t} \mathbf{v}$  or the Reynolds stress term  $\nabla \cdot (\rho_0 \mathbf{v}\mathbf{v})$  are considered to be the source, respectively. For angular degrees lower than 400, close to the surface, the modes are essentially radial, so that only the radial component of the Reynolds stress provides a significant contribution to the excitation. In this case it can be shown that a perfectly localized source results in a delta-function term on the right hand side of equation (A.1). The inner boundary conditions are governed by regularity at the center, whereas the outer boundary conditions are derived assuming quasi-isothermal conditions at the surface, i.e., the equations are solved with constant coefficients, and the solutions are selected to provide outward going waves for frequencies above  $\omega_c$ , regularity of the kinetic energy of p-modes, and prohibit inward directed radiative flux (Unno et al., 1989). From these equations, we get a spectrum for the radial velocity oscillations  $v = i\omega\tilde{\xi}_r$  and luminosity oscillations  $\delta L/L$ . Oscillations in other thermodynamic variables like pressure or temperature can be derived if

needed. The luminosity oscillations are assumed to be proportional to the observable intensity oscillations. However, as pointed out by Unno et al. (1989), oscillations perturb the limb darkening function, and geometrical effects from the perturbation of the surface (Berthomieu & Provost, 1990) influence the continuum intensity. This leads to a perturbation of the Eddington factor, which is neglected in our calculations. However, luminosity is a better proxy for intensity than temperature, because additional effects from perturbations of the mean opacity and of the temperature stratification are taken into account.

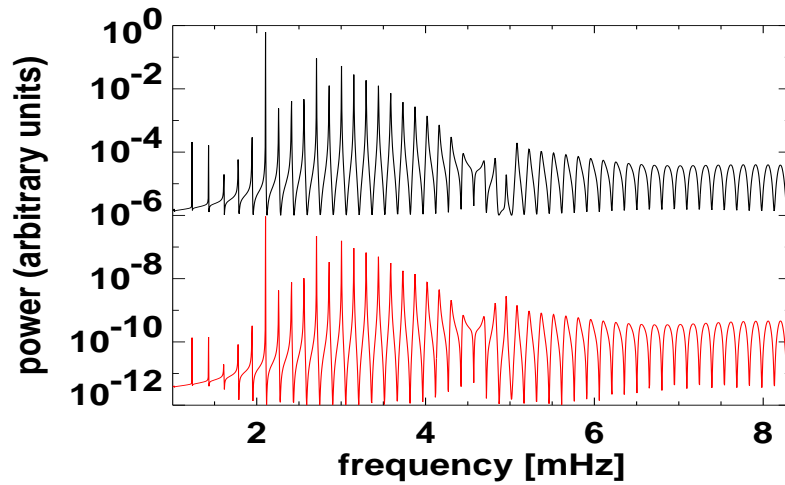


**Figure II.3:** Intensity spectra (black line) and velocity spectra (red line) form a nonadiabatic Green's function with a source depth of +100 km, and an imaginary part of the frequency of 1  $\mu\text{Hz}$ . Note, that the displayed peak-height at low frequencies is heavily influenced by the finite frequency resolution. The absolute value of the vertical scale is arbitrary.

Figure II.3 shows the nonadiabatic power spectra for velocity and intensity for a source depth of +100 km. The nonadiabatic power spectrum reproduces, unlike the adiabatic spectrum, a decline in its peak height above 3 mHz due to reduced atmospheric reflection (Goldreich, Murray, & Kumar, 1994). Even so, the observed frequency dependence of the amplitudes can not be reproduced with a frequency independent source strength. It is further important to note that the observed mode width is largely underestimated because a variety of damping effects have been neglected in the formulation of equations (A.1)–(A.5).

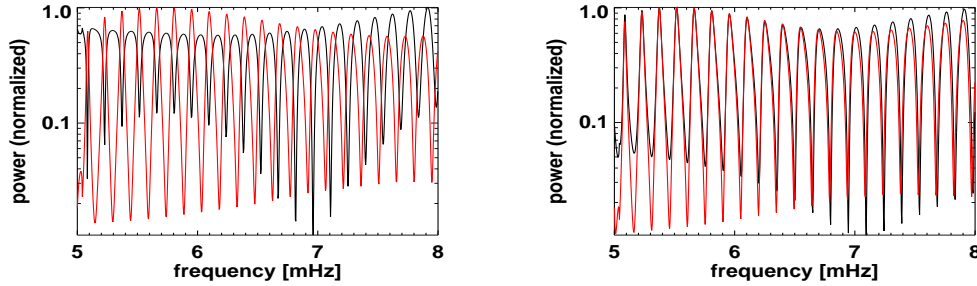


**Figure II.4:** Pseudo-mode spectrum of intensity (black line) and velocity (red line) from a Green's function for a source depth of 0 km (left panel), and a source depth of +40 km (right panel).

### a) Mode Asymmetry and Nonadiabatic Pseudo-Mode Spectra

Of particular interest is the fact that for sources shallower than +60 km<sup>2</sup>, the pseudo-mode peaks do not necessarily occur at the same frequencies in velocity and intensity (see figure II.4). This contradicts the conclusion of Rast & Bogdan (1998) that velocity and intensity spectra share the same intrinsic shape of the spectra, in particular the same line profile and the same spectral locations of the pseudo-mode peaks. This is not the case if the source is placed sufficiently close to the surface (not deeper than +60 km). The differing results can be explained simply by the fact, that Rast & Bogdan (1998) used a simplified model with an isothermal layer on top of a polytropic layer, and that instead of luminosity, temperature is taken as a proxy for the intensity spectra. Figure II.5 shows that pseudo-mode peaks in observed spectra are indeed mutually shifted in velocity and intensity. Using the same profiles for the velocity and the intensity oscillations is therefore not necessarily correct. However, in Section II.4 it will be shown that in the pseudo-mode frequency range neither velocity nor intensity spectra are reproduced accurately enough by the nonadiabatic Green's functions to model the observed spectra.

The situation is similar concerning the asymmetry of p-modes. The line asymmetry of the pure oscillation power spectra can not be of opposite sign for intensity and velocity spectra, but they are of different extent if the source is not too deep (above +100 km) in the convection zone (see figure II.6). For deeper sources, the profiles are almost identical.

---

<sup>2</sup>+60 km: In the remainder of this thesis, positive values will correspond to sources *below* the solar radius, whereas negative values correspond to levels *above* the solar radius.



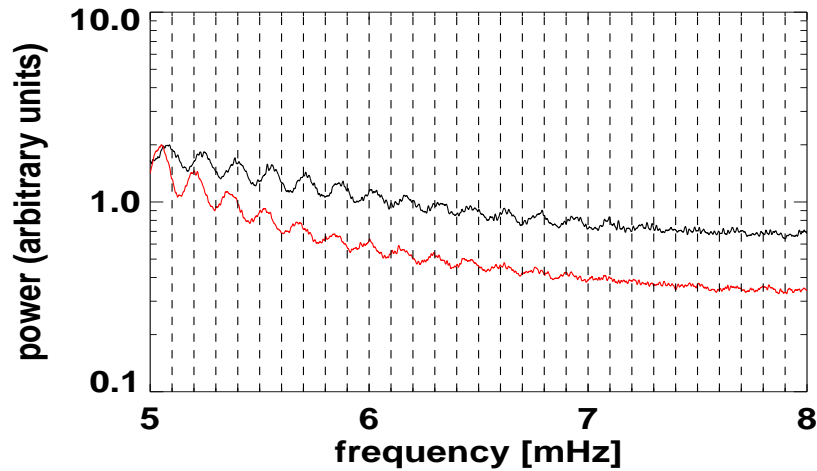


**Figure II.5:** Pseudo mode power spectrum of intensity (black line) and velocity (red line) of angular degree  $l = 44$ . The dashed vertical lines help to see how the peaks of both spectra line up.

## b) Numerical Calculations

Evaluating the eigenfrequencies of a solar model is a nonlinear two boundary eigenvalue problem in the perturbed variables *and* the corresponding eigenfrequency. It can be solved using relaxation techniques described in Press et al. (1986), to simultaneously evaluate eigenfrequencies and eigenfunctions. The nonadiabatic eigenfrequencies are intrinsically complex. The imaginary part has a magnitude comparable to the real part only at frequencies close to the acoustic cutoff frequency.

The response function to a source can be calculated by integrating the product of source function and Green's function over radius (see equation (II.1)). The pressure scale height at the surface (rising from 140 km to 250 km in the range of 0 km to +200 km) is much smaller than the radial mode-wavelength. Therefore, it is reasonable to consider a pure point source for all calculations. Then, the response function is directly given by the Green's function. Other than the calculation of eigenfrequencies and eigenfunctions, the determination of the Green's function is a linear problem, because there the frequency is a parameter, rather than a variable. Whereas eigenfunctions exist only for discrete frequencies, the Green's function can be calculated for all frequencies. The inhomogeneous equation for the Green's function can also be conveniently solved using relaxation techniques, but thanks to linearity, neither a trial solution nor iterations are necessary. Shooting methods (Press et al., 1986) turn out to be numerically unstable for that particular problem.

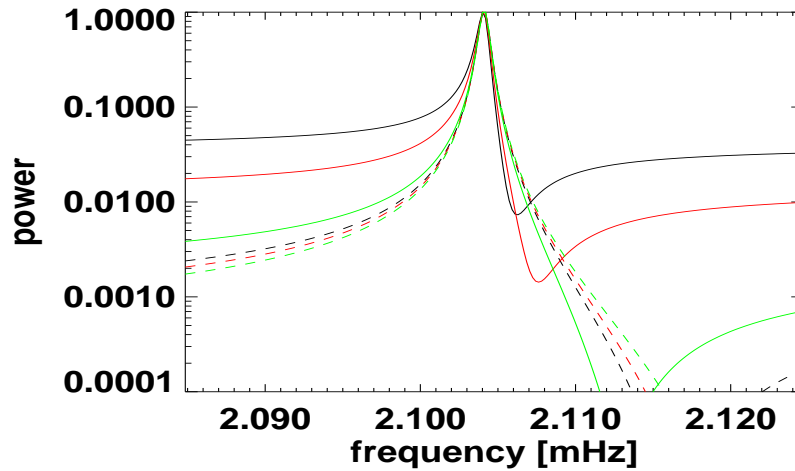


**Figure II.6:** Different shapes of velocity and luminosity peaks for source depths of 0 km (black lines), +40 km (red lines), and +80 km (green lines) for the  $l = 22$ ,  $n = 8$  mode: luminosity peaks correspond to the solid lines, velocity peaks correspond to the dashed lines. All peaks are normalized to their maxima.

### c) Calculated and Observed Spectra

For low frequencies, the peaks of the response function are very close to the eigenfrequencies. For frequencies in the neighborhood of the acoustic cutoff frequency, this is no longer true. In particular, the maxima in the pseudo-mode range do not correspond to calculated eigenfrequencies, because pseudo-modes are propagating waves instead of eigenmodes.

Neglecting the perturbation of the convective energy flux, as we did for the nonadiabatic calculations, introduces serious errors for all modes that have a substantial travel time through the convection zone, i.e. all p-modes and f-modes. The simplification is driven by the desire to avoid complexity, and is not always a good approximation (Unno et al., 1989). However, mode frequencies, which have an upper turning point below the strongly superadiabatic layer, i.e. modes below about 2.5 mHz, are reproduced reasonably well by adiabatic and nonadiabatic calculations, as shown in figure II.7. We will see later, that mutual phases of velocity and intensity in this frequency range are nevertheless different. They are substantially better reproduced by nonadiabatic calculations which include radiative transfer.

Figure II.8 compares nonadiabatic and adiabatic eigenfunctions. The adiabatic luminosity perturbation is represented by the respective temperature perturbation. The plots show that adiabatic and nonadiabatic velocity eigenfunctions are almost identical, except for a small deviation in the photosphere. The nonadiabatic luminosity eigenfunction and the adiabatic temperature eigenfunction are substantially different,

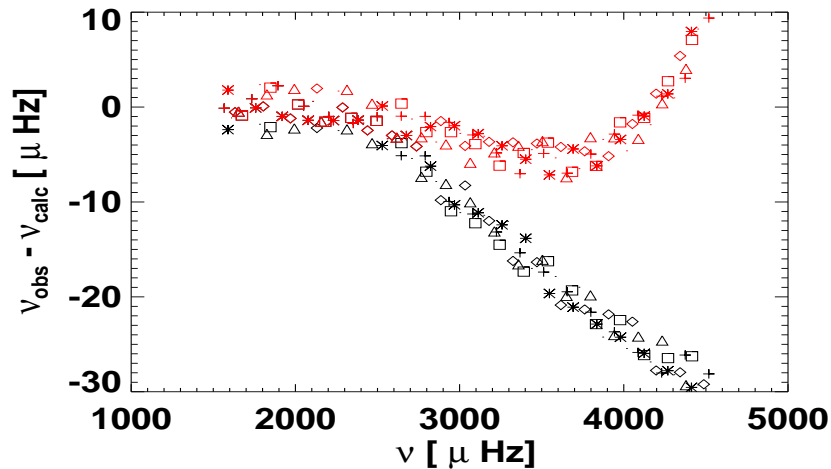


**Figure II.7:** Deviation of the observed mode frequencies from adiabatic (black labels) and non-adiabatic (red labels) model frequencies for angular degrees  $l=20 - 25$  and radial order  $n = 5 - 24$  (displayed as: cross (20), star (21), point (22), diamond (23), triangle (24), square (25)).

which is particularly pronounced in the strongly superadiabatic upper convection zone. The deviation of the luminosity eigenfunction illustrates that, although mode profiles are almost identical for adiabatic and nonadiabatic power calculations (see figure II.9), the eigenfunctions and, as we will see below, the mutual phases might deviate substantially.

The influence of convective flux on the mutual phases in the superadiabatic layer remains an open issue. However, compared to simplified models such as the potential well model, the model of two wave interference (Duvall et al. , 1993), or the adiabatic approximation, we can expect to see an improvement towards much more accurate spectra, and to make the estimates of spectral parameters more reliable. When we adjust the parameters of the model to fit the observed spectra, the parameters depend heavily on the respective model for the pure oscillator, so that this model has to be as accurate as possible in order to get physically meaningful values for noise parameters and source depth.

## II.3 Fitting Medium- $l$ Spectra

### II.3.1 Estimators for Power and Cross Spectra

The expectation values for the spectra of spherical harmonic transforms of Doppler velocity and continuum intensity are expected to depend on angular degree  $l$ , but not on tesseral order  $m$ . If  $v_l^m(\nu)$  and  $i_l^m(\nu)$  are the Fourier transforms of the spherical

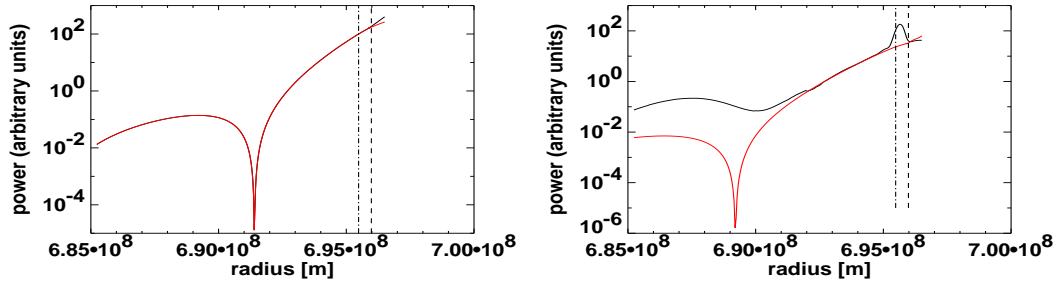


**Figure II.8:** Green's functions for  $l = 22$ , close to the calculated resonance frequency at 2.1042 mHz, as a function of radius. The source depth is +500 km. The Green's functions should be a very good approximation to the respective eigenfunctions of the  $l = 22$ ,  $n = 8$  mode. *Left panel:* Nonadiabatic velocity eigenfunction (black line), and adiabatic velocity eigenfunction (red line). *Right panel:* Nonadiabatic luminosity eigenfunction (black line), and adiabatic temperature eigenfunction (red line). The dashed line indicates the solar radius. The dashed-dotted line indicates the source location.

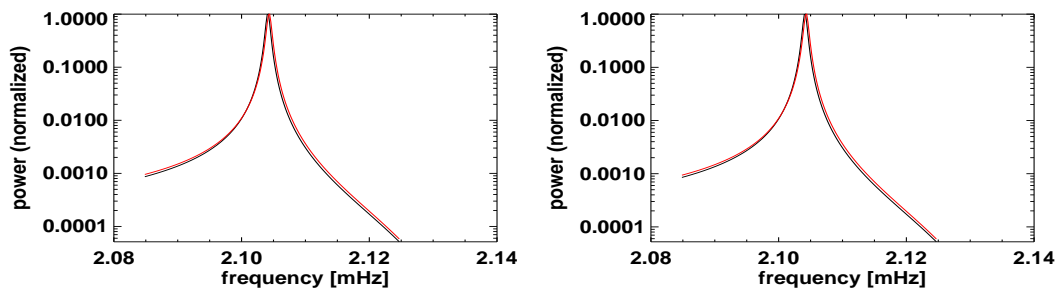


**Figure II.9:**  $l = 22$ ,  $n = 8$  mode for a source depth of +500 km. *Left panel:* Power peak of the nonadiabatic velocity Green's function (black line), and the adiabatic velocity Green's function (red line). *Right panel:* Power peak of the nonadiabatic luminosity Green's function (black line), and the adiabatic temperature Green's function (red line).

harmonic transforms of the velocity and intensity time series, respectively, then the power spectra  $P_I^l$  and  $P_V^l$ , the mutual phase  $\Phi^l$ , and the mutual coherence  $\rho^l(\nu)$  are defined as:

$$P_I^l = E|i_l^m(\nu)|^2, \quad (\text{II.10})$$

$$P_V^l = E|v_l^m(\nu)|^2, \quad (\text{II.11})$$

$$\Phi^l = \arg E[i_l^m(\nu)(v_l^m(\nu))^*], \quad (\text{II.12})$$

$$\rho^l(\nu) = \frac{E[i_l^m(\nu)(v_l^m(\nu))^*]}{\sqrt{P_I^l(\nu)P_V^l(\nu)}}. \quad (\text{II.13})$$

$E$  denotes the expectation value. An estimator of the power and cross spectra can be obtained by shifting and averaging the spherical harmonic transform spectra according to the frequency splitting:

$$\hat{P}_I^l = \sum_{m=-l}^l |i_l^m(\nu + \Delta\nu_m)|^2, \quad (\text{II.14})$$

$$\hat{P}_V^l = \sum_{m=-l}^l |v_l^m(\nu + \Delta\nu_m)|^2, \quad (\text{II.15})$$

$$\hat{\Phi}^l = \arg \sum_{m=-l}^l i_l^m(\nu + \Delta\nu_m)(v_l^m(\nu + \Delta\nu_m))^*, \quad (\text{II.16})$$

$$\hat{\rho}^l = \frac{|\sum_{m=-l}^l i_l^m(\nu + \Delta\nu_m)(v_l^m(\nu + \Delta\nu_m))^*|}{\sqrt{\hat{P}_I^l \hat{P}_V^l}}. \quad (\text{II.17})$$

We used spherical harmonic transforms of full-disk MDI data of Doppler velocity and continuum intensity, starting April 13, 1997. The data cover 61 days and are almost continuous. Long term trends in the data were removed by subtracting a running mean over 90 minutes. This is an efficient high pass filter, making the time series stationary, and leaving the spectra unchanged in the frequency range of our interest. To obtain the splitting  $\Delta\nu_m$ , the frequencies of the target modes of all single  $m$  spectra are estimated with the maximum likelihood technique. The obtained dependence of frequency on

$m$  is projected onto Legendre polynomials in  $m/l$ . Keeping only the first five coefficients  $c_1 \dots c_5$  provides a smooth and sufficiently accurate estimate of the splitting. Hence,  $\Delta\nu_m$  is given by:

$$\Delta\nu_m = l \sum_{i=1}^5 c_i P_i(m/l), \quad (\text{II.18})$$

where  $P_i$  is the Legendre Polynome of order  $i$ .

Mode multiplets in a frequency range of  $1900 \mu\text{Hz}$  to  $2500 \mu\text{Hz}$ , and with  $l \approx 15$  to  $l \approx 25$  are well separated in frequency from neighboring  $(n, l)$  multiplets, have sufficient signal-to-noise ratio, and the number of multiplet members is big enough to give satisfactory spectral estimates by averaging over  $m$ .

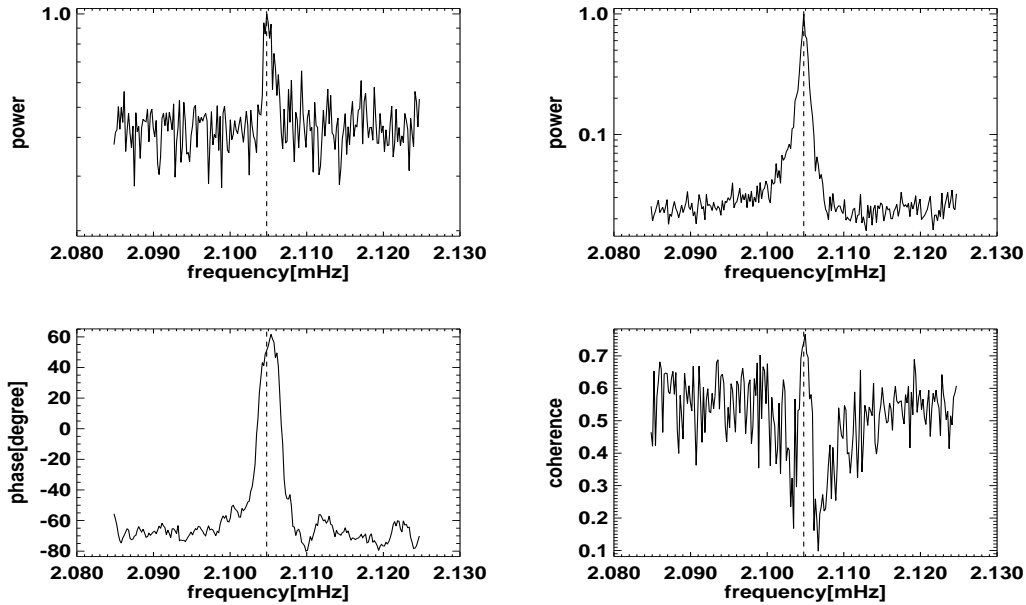


**Figure II.10:** Power and cross spectra of intensity (upper left), velocity (upper right), phase (lower left), and coherence (lower right) for the  $l = 22, n = 8$  mode. The power spectra are normalized to their maxima. The resonance frequency is indicated by the vertical dashed line.

Figure II.10 shows the intensity and velocity power spectrum, and the mutual phase and coherence of the  $l = 22, n = 8$  mode at  $2.1048 \text{ mHz}$ . The peaks of the velocity and intensity power show marked asymmetry in opposite sense, and their phase relation close to the resonance deviates from the phase relation far from the resonance frequency. The coherence has a maximum at the resonance frequency, and two characteristic dips of different extent to its left and to its right. In figure II.6 we saw that the pure oscillation can not have a different sign in asymmetry in velocity and intensity. Therefore, the model for the power spectra needs to be extended in a physically motivated way. In the following section we will introduce the concept of “correlated

noise”, a concept which is based on simulations of the upper solar convection zone.

### II.3.2 Modelling Power and Cross Spectra

The (complex) eigenfrequency of the mode displayed in figure II.10 has been calculated by solving the nonadiabatic equations (A.1)–(A.5) with the solar model of Provost, Berthomieu, & Morel (2000) without a source term. The calculated frequency has a real part of 2.1042 mHz and an imaginary part of 0.245  $\mu$ Hz.

Neither central frequency nor width of the theoretically calculated power spectra correspond exactly to the observed value. The small deviation of the frequency is taken into account by shifting the frequency scale by roughly 0.6  $\mu$ Hz. The width of the peaks is considerably underestimated by the calculated imaginary part of the eigenfrequency. Therefore, the imaginary part has to be adjusted to the observed width of the peaks. For the modes under consideration, an imaginary part between 0.4  $\mu$ Hz and 0.5  $\mu$ Hz turned out to give satisfactory results. There is a wide variety of possible damping mechanisms, which are difficult to include in the formalism. The coupling of modes to turbulent convection introduces additional damping, as well as a possible coupling of the modes to Alfvén waves. Adjusting the imaginary part of the frequency is a phenomenological approach to take additional damping into account and to make fits possible.

With the customization described above, we construct a model for the observed spectra. The peak shape of the power spectra are governed by  $V_l$  and  $I_l$  which are the nonadiabatic Green’s functions for velocity and luminosity, respectively, and the correlated noise components  $c_V^{corr}$  and  $c_I^{corr}$ , which model the visible imprint of the excitation process on the surface. The model is given by

$$P_V^l = |V_l + c_V^{corr}|^2 + |c_V^{coh}|^2 + |c_V^{uncoh}|^2, \quad (\text{II.19})$$

$$P_I^l = |I_l + c_I^{corr}|^2 + |c_I^{coh}|^2 + |c_I^{uncoh}|^2, \quad (\text{II.20})$$

$$\Phi^l = \arg \left( (I_l + c_I^{corr})(V_l + c_V^{corr})^* + c_I^{coh}(c_V^{coh})^* \right), \quad (\text{II.21})$$

$$\rho^l = \frac{|(I_l + c_I^{corr})(V_l + c_V^{corr})^* + c_I^{coh}(c_V^{coh})^*|}{\sqrt{P_I^l P_V^l}}. \quad (\text{II.22})$$

$c_V^{coh}$  and  $c_I^{coh}$  play a substantial role in modelling the phase and coherence. Most parts of the intensity and velocity signal are coherent, i.e. they have a fixed phase relation between velocity and intensity, but only a small fraction of it has fixed phase relation to the oscillation. This fraction (represented by  $c_V^{corr}$  and  $c_I^{corr}$ ) is assumed to be caused by a surface process which is correlated to the mode excitation process. Through the interference term, correlated noise is able to modify the shape of the power spectrum peaks.  $c_V^{uncoh}$  and  $c_I^{uncoh}$  represent the fraction of both signals without fixed phase relation, being due to nonlinear processes of granulation and instrumental noise.

### II.3.3 Previous Results

There have been various efforts to infer the source properties from the power and cross spectra in recent times. Abrams & Kumar (1996) first used the potential well model to explain the observed asymmetry in mode peaks. Chaplin & Appourchaux (1999) fitted low- $l$  velocity and intensity power spectra with a correlated component only in intensity, and found amplitudes of the correlated component in intensity between 1% and 6% of the modes' peak heights. In their paper, the source depth depends strongly on frequency, in a range between 100 km and 500 km below the photospheric level. Abrams & Kumar (1996) (p-modes in velocity) and Kumar (1994) (pseudo-modes in intensity) fitted nonadiabatic Green's functions to observed spectra, and found an excitation depth between 325 km and 525 km (p-modes), and  $140 \text{ km} \pm 60 \text{ km}$  (pseudo-modes). Nigam (1999) found an excitation depth of 75 km, using a combination of monopole and quadrupole sources exciting adiabatic oscillations. Kumar & Basu (1999a) reinvestigated the low frequency velocity spectrum with more advanced solar models, and found a source depth between 120 km and 350 km for a dipole source, and a much deeper source between 700 km and 1050 km in the case of a quadrupole source. None of these publications includes the possibility of a correlated component in velocity. All this shows, that the estimated source depth depends strongly on the solar model used and on the applied approximations for the model for the resonance.

Severino et al. (2001) established the model for the power and cross spectra given by equations (II.19)–(II.22), but used Lorentzian p-mode profiles for the resonance, disregarding the source. Their estimates of the correlated components can therefore be regarded as unreliable. Jefferies et al. (1999) extended this approach by using the two wave interference model to account for the localized source. They showed that for their simple model it is mathematically impossible to disentangle source depth and noise parameters. For numerically calculated resonances this is no longer strictly true, but it will be shown below, that it is not possible to give independent estimates of the source depth and the correlated noise components. However, it is possible to



give inequalities for the source depth, as well as reliable estimates for amplitudes and phases of several noise parameters.

Georgobiani, Stein & Nordlund (2003) pursued a completely different approach to explain the asymmetry reversal in helioseismic spectra. They simulated a small box in the upper layer of the solar convection zone. Instead of calculating temperature and velocity spectra at constant geometrical depth, they looked at the signal at constant optical depth, which accounts for the observation height varying with the oscillation. This leads to a substantial reduction of the temperature fluctuations, and to a reversal of asymmetry in the temperature spectra. However, they point out that they had unrealistically high mode amplitudes. Considering that the effect is predominantly due to the nonlinear dependence of the  $H^-$  opacity on temperature, radiative transport, not correlated noise, seems to determine the shape of the p-mode peaks. This will be discussed in greater detail in Section II.6, where mode spectra are calculated by radiative transfer calculations.

### II.3.4 Source Depth and Noise Parameters from Power and Cross Spectra

Fits to the model given by equations (II.19) through (II.22) have been performed for the modes  $n = 8$ ,  $l = 21 \dots 25$  in the frequency range 2.077 mHz ( $l = 21$ ) through 2.182 mHz ( $l = 25$ ).  $V_l$  and  $I_l$  are represented by the nonadiabatic Green's function for velocity and luminosity, respectively (dipole source), or its derivative with respect to the source depth (quadrupole source). It takes substantial computation time to calculate the theoretical spectrum with the necessary frequency resolution. Therefore, the spectra have been calculated for different source depths between -200 km and +500 km with a step size of 20 km. Both shape and mutual phase of the spectra are almost identical whether the full set of equations is solved or the Cowling approximation is applied. In order to save two thirds of the calculation time, we calculated the spectra in the Cowling approximation.

For each of these calculated spectra, least square fits to all four observed spectra have been performed. The squared deviations have been weighted according to the variance in the flat frequency bands far from the resonance. The nonlinear optimization method *amoeba* has been used to find a set of 11 parameters — 2 mode amplitudes, 6 noise amplitudes, and 3 phases — that fits the model to the observed spectrum. *amoeba* is a simplex downhill method described in Press et al. (1986). In order to check if the fitted parameter set really represents a global minimum, we also used the genetic algorithm *pikaia* (Charbonneau, 1995) which works independent of initial guesses. This optimization worked less efficiently for this particular problem, but was

able to reproduce the results obtained from *amoeba*.

As the most important result it must be asserted that the source depth can *not* be unambiguously determined from the power and cross spectra. Although the model is sensitive to all parameters, good fits, like the one displayed in figure II.11, occur for all source depths below the solar radius.

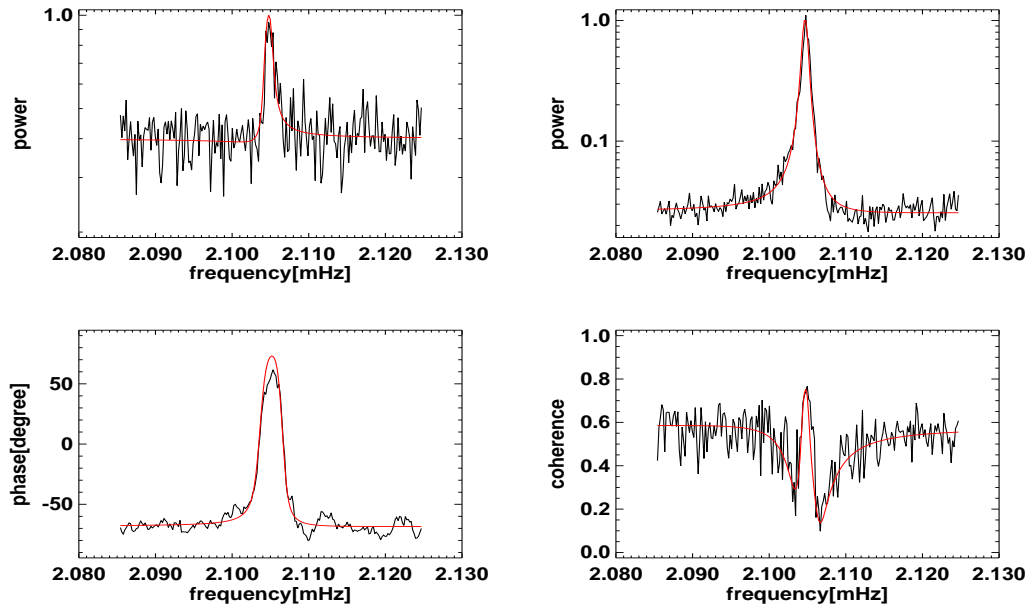


**Figure II.11:** Fitted power and cross spectra of intensity (upper left), velocity (upper right), phase (lower left) and coherence (lower right), for the  $l = 22$ ,  $n = 8$  mode. The power spectra are normalized to their maxima. Fits of the displayed quality without substantial systematic deviations occur for many sets of parameters. They are referred to as “good fits”.

### a) Results for a Dipole Source

The estimation of the source depth obtained from fitting the model given by equations (II.19)–(II.22) is rather poor — only a source depth above the solar radius can be excluded. For all positive depths we obtain good fits (see figure II.12, left panel). However, the fraction of correlated noise in velocity can be roughly estimated without detailed assumptions about the depth of the source.

The calculated spectra for the pure oscillation change only slightly in the range of source depths between +100 km and +500 km. Therefore, the parameter estimation shows little variation in this range of depths, and the error bars will be estimated from the distribution of the parameters there. These estimates reflect probably more accurately the true variance of the parameters than the formal errors of the fits obtained from the inverted Hessian matrix.

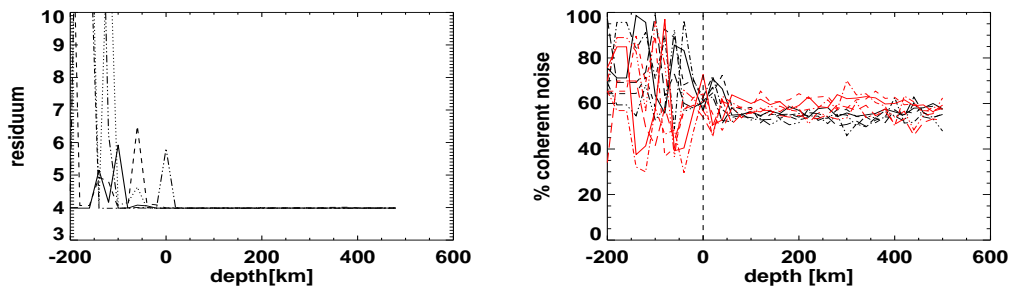


**Figure II.12:** *Left panel:* Residuum of the fits obtained for different depths, for the modes  $n = 8$ ,  $l = 21 \dots 25$ . A value of four represents an optimal fit: It can be achieved for sources deeper than 0 km. *Right panel:* Fraction of total coherent noise  $|c^{corr}|^2 + |c^{coh}|^2$  in percent of the total additive background. The black lines represent intensity, whereas the red lines represent velocity. Good fits occur for source depths right of the vertical dashed line. The values for  $l = 21$  through  $l = 25$  (for both panels) are displayed as: solid line (21), dotted line (22), dashed line (23), dash-dot-dashed line (24), dashed-dotted line (25).

We see in figure II.13, that the correlated component in velocity is so small that only an upper limit of about 1% of the total noise can be given. The correlated component in intensity is consistently higher. For an assumed source depth below +100 km, the fraction of correlated noise in intensity is  $5\% \pm 1\%$ . It is important to note that between 0 km and +100 km good fits occur, but a higher fraction of correlated noise in intensity (up to 20%) is necessary in order to reproduce the observed spectra with these source depths. For the velocity spectra, the correlated noise fraction remains small, but we have to raise the upper limit to about 2%.

Figures 14 and 15 of Stein & Nordlund (2001) show, that the strong pressure fluctuations which occur in numerical simulations of convection and which are probably linked to seismic events, are concentrated in intergranular lanes and at the edge of granules. Correlated surface fluctuation from radiative cooling can probably be interpreted as correlated noise. This means that the area where granulation noise is correlated to the excitation source covers only a small fraction of the solar surface. This is consistent with a uncorrelated component being much higher than the correlated component in both spectra. Figure 23 and 24 of Stein & Nordlund (2001) show, that the nonadiabatic perturbations which are associated with the excitation process hardly reach the observation height of the MDI line. Even if parts of these perturbations were visible at this height, it is important to consider the fact that the area covered by a MDI pixel is of the same order of magnitude as the horizontal scale of a granule. Therefore, velocity perturbations from rapid downdrafts, which are extended over an area much smaller than a granule are suppressed by the intensity weighted averaging for each pixel. Our estimates for the fraction of correlated noise reveal qualitatively what is expected from

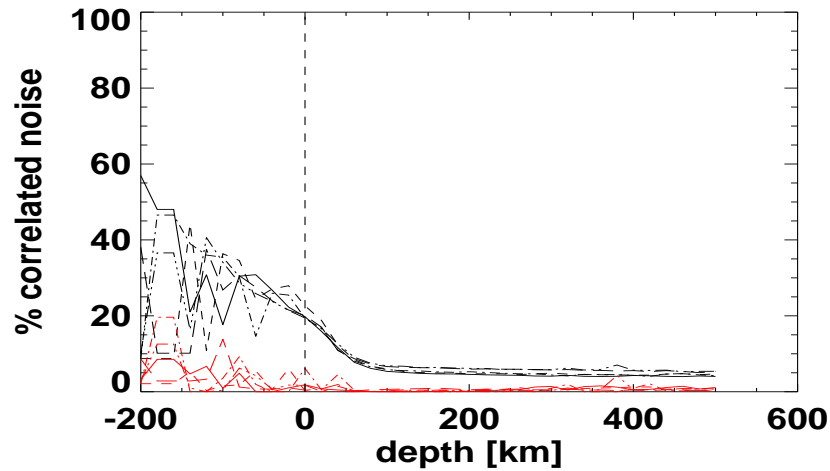


**Figure II.13:** Fitted fraction for the correlated noise in intensity (black lines) and velocity (red lines). For all source depths right of the dashed vertical line, the power and cross spectra can be successfully fitted to the model. For the assignment of line-styles and angular degrees, see figure II.12.

the currently available simulations of solar convection. A quantitative evaluation of these simulations in terms of the ratio of correlated and total intensity fluctuations would definitely be helpful.

Figure II.12 (right panel) shows the total fraction of coherent noise, i.e.  $|c^{corr}|^2 + |c^{coh}|^2$ . It is  $56\% \pm 4\%$  in intensity, and  $58\% \pm 5\%$  in velocity, and therefore equal within the error bars.

In figure II.14, the fitted phases for the correlated intensity noise and the mutual phase of the coherent, uncorrelated components in intensity and velocity are shown. The phase of the correlated component in velocity is missing in the plot because the component's amplitude is simply too small to fit the phase reliably. However, the well estimated phase of the correlated component in intensity ( $-162^\circ \pm 7^\circ$ ) gives very valuable information about the excitation process. Figure II.15 shows that the phase of the intensity is close to phase opposition relative to the resonance-phase of the velocity Green's function representing the oscillation. Bearing in mind that positive velocities are inward directed, we see that the negative intensity contribution is slightly ahead of the inward velocity with an additional phase offset of  $18^\circ \pm 7^\circ$ . This offset can be interpreted as the delay of the response to the excitation. The observed values of the phase agree with excitation of p-modes by dark downdrafting plumes.

The uncorrelated component has a phase difference of  $-67^\circ \pm 2^\circ$ , where the intensity component is leading the velocity component. This phase difference is of opposite sign compared to the phase difference in an adiabatic acoustic resonance. There is

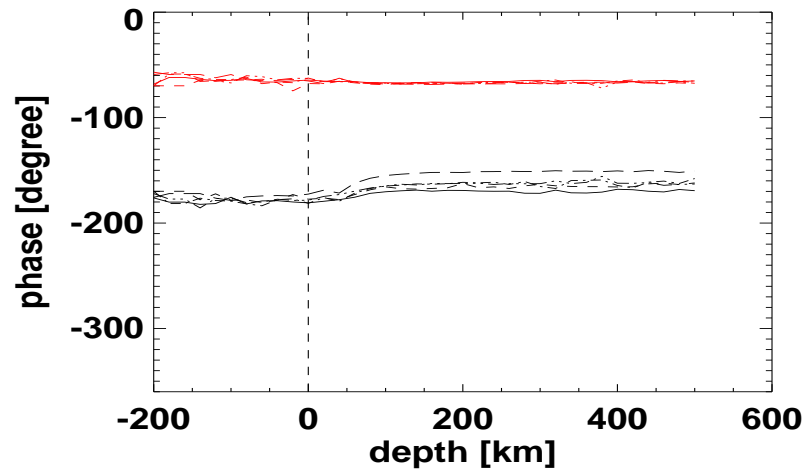


**Figure II.14:** Phase lag of the mode-correlated component in intensity (black lines), and the relative phase of the not-mode-correlated components in velocity and intensity (red lines). The line shapes are described in the caption of figure II.12. Good fits occur to the right of the vertical dashed line.

no simple explanation for this phase difference, but as pointed out by Oliviero et al. (1999), the negative phase can qualitatively be revealed by numerical simulation of granulation.

Figures II.16 and II.17 give a simple interpretation of the obtained phase spectrum. There is a negative intensity-velocity phase difference of  $-66.7^\circ \pm 3.8^\circ$  far from the resonance. This corresponds simply to the phase difference of the coherent-uncorrelated component. The correlated component is much smaller, and plays only a minor role. The observed value of about  $65^\circ$  right at the resonance is very close to the phase difference for a pure oscillation spectrum, calculated from the nonadiabatic equations for a source deeper than  $+100 \text{ km}$ <sup>3</sup>. For an assumed source depth between 0 km and  $+100 \text{ km}$ , an increased fraction of correlated intensity noise may compensate for the phase difference (see figure II.13). Because the adiabatic phase difference between temperature and velocity is  $90^\circ$ , there have been discussions about the origin of the reduced phase difference. Correlated noise has been held responsible for this deviation (Jimenez et al., 1999; Nigam, 1999). We have shown, that correlated noise is not needed to explain the mutual phase of velocity and intensity oscillations: The nonadiabatic treatment of the oscillations seems to explain most of the observed phase difference. It is needed however to explain the reversed asymmetry in the mode peaks of intensity spectra.

<sup>3</sup>Note that the remarkable behavior of the calculated phase of the pure oscillation far to the right of the resonance is unimportant for the model of power and cross spectra, because at these frequencies the spectra are almost completely dominated by the noise.

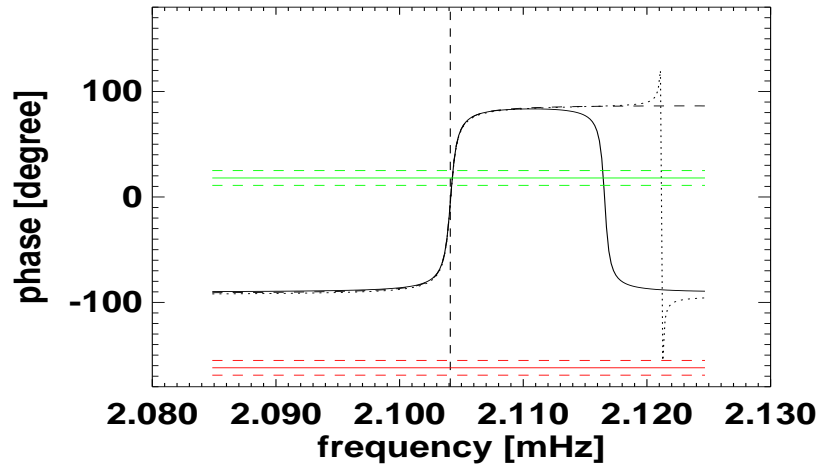


**Figure II.15:** Black lines: phases of the velocity Green's functions for source depth 0 km (solid line), +100 km (dotted line), and +500 km (dashed) line; red lines: phase of the correlated intensity; green lines: the same phase shifted by  $180^\circ$ . It indicates the phase of the negative intensity variation. Dashed lines indicate the errors.

Figure II.17 shows, that the mutual phase of the nonadiabatic Green's functions hit the observed phases reasonably well in the frequency band between roughly 2 mHz and 3 mHz. Below that band, the signal-to-noise ratio in the intensity spectra is very low, so that the phases are substantially influenced by the noise even at the resonances. For higher frequencies, the observed phase drifts away towards higher values. We explain this behavior by the increased influence of the superadiabatic surface layer at higher frequencies, which is not properly treated in the solar model, as indicated by the differences in the resonance frequencies displayed in figure II.7.

### b) Fitting Modes with a Quadrupole Source

In a next step we looked for the dependence of the estimated parameters on the assumed dominant multipole moment of the source. Following equation (II.2),  $I_l$  and  $V_l$  are represented by the first derivatives of the Green's functions with respect to the source depth. Again there is no unique estimate of the source depth. Furthermore, the parameters for correlated noise amplitudes and phases are very close to the estimates for the dipole case. The main difference is that there are two ranges of source depths where good fits occur: Above -100 km and below +120 km. Excitation by turbulent convection can not occur in the convectively stable photosphere. Further, an excitation in this zone would be rather ineffective because of the low mode energy density there. Therefore, we discard source depths above -100 km.

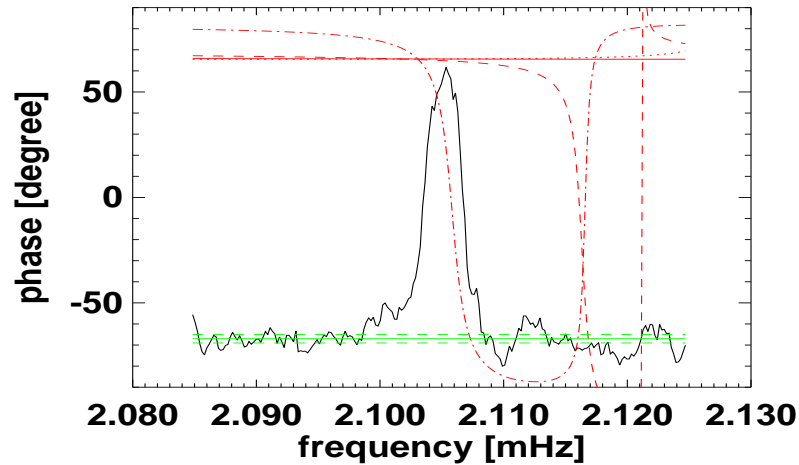


**Figure II.16:** Observed phase difference (black line) of the  $l = 22$ ,  $n = 8$  mode, the phase of the coherent, uncorrelated background (green lines), and the relative phase of the pure oscillation spectrum (red lines) for source depth of 0 km (dashed dotted line), +100 km (dashed line), +300 km (dotted line), and +500 km (solid line). Dashed lines indicate the errors. The calculated phase at the resonance fits the observed phase for source depths deeper than 0 km.

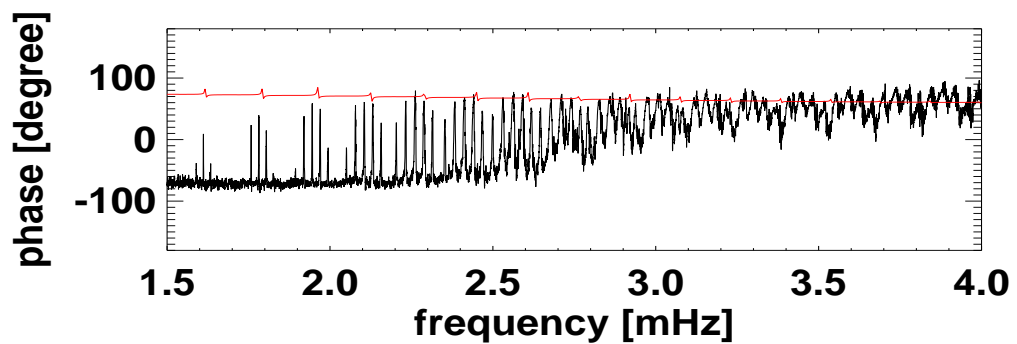


**Figure II.17:** Mutual phase of the observed  $l = 22$  spectra for intensity and velocity (black line), and the phase of the respective phase of the nonadiabatic Green's function of velocity and luminosity for source depth +500 km. Note, that each target mode is encircled by neighboring  $l$  modes leaking into the spectrum.

Chaplin & Appourchaux (1999) showed in detail for potential well Green's functions that the position of the source relative to the nodes of the eigenfunctions largely determines the mode asymmetry. This means that fitting the spectra to models containing the Green's functions can provide a specification of the source depth on length scales below the radial mode wavelength. Rough estimates for the source location have to be obtained from physical considerations.

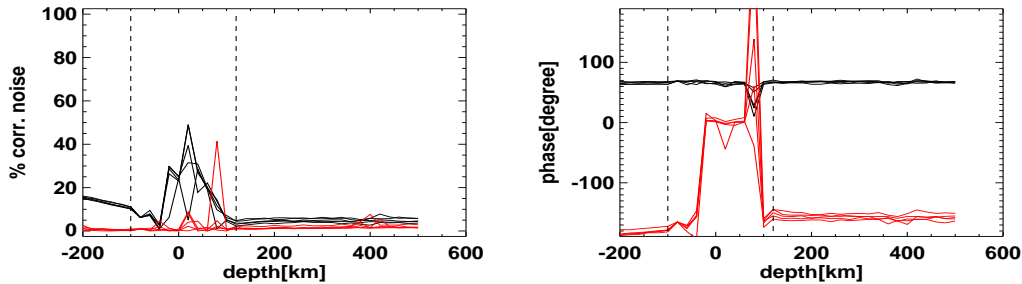


**Figure II.18:** Parameters estimated from fits with a quadrupole source. Fits between the two vertical dashed lines failed, all other fits have good quality. *Left panel:* Fraction of correlated noise in intensity (black lines) and velocity (red lines). *Right panel:* Mutual phase of the coherent, uncorrelated components (black lines), and phases of the correlated components in intensity (red lines). The results are very close to the results for a dipole source (see figures II.13 and II.14).

Figure II.18 shows that again the fraction of correlated noise is significantly lower in velocity ( $2\% \pm 1\%$ ) than in intensity ( $5\% \pm 1\%$ ). Further, the results for the phases are almost identical with the ones obtained for a dipole source ( $-67^\circ \pm 2^\circ$  for the mutual intensity-velocity phase of the uncorrelated part,  $-157^\circ \pm 5^\circ$  for the phase of the correlated intensity component; the corresponding velocity component can not be stably fitted).

The only real significant difference between the dipole case and the quadrupole case is that stable fits occur only below +120 km, whereas in the dipole case they occur for all depths below 0 km.

## II.4 Fitting Pseudo-Mode Spectra

For the p-mode spectrum, we have seen that shifting the source depth and varying the fraction of correlated noise cause similar modifications in the p-mode spectrum. The same is true for the pseudo-mode spectrum. Therefore, fitting pseudo-mode spectra is a complimentary approach to fitting the shape of p-mode peaks. The modification of the power and cross spectra by the varying parameters (source depth and noise parameters) occurs qualitatively in a different way: While the peaks in the p-mode power spectra are only changed in shape but not in frequency, the peak frequencies of



	Dipole $0 \text{ km} < d < 100 \text{ km}$	Dipole $d > 100 \text{ km}$	Quadrupole $d > 120 \text{ km}$
$ c_I^{corr} ^2$	$(5 - 20)\%$	$(5 \pm 1)\%$	$(5 \pm 1)\%$
$ c_V^{corr} ^2$	$< 2\%$	$< 1\%$	$(2 \pm 1)\%$
$ c_I^{corr} ^2 +  c_I^{coh} ^2$	$(56 \pm 4)\%$	$(56 \pm 4)\%$	$(55 \pm 4)\%$
$ c_V^{corr} ^2 +  c_V^{coh} ^2$	$(58 \pm 5)\%$	$(58 \pm 5)\%$	$(58 \pm 3)\%$
$\arg(c_I^{corr})$	$(-162 \pm 7)^\circ$	$(-162 \pm 7)^\circ$	$(-157 \pm 5)^\circ$
$\arg(c_V^{corr})$	—	—	—
$\arg(c_I^{coh}(c_V^{coh})^*)$	$(-67 \pm 2)^\circ$	$(-67 \pm 2)^\circ$	$(-67 \pm 2)^\circ$

**Table II.1:** Best fits for the noise parameters for dipole and quadrupole sources.  $d = R - r_S$  is the source depth. The squared absolute values are given in percentage of the total additive background.

the pseudo-modes can be shifted as well. As shown in figure II.19, the positions of the maxima are indeed mutually shifted in the power spectra of intensity and velocity. The shape of the pseudo-mode power peaks, as well as their structure in the cross spectra, is not as pronounced as for the p-modes, and contains little information. Furthermore, the signal-to-noise ratio for the pseudo-modes can be enhanced substantially by adding correlated noise (Nigam, 1999).

Figure II.19 also shows that the maxima of the mutual phase occur at the power minima of the velocity power spectra. This is contrary to the situation in the p-mode range (see also figure II.10 and Oliviero et al. (1999)).

In order to fit the model described by equations (II.19) through (II.22), we have to treat the mode leakage differently from low frequency p-modes. Whereas  $m$ -leakage does not play a substantial role because of the smooth broadband structure of the pseudo-mode range,  $l$ -leakage becomes important because the width of the peaks are comparable to their mutual distance. The method how to treat the leakage is described

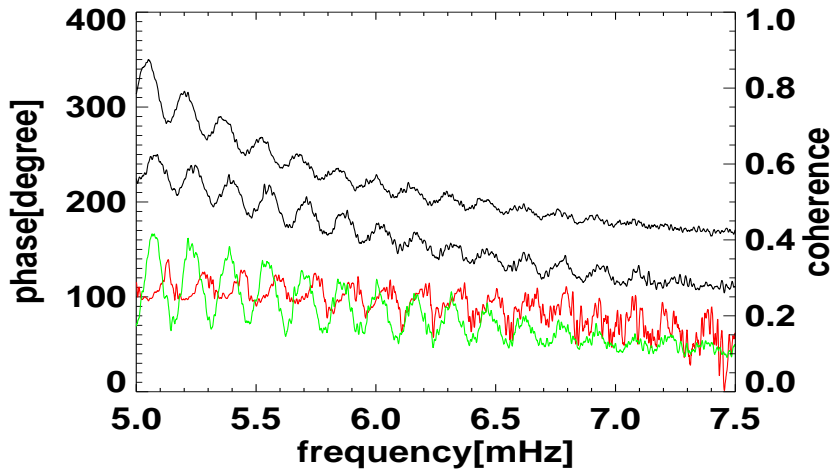


**Figure II.19:** Pseudo-mode power spectra for velocity (upper black line) and intensity (lower black line), the mutual coherence (green line), and the mutual phase (red line) for a  $l = 44$  spectrum. The scale for the power spectra is arbitrary.

in Appendix C.

The fact that the fitted section of the spectra has to be of the order of at least 1 mHz makes finding a physically reasonable model much more problematic compared to low frequency p-mode fitting. Frequency independence of all parameters is maybe not a good assumption over that range of frequency. Furthermore, pseudo-modes, like high frequency p-modes, are heavily influenced by the uncertainties in the description of the surface layer of the solar model, so that the theoretical spectra are probably not an adequate description of the observations. Kumar (1994) calculated nonadiabatic Green's functions from a solar model and successfully fitted pseudo-mode spectra of intensity measurements with a frequency dependence of  $\omega^{-7.5}$  of the excitation strength, assuming only an additive background in the power spectrum. Although, as shown in figure II.4, mutually shifted peaks in velocity and intensity spectra can occur as a result of a very shallow source depth, the observed shifts in the four power and cross spectra, as displayed in figure II.19, could *not* be explained by the model of Kumar (1994). Even with (frequency independent) correlated noise components, it turns out that it is not possible to fit the model simultaneously to all four spectra. This shows, that the oscillation functions have to be very accurate in order to fit the model given by equations (II.19)–(II.22) to the observed spectra. For high frequencies, our nonadiabatic Green's functions (which completely neglect convective flux) can not be expected to be accurate. A proper treatment of the convective energy flux, together with a physically motivated frequency dependence of the noise parameters can probably provide satisfactory fits. This could be the direction of future work.

## II.5 Fitting Low- $l$ Spectra

Data from the GOLF experiment (Gabriel et al., 1995) and the SPM instrument (Fröhlich et al., 1995) are the best choice for estimating the mode and noise parameters of low- $l$  spectra. Long time series with high filling factors (GOLF: 99.4 %, SPM blue: 98.0 %) are available. We chose GOLF and SPM blue data for 804 days, starting 1996, April 11. During this period, GOLF measured only in the blue wing of the Na D line due to a malfunction of the instrument. Therefore, the signal is not a differential signal and contains some contribution from intensity perturbations.

Power spectra obey simple  $\chi^2$  statistics, but phase and coherence have different, more complicated statistics. In order to get an approximately normal distribution for all spectra, we averaged the Fourier transforms over a frequency window of  $0.29 \mu\text{Hz}$ , which corresponds to 20 frequency bins. The hypothesis for the resulting distribution of all 4 spectra to be normal can be confirmed by the fact that the (normally distributed) estimators for the third and fourth moment are zero within the  $1\sigma$  level (van der Waerden, 1969). In order to avoid substantial bias, the frequency band should be smaller than any significant structure in the spectrum. Very similar results for least square fits for averaged power spectra, and maximum likelihood fits of the unaveraged power spectra support this assumption.

The estimators for intensity power, velocity power, phase, and coherence are obtained as follows

$$\hat{P}_I^0(v_i) = \frac{1}{(n+1)} \sum_{j=i-n/2}^{i+n/2} |i_0(v_j)|^2, \quad (\text{II.23})$$

$$\hat{P}_V^0(v_i) = \frac{1}{(n+1)} \sum_{j=i-n/2}^{i+n/2} |v_0(v_j)|^2, \quad (\text{II.24})$$

$$\hat{\Phi}^0(v_i) = \arg \sum_{j=i-n/2}^{i+n/2} i_0(v_j)(v_0(v_j))^*, \quad (\text{II.25})$$

$$\hat{\rho}^0(v_i) = \frac{\left| \frac{1}{(n+1)} \sum_{j=i-n/2}^{i+n/2} i_0(v_j)(v_0(v_j))^* \right|}{\sqrt{\hat{P}_I^0 \hat{P}_V^0}}, \quad (\text{II.26})$$

where  $n$  is the (even) number of frequency bins in the averaging window, and  $i = [\frac{1}{2}n, \frac{3}{2}n + 1, \frac{5}{2}n + 2, \dots]$ .

The spectra are modelled by the expressions (II.19)–(II.22), where  $I_l = I_{02}$  and  $V_l = V_{02}$  are given by:

$$I_{02}(\nu) = a_0^I I_0(\nu) + a_2^I \sum_{m=-2,0,2} b_m^I I_2(\nu + m \Delta\nu), \quad (\text{II.27})$$

$$V_{02}(\nu) = a_0^V V_0(\nu) + a_2^V \sum_{m=-2,0,2} b_m^V V_2(\nu + m \Delta\nu), \quad (\text{II.28})$$

where  $a_0^I, a_0^V, a_2^I, a_2^V$  are the amplitudes of the  $l = 0$  and  $l = 2$  modes, respectively, and the  $b$  coefficients are the fixed, calculated amplitude ratios between the  $m = \pm 2$  and the  $m = 0$  coefficients. Following Jiménez (2004), we set  $b_0^V = 0.71, b_0^I = 0.57$ , and  $b_{-2,2}^V = b_{-2,2}^I = 1$ .  $\Delta\nu$  was set to  $0.4 \mu\text{Hz}$ .

Single mode fitting is not possible for whole disk measurements because pairs of  $l = 0, l = 2$  modes, and pairs of  $l = 1, l = 3$  modes appear in the spectrum with a frequency separation of about  $10 \mu\text{Hz}$  and  $15 \mu\text{Hz}$ , respectively. Therefore, the modes leaking into the spectrum have to be included in the model. The leakage coefficients are real, and their amplitudes are fitted as a free parameter. For higher frequencies, the widths of the modes increase, whereas the distances between the pairs decrease. Therefore, the characteristic structures in phase and coherence for each single mode in the pair merge and finally smear out. A tradeoff between a reasonable signal-to-noise ratio and significant double peak mode structure suggests to fit modes in a frequency range between  $2.2$  and  $2.5 \text{ mHz}$  (see figure II.20). The low signal-to-noise ratio for the  $l = 3$  mode in the intensity spectrum suggests to choose a  $l = 0, l = 2$  pair instead of a  $l = 1, l = 3$  pair. Figure II.21 shows the modes  $(n, l) = (16, 0)$  and  $(n, l) = (15, 2)$  together with the best fitting model.

To model the spectrum we need to calculate the spectra of the pure oscillation. The spectra can be calculated with the same code as the medium- $l$  spectra in the preceding section. However, in the radial case  $l = 0$  the numerical code has to be slightly modified because of additional zeros in the central boundary condition. We note that the Cowling approximation has not been applied, because low- $l$  modes penetrate deep enough into the solar interior to feel the perturbation of the gravitational potential. We calculated the Green's functions in steps of  $20 \text{ km}$  in a range from  $-200$  to  $+500 \text{ km}$ . The  $l = 0$  mode had to be shifted by  $1.1 \mu\text{Hz}$  towards lower frequencies, and the  $l = 2$  mode by  $0.8 \mu\text{Hz}$  to fit the observations. To account for the intensity contribution to the GOLF signal, an additional parameter representing a possible phase offset of the velocity oscillation was introduced. Best fits occur if this parameter is set to about  $20^\circ$ .

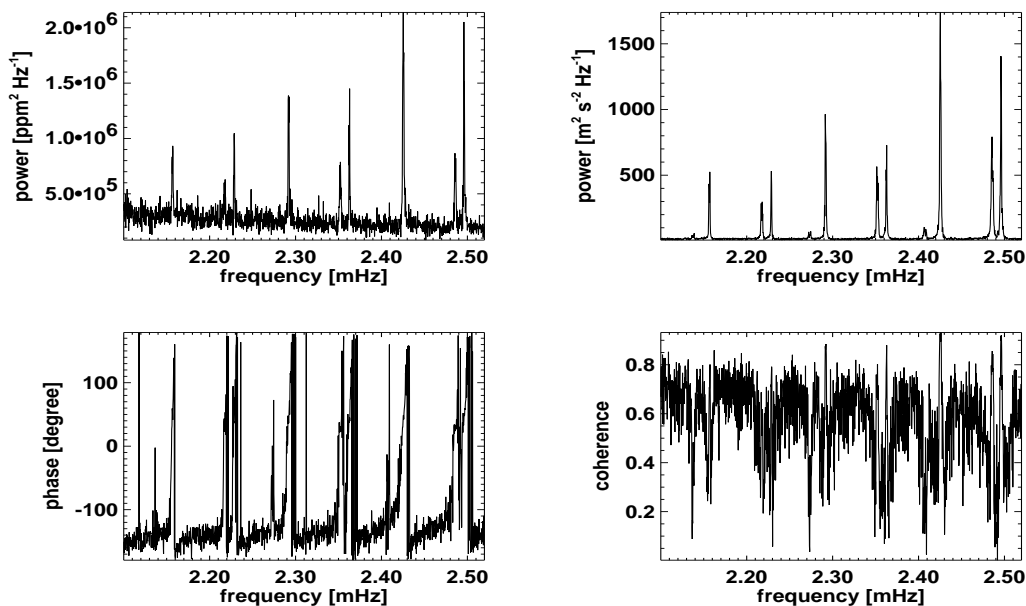


**Figure II.20:** Frequency averaged power spectra of intensity (upper left), velocity (upper right), and the mutual phase (lower left), and coherence (lower right) from 804 days of GOLF (velocity) and SPM blue (intensity) data. The identifiable modes in the velocity spectrum are (from left to right):  $(n, l) = (13, 3), (14, 1); (14, 2), (15, 0); (14, 3), (15, 1); (15, 2), (16, 0); (15, 3), (16, 1); (16, 2), (17, 0)$ .

As for medium- $l$  modes, source depths above the solar radius can be excluded (see figure II.23). The quality of the fits for source depths below the solar radius is shown in figure II.21. It shows that the model is not able to reproduce the observed spectra accurately. The mode profile has some deviation from the observed one in the wings. This leads to a substantial deviation of the spectra in the frequency band between the modes, where both wings overlap. In order to demonstrate that the error is not due to a biased estimate of the spectra through averaging, but due to an inappropriate mode profile, we compared two models fitted to the unaveraged GOLF power spectrum with maximum likelihood method (Toutain & Appourchaux, 1994). One fit is performed with a profile given by equation (II.7) (modified Lorentzian shape), and the other with the profile given by the nonadiabatic Green's function. Figure II.22 shows that the modified Lorentzian profile fits much better the estimator of the velocity power spectrum. Unfortunately the asymmetry parameter does not give direct information about physical quantities like source depth or correlated noise.

It is an interesting question why the mode profiles from the nonadiabatic Green's functions fit the observations for medium- $l$  spectra, but not for low- $l$  spectra. The most significant difference between the two spectra is the length of the underlying time series: While for medium- $l$ , we used two-month time series, for low- $l$  we used

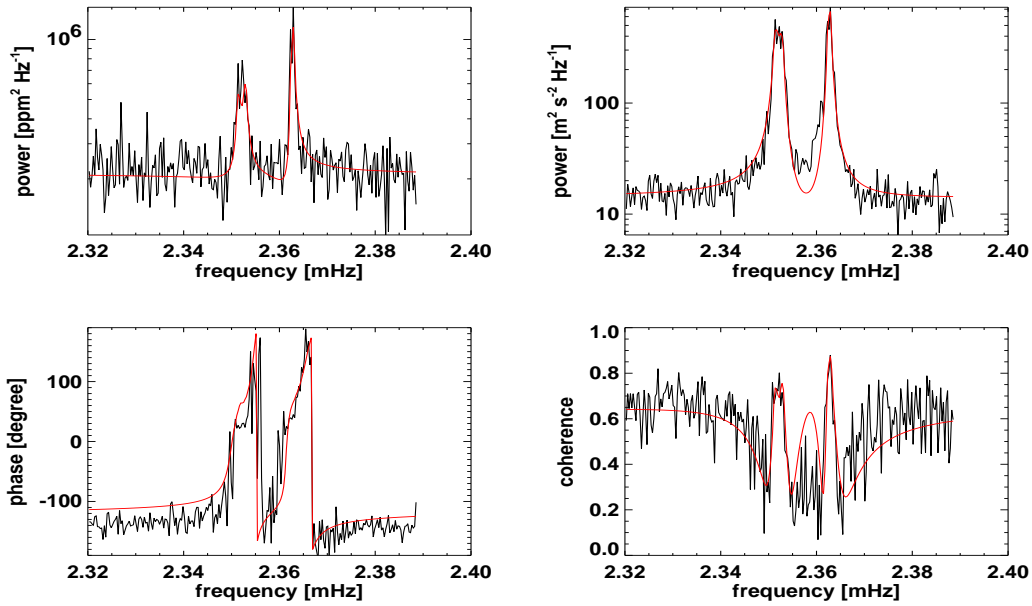


**Figure II.21:** Best fits for the mode-pair  $(n, l) = (16, 0)$  (right peak),  $(n, l) = (15, 2)$  (left peak) for the power spectra of intensity (upper left), velocity (upper right), the mutual phase (lower left) and the mutual coherence (lower right). The spectra are the same as in figure II.20 (in the indicated frequency range); the best-fitting model spectra are drawn with red lines.

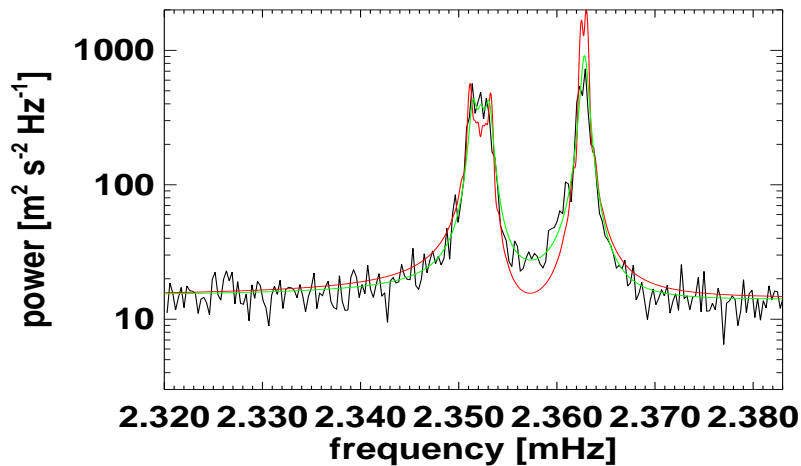


**Figure II.22:** Averaged GOLF power spectrum (black line) and the maximum likelihood fit (which has to be performed on the original (i.e. non-averaged) spectrum, which is not displayed here) with a modified Lorentzian profile (green line), and a profile of the nonadiabatic Green's function (red line).

time series with a length of more than two years. Solar cycle dependent changes of the mode's frequency, amplitude and width become important on a time scale of two years (Jiménez-Reyes et al. , 2003). An average over different mode amplitudes and widths definitely alters the observed shape of the modes.

Phase and amplitude of the coherent noncorrelated background component are almost independent of the mode profiles: for this, the best fit parameters for this component are credible. The parameters for the mode correlated noise however are definitely influenced by the mode profile. Therefore, the best fits for these parameters have to be treated with caution.

For the amplitude of the correlated noise component we find much higher values compared to our fits in the medium- $l$  case (see figure II.24). However, the big fluctuation in particular of the velocity component reflects the uncertainty of the fitted profiles.

The phase for the intensity component ( $-154^\circ \pm 10^\circ$ ) is almost the same as what we found for medium-degree modes. The phase of the velocity component, which could not be fitted for medium- $l$ , is  $24^\circ \pm 7^\circ$ . The phase for the background component is little influenced by the inappropriate line profile and can be given by  $-118^\circ \pm 5^\circ$ . This is significantly different from the result for medium- $l$ . The  $l$ -dependence of this phase gives subtle information about the physics of convection, but the discussion of this is beyond the scope of this work.

Unfortunately, the fits are not good enough to draw conclusions about the excitation process from the correlated noise coefficients. With more accurate models for the pure low- $l$  oscillations there may be a chance to infer reliable estimates for the correlated noise.

## II.6 Helioseismic Spectra Calculated by Radiative Transfer

Modes far below the acoustic cutoff frequency have upper turning points below the strongly superadiabatic surface layer. Therefore, mode frequencies and eigenfunctions are hardly influenced by this layer. However, perturbations of the continuum intensity are formed in a layer where the applied diffusion approximation for the radiation flux brakes down (Nordlund & Stein, 2001), and it is therefore not clear whether intensity oscillations are adequately described by the luminosity Green's functions. To get a more accurate description of the oscillation spectra, we performed radiative transfer calculations with solar atmospheres perturbed according to the nonadiabatic Green's functions of velocity, temperature, pressure, and density.

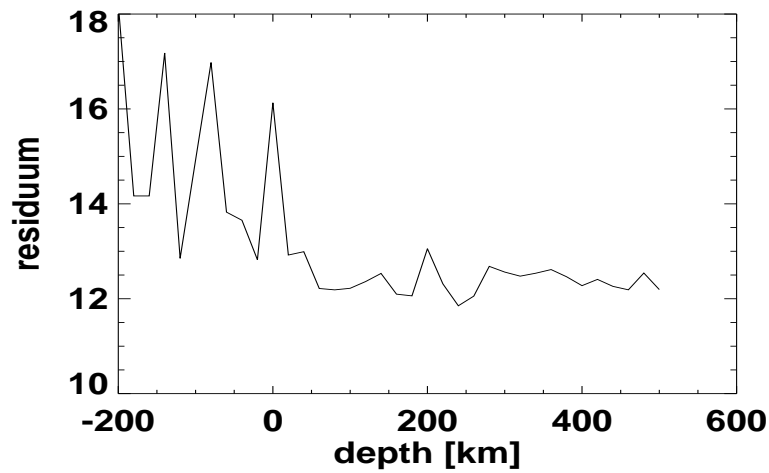


**Figure II.23:** Residuuum for the fits of the power and cross spectra. Fits of the quality displayed in figure II.21 occur for positive depths, i. e. all depths below the solar radius. Fits without systematic deviation would correspond to a value of four.

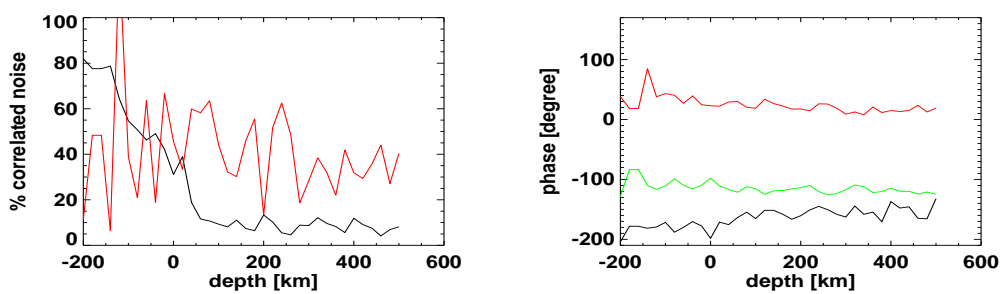


**Figure II.24:** *Left panel:* Fraction of correlated noise in intensity (black line) and velocity (red line). *Right panel:* Phases of the correlated component in intensity (black line), velocity (red line), and the mutual phase of intensity and velocity in the coherent, noncorrelated background (green line). Note, that the parameters for the correlated noise are probably not reliable because of the insufficient quality of the fits.



Other than velocity or intensity perturbations, the observed line depth perturbations are not directly linked to a physical quantity. Therefore, oscillations in the depth of the Ni I absorption line can not be immediately modelled by solving the set of equations (A.1)–(A.5). Being a differential signal like velocity, a uniform shift of both continuum and core intensity of the absorption line by a radially coherent temperature fluctuation will not be traceable in the line depth spectra. However, independent temperature fluctuations at the photosphere and at the observation height of the line's core (-300 km) will be visible in the line depth spectra. In order to infer the role of correlated noise in line depth spectra, we have to have a realistic model for the oscillations in line depth.

### II.6.1 Radiative Transfer Calculations

The physical quantities in a model atmosphere have to be modified according to the oscillations of velocity, pressure, temperature, and density. The modification have been applied from the edge of the model at -587 km down to +1500 km. A nonadiabatic  $l = 22$  Green's function spectrum for a source depth of +100 km was calculated for the entire frequency range from zero to the Nyquist frequency, and was brought to the time domain by a inverse Fourier transform. The radiation transfer code COSI (Hamann & Schmutz, 1987; Haberreiter & Schmutz, 2003) calculates the variation of the Ni I absorption line. The time varying absorption line has to be integrated with the five filter functions F0 . . . F4 displayed in figure I.5. The equations (I.29), (I.30), and (I.31) provide a time series for the MDI velocity, line depth, and intensity, respectively.

COSI is a radially symmetric code, solving simultaneously radiative transport equations and equations for the statistical equilibrium in non-local thermodynamic equilibrium (non-LTE). In order to save computation time, we restricted the code to local thermodynamic equilibrium, and changed the oscillator strength for the Ni I line from -2.17 to -2.53 to fit the line's depth to the depth of the observed Kitt peak absorption line (Wallace, Hinkle & Livingston, 1998). Figure II.25 compares the observed absorption line with the calculated absorption line for the unperturbed atmosphere. They do not agree perfectly, but as our approach is probably not extremely sensitive to the line's shape, the agreement may be sufficient.

The spectra are calculated with approximately realistic mode amplitudes. We used equilibrium quantities from the solar model of Provost, Berthomieu, & Morel (2000) and calculated the radiation transfer for the disk center in a wavelength band of 8 Å centered at 6768 Å with a resolution of 20 mÅ, considering only the Ni I transition at 6767.77 Å.

From the spectra we calculated *MDI velocity*, *MDI intensity*, and *MDI line depth*

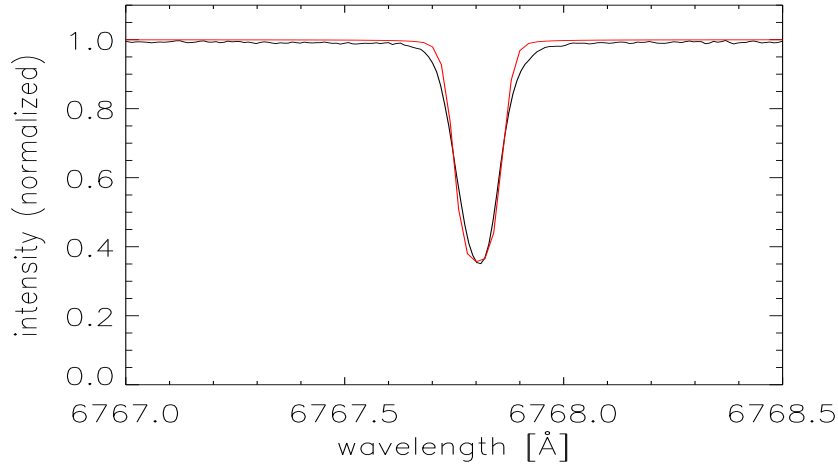


**Figure II.25:** Measure Kitt Peak absorption line (black line) and absorption line calculated by the radiative transfer code COSI (red line). Both lines are normalized to the continuum intensity.

via equations (I.29), (I.30), and (I.31), respectively. Additionally, we inferred a quantity called *real intensity* from the continuum in the neighborhood of the absorption line, and a quantity called *real line depth*, defined as continuum intensity minus minimum intensity in the calculated wavelength band.

For validation, we compared the *MDI velocity* with the input velocity at the line center observation height -300 km. Figure II.26 shows that velocity spectra obtained from radiative transfer agree perfectly with the input velocity at -300 km. This can be seen as a validation of the effective observation height. Because of the good agreement, we will not distinguish between velocity and *MDI velocity* in the remainder.

*MDI line depth* spectra showed a very high level of numerical noise. The reason for this is currently unclear. Therefore, we generally chose the *real line depth* spectra to represent line depth oscillations.

## II.6.2 Intensity Spectra from Radiation Transfer Model

Note, that the calculated radiation flux always reflects an effective observation height which corresponds to an optical depth  $\tau \approx 1$ . The oscillation spectra obtained from a radiation transfer code therefore always mimic the observation at constant optical depth. Georgobiani, Stein & Nordlund (2003) found a reversal of the asymmetry in intensity peaks if the observation height changes from constant geometrical depth to constant optical depth. They attribute this effect to the nonlinear dependence of the  $H^-$  opacity on temperature. COSI accounts for this dependence, so that the sensitivity of a pure oscillation to the  $H^-$  opacity changes can be investigated with our approach.

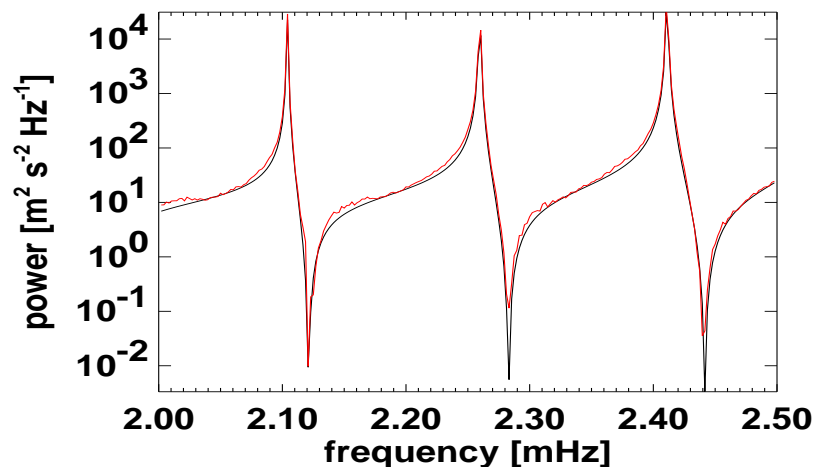


**Figure II.26:** Input velocity at the observation height -300 km (black line) and *MDI velocity* (red line). The peaks represent the modes  $l = 22$ ,  $n = 8, 9, 10$  (from left to right).

We found the same asymmetry for *real intensity*, *MDI intensity*, and the luminosity Green’s function. In the upper two orders of magnitude which are important for the fits, we found exactly the same asymmetry for this three spectra (see figure II.27), although the luminosity Green’s function refers to constant geometrical depth, whereas the *real intensity* and the *MDI intensity* refer to constant optical depth. This can be regarded as a confirmation that correlated noise is indeed responsible for the observed reversal of asymmetry, as assumed in the preceding sections.

Our approach is substantially different from the approach of Georgobiani, Stein & Nordlund (2003). They performed 3-dimensional simulations of the “Sun in a box”, i.e. a small portion of the upper solar convection zone. Besides convective motion, oscillation modes arise as eigenmodes of the box. These modes correspond to global solar modes with radial and horizontal nodes at the boundaries of the box, but exceed the amplitudes of observed modes substantially. Because of the small size of the box (6 Mm  $\times$  6 Mm horizontally and 3 Mm radially), only high- $l$  modes ( $l \approx 740$ ) are discernable in the spectra. These modes do not penetrate very deeply into the Sun, so that compared to medium- $l$  modes their global properties might be much more influenced by the complex radiation transfer in the upper convection zone. The validity of their result for medium- $l$  and low- $l$  modes with realistic amplitudes is therefore questionable.

Our calculations, in contrast, are able to give the peak shape of medium- $l$  modes, but suffers from certain inconsistencies: The Green’s functions are calculated assuming the diffusion approximation for radiative transport to be valid for the entire Sun including the upper convection zone. The detailed radiation transfer was calculated

with these erroneous perturbation functions. Furthermore, our radiative transfer calculations are radial and can not consider the effect of horizontal convective motions on radiation transfer. The horizontal variation from the spherical harmonic oscillation pattern is also neglected. These calculations should be regarded as a first approach towards a more accurate description. A more detailed investigation of this problem will be crucial for a deeper understanding of p-mode spectra.

### II.6.3 *Real Intensity Oscillations versus MDI Intensity Oscillations*

In this subsection, we compare the phase of *real intensity* oscillations and the *MDI intensity* oscillations with the observed intensity. The *MDI-intensity* is expected to reproduce the observed intensity better than the *real intensity*. However, the *real intensity* should be very close to the luminosity Green's function used in the previous Sections. Figure II.28 compares three mutual phases for a source depth +100 km: The velocity-luminosity phase from the nonadiabatic Green's function, the mutual phase of velocity and *MDI-intensity*, and the mutual phase of velocity and *real intensity*. As expected, the luminosity function represents the *real intensity* reasonably well at the resonance frequencies, but the *MDI-intensity* has a slightly different phase relative to velocity. In Section II.3 we argued, that the contribution of the correlated noise is rather small, because the mutual phase of the observed intensity and velocity at the resonance is very close to the phase of the respective nonadiabatic Green's functions of velocity and luminosity. Figure II.28 suggests a higher deviation, if the observed intensity is modelled by the *MDI intensity*. This means, that the fraction of correlated noise is probably slightly underestimated by the fits performed in Section II.3.

It is important to note that the *MDI-intensity* and *real intensity* are calculated for the disk center. For a more accurate estimation of the mutual phase, radiative transfer calculations covering the entire solar disk and successive disk integration with the spherical harmonic mask would be necessary. This could account for the solar disk variation of the geometrical depth corresponding to  $\tau = 1$ . We conclude that the estimates for the fraction of correlated noise depend critically on the details of the fitted model for the oscillation. Simple models can not be expected to give reliable results. Further refinement of the models is necessary.

### II.6.4 *Comparison of Intensity, Velocity, and Line Depth Spectra*

Figure II.29 shows the profiles of the modes  $l = 22$ ,  $n = 8, 9, 10$  in velocity, intensity and line depth for a excitation depth of +100 km, calculated with the radiation transfer code COSI. They are very similar in the upper two orders of magnitude which are

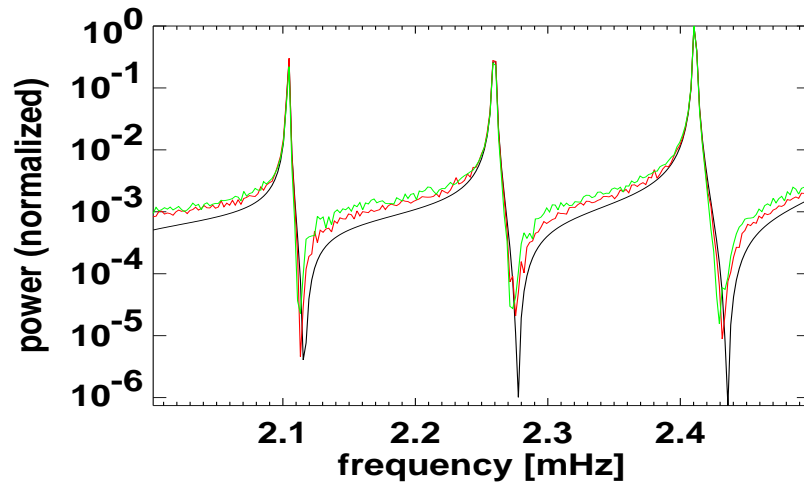


**Figure II.27:** Luminosity power spectrum at constant observation height -300 km (black line), the *MDI intensity* spectrum (red line), and the *real intensity* spectrum (green line). The peaks represent the modes  $l = 22$ ,  $n = 8, 9, 10$  (from left to right). The power is normalized to the maximum of each spectrum.

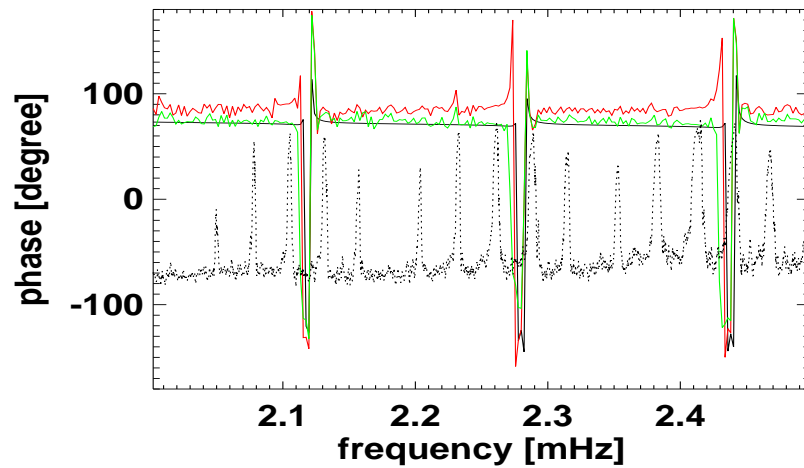


**Figure II.28:** Luminosity-velocity phase of the nonadiabatic greens function for source depth +100 km (black line), the mutual phase of *MDI intensity* and velocity (red line), and the mutual phase of *real intensity* and velocity (green line). The observed spectra are displayed with black dotted lines. Note that the target modes ( $l = 22$ ) at 2.105 mHz, 2.260 mHz, and 2.411 mHz are encircled by modes from neighboring  $l$  leaking into the spectrum. The phase of the target mode hits the phase of *real intensity* very well, but the *MDI intensity* has a substantial deviation.

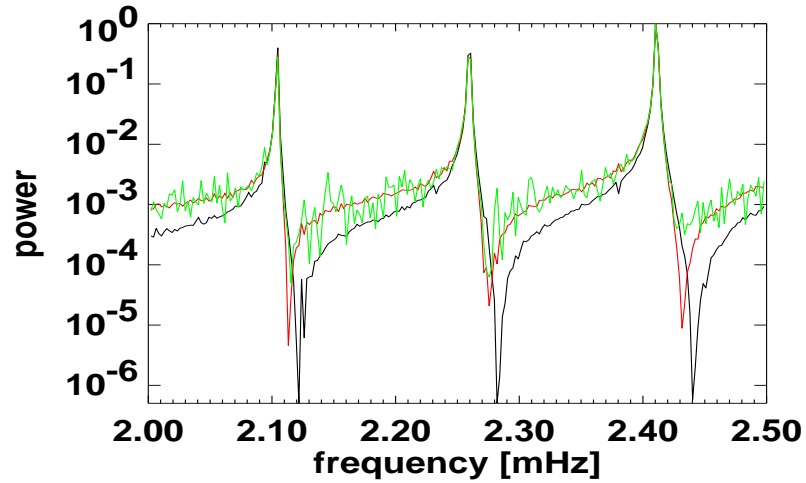


**Figure II.29:** The modes  $l = 22, n = 8, 9, 10$  for velocity (black line), *real intensity* (red line), and *real line depth* (green line), for an excitation depth of +100 km. The spectra have been normalized to their maxima.

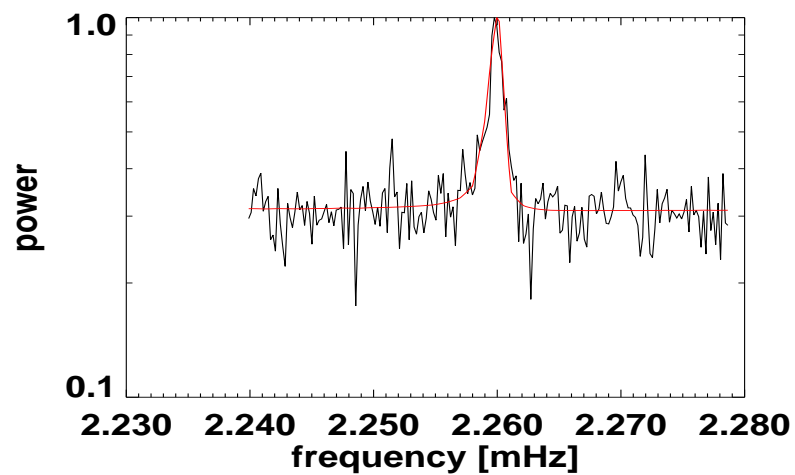


**Figure II.30:**  $l = 22, n = 9$  mode, observed in line depth (black line), and a calculated *real line depth* spectrum for a source depth of +100 km fitted to the observations according to equation (II.29) (red line). The peaks are normalized to their maxima.

important for fits. Hence, observed asymmetry differences must be attributed to the correlated noise.

To infer the fraction of correlated noise in line depth spectra, simultaneous power and cross spectrum fitting for line depth and velocity would be desirable. Unfortunately, the mutual phases of the calculated spectra are too noisy to do so. We therefore fitted only the observed line depth power spectrum of the  $l = 22$ ,  $n = 9$  mode to a model given by

$$P_{ld}^l = |L_l + c_{ld}^{corr}|^2 + |c_{ld}^{nc}|^2, \quad (\text{II.29})$$

where  $L_l$  represents the *real line depth* Fourier spectrum,  $c_{ld}^{corr}$  is the correlated noise, and  $|c_{ld}^{nc}|^2$  represents the uncorrelated background. The fraction of correlated noise, which is necessary to fit the model to the observations, is between zero and ten percent. This is a very rough estimate, but the fact that the MDI line depth is a differential signal, suggests that the fraction of correlated noise is similarly low in line depth and in velocity spectra.

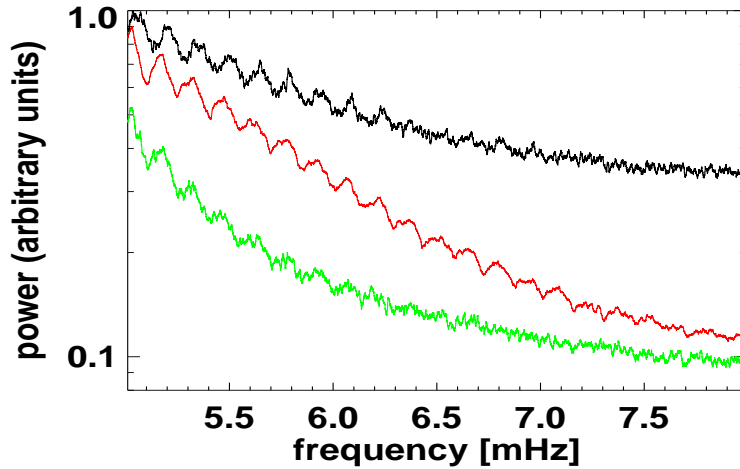


**Figure II.31:** Observed pseudo mode spectra for  $l = 22$  for intensity (black line), line depth (red line), and velocity (green line). The  $m$ -averaged spectra are smoothed with a running mean of  $10 \mu\text{Hz}$  width. The vertical scale is arbitrary here.

Figure II.31 shows the observed power spectra for velocity, intensity, and line depth. In line depth spectra, pseudo-modes are visible up to frequencies as high as  $7 \text{ mHz}$ . Pseudo-modes are less visible in intensity spectra, and least pronounced in velocity. Because of the smooth power variation in the pseudo-mode frequency band, the mode visibility is determined by the ratio of the power contrast of minima and maxima, and the variance of the residuum. As the variance of the residua is similar in the

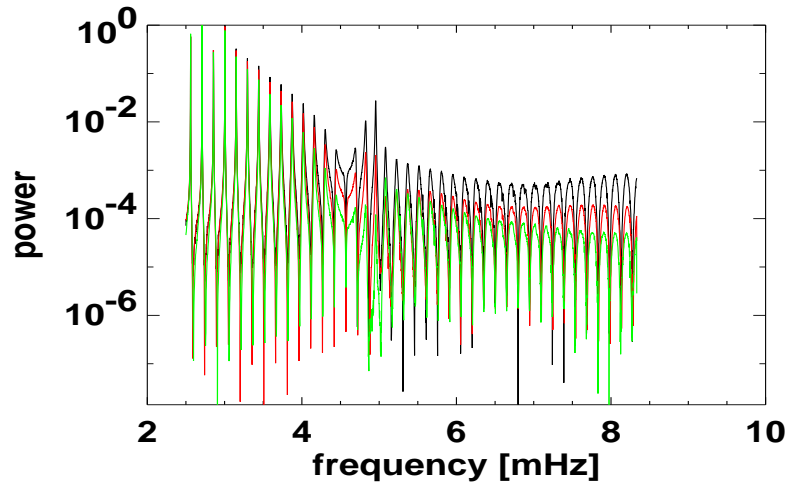


**Figure II.32:** *Real line depth* (black line), *MDI intensity* (red line) and *velocity* (green line) power spectra for  $l = 22$ , normalized to their maxima, with a frequency independent point source at +100 km. The *real intensity* spectrum, which is not displayed here, is very close to the *MDI intensity* spectrum.

spectra, there seems to be an enhanced power contrast in the line depth pseudo-modes due to higher pseudo-mode amplitudes. Nigam (1999) has shown, that correlated noise can substantially enhance the power in the pseudo-mode range. Substantial correlated noise, however, is not expected for the line depth signal. The high visibility of pseudo-modes in line depth spectra is therefore puzzling.

Our radiative transfer calculations are able to give a qualitative explanation. Figure II.32 shows the power spectra for velocity, *MDI intensity*, and *real line depth*, normalized to their maximum. The high pseudo-mode power in the line depth spectra can probably be attributed to the slower decay of mode power with frequency, compared to intensity and velocity spectra. The lowest pseudo-mode signal is observed in the velocity spectra — consistent with the rapid power decay in velocity. Therefore, an unexpectedly high correlated noise component in the differential line depth signal is maybe not necessary to explain the observations. Radiative transport effects probably play a crucial role for the explanation of the high pseudo-mode power in line depth spectra. A quantitative evaluation of this remains a challenging task, because of the difficulty to model the high frequency spectra reliably.

## II.7 Conclusions

With our approach to fit medium- $l$  power and cross spectra with physically reliable models of the resonance, we could derive an upper limit for the correlated fraction of



the total additive noise in the Doppler velocity signal of 1% in the case of a dipole source, and 2% in the case of a quadrupole source. The corresponding intensity signal has been found to be between 5% and 20%, depending on depth and multipole order of the source. The lower fraction of correlated noise in velocity confirms the assumption of a predominantly intensity-like signal correlated with the source. This is consistent with the assumption of p-mode excitation by dark downdrafts in intergranular lanes.

The deviation of the phase from the adiabatic value (Jimenez et al., 1999) can be attributed to nonadiabatic effects, as soon as the radiation flux is included in the oscillation equations. The background plays a minor role in the examined frequency range. The phase of the intensity contribution, which is constrained by the observed asymmetry reversal, is close to phase opposition with respect to the phase of the Green's function representing the solar oscillation mode. This is a specification of the negative asymmetry parameter found by Nigam & Kosovichev (1998), and can be interpreted as a negative intensity contribution of dark intergranular lanes, being correlated to the (positive) inward flow. This is the current idea about excitation of p-modes as obtained from numerical simulations (Stein & Nordlund, 2001). A phase offset of about  $20^\circ$  with the lower intensity being ahead of the excitation signal can be interpreted as time lag of the response (see figure II.15). We can not confirm the important role of a correlated velocity component to explain the phase spectra that Skartlien & Rast (2000) found for high- $l$  modes. Of course, downflows are associated with a velocity signal, but because velocity is observed at a higher atmospheric level than continuum intensity, the velocity signal from seismic events at the base of the photosphere is maybe not visible in the mid-photosphere, where the line is formed.

All results for the noise parameters (and the inequality for the source depth) are consistent with the p-mode excitation by rapid intergranular downdrafts, which possibly correspond to the observed seismic events. Both dipole and quadrupole excitation is possible, with only minor modifications for the mode parameters. The situation for the low- $l$  spectra remains unclear, because the profiles of the Green's function peaks do not agree with observations. Obviously, the physically better motivated mode profile from the nonadiabatic Green's functions is less flexible than a more empirical model like the modified Lorentzian profile, so that it can not absorb additional modifications of the mode profile caused by e.g. solar cycle effects.

In figures II.4 and II.6 we demonstrated that modes of oscillations in luminosity and velocity do not necessarily show the same profiles, both for p-modes and pseudo-modes, provided that the source is located not very deep in the convection zone. This shift, however, can not explain the observed shift in intensity and velocity pseudo-mode power spectra.

Radiative transfer calculations show that the phase of the MDI-intensity, given by

equation I.31, may differ from the continuum intensity in the neighborhood of the absorption line. Therefore, the estimates for the correlated noise displayed in table II.1 may be biased towards a lower fraction of correlated noise. A quantitative evaluation of this needs to be done in the future. Figure II.29 gives a clue, why pseudo-mode visibility is highest in line depth spectra. We suggest, that this is not, as suggested by Nigam (1999), caused by a high fraction of correlated noise, but a subtle effect of the line formation by radiative transfer in the solar atmosphere.

Georgobiani, Stein & Nordlund (2003) showed that radiative transfer is able to modify the asymmetry of high- $l$  continuum intensity mode-peaks, provided that the modes have high amplitude. The mode modifications we found for medium- $l$  with a different approach are much smaller. In particular, the modes' asymmetries are not changed. Nevertheless, estimates for the noise parameters can be slightly changed if radiative transfer is properly treated in the upper solar convection zone and in the photosphere. Investigating how p-mode profiles and phases are influenced by radiative transfer effects will be a crucial premise to make further progress in the investigation of mode-noise interaction in helioseismic spectra.



## Chapter III

# Search for G-Modes in the Supergranular Noise

G-modes are confined to the radiation zone (see figure I.3), and their surface amplitudes are too low to be easily detected in the currently available time series of Doppler velocity and intensity. If g-modes are excited by turbulent stresses in the convection zone, their amplitudes are below 0.4 mm/s (Kumar et al., 1996; Andersen, 1996). This means, that even for the longest available time series, they are hidden in the supergranular noise. G-modes are expected to have a very long lifetime, due to strong trapping and low internal damping. This results in very narrow peaks, i.e. peaks of width below the frequency resolution of the available spectra. Therefore, the signal-to-noise ratio should improve with the square root of the observation time, due to supergranular noise averaging out with time. Thus, usually very long time series of whole disk measurements (“Sun as a Star”) are accumulated, and the resulting spectra are searched for peaks corresponding to theoretically predicted resonance frequencies. Because no solar g-mode could be identified unambiguously up to now, upper limits for their amplitudes have been given (e.g., Appourchaux et al., 2000). Our approach is complementary to time series analysis and exploits the possibilities of spatially resolved data from the MDI instrument.

We will examine the interplay of g-modes and supergranular noise with regard to observational aspects. Gravity modes of the Sun are expected to provide valuable information about the internal properties of the Sun. Knowledge of the g-mode frequencies would be especially important for inferring the properties of the solar core, because compared to p-modes, g-modes are much more sensitive to the Sun’s deep interior. Thus, our focus will be on maximizing the signal-to-noise ratio of possibly present modes, taking advantage of the spatial properties of velocity eigenmodes, which are well constrained by theory, and the properties of the supergranular noise,

which are accessible to observations. Although the method presented below will not be able to detect g-modes, it will enable us to give very accurate upper limits for the surface amplitude of each mode, which constrains assumptions about the g-mode excitation process.

The work presented below was published in Wachter et al. (2003).

### III.1 Data

Only low- $l$  g-modes are expected to have appreciable amplitudes at the surface (Christensen-Dalsgaard, 1998). Nevertheless, our approach for g-mode detection requires spatially resolved data to apply optimized masks. Therefore, we used two data sets of almost continuous Doppler measurements from the *medium-l* program of MDI (Kosovichev et al., 1997). Both data sets, which are separated by the 1998 SOHO observation gap, cover 765 days, one from 1996 May 5 through 1998 June 8, and the other from 1999 March 1 through 2001 April 3, with a sampling rate of one minute. The duty cycles are 95.8% and 96.3%, respectively. We decided not to use just one time series including the gap in SOHO observations in 1998 to avoid a modification of the noise statistics by the large gap, and to account for possible solar cycle changes of both modes and noise.

The data are remapped onto the solar surface using heliographic coordinates. A model is fitted to the data in order to remove the Doppler shift produced by solar rotation. Further corrections to account for the spacecraft's motion are applied. To contain the computational effort, the grid's resolution was reduced, using Gaussian smoothing. The resulting data, which we used as a starting point for the optimal masks, are time series of images with  $41 \times 38$  pixels, covering the range between  $\pm 60^\circ$  in longitude and  $\pm 0.95$  in sine latitude with a cosine bell-shaped apodization between 83% and 87% of the Sun's radius.

### III.2 Horizontal and Radial Components in Noise and Modes

To maximize the signal-to-noise ratio of each low frequency mode that might be present, we exploit the spatial resolution of the MDI instrument. In contrast to the p-mode range, noise in the frequency range where g-mode detection could be anticipated (below  $\approx 470\mu\text{Hz}$ ) is mostly horizontal, resulting in a low noise level at the disk center (see figure III.2), where movement is mainly perpendicular to the line-of-sight. On the other hand, within the frequency band where detection of g-modes is expected,

for low angular degrees  $l$  a transition occurs from essentially radial to mostly horizontal eigenmodes: higher frequency g-modes are, like the visible p-modes, mostly radial whereas lower frequency g-modes become mainly horizontal. It follows directly from equations (I.20) and (I.21), that the ratio of the radial and horizontal root mean square (rms) displacement (i.e., the displacement averaged over one period and the solar surface) for a mode of angular degree  $l$  and frequency  $\omega$  is given by:

$$\sqrt{l(l+1)} \frac{g(R)}{R\omega^2} \equiv b(\omega). \quad (\text{III.1})$$

Equation (I.21) has been derived applying the Cowling approximation, which is not necessarily valid for modes of low angular degree and radial order. In order to show that equation (I.21) can be applied for these modes, too, we compared the ratio of horizontal and radial component of numerically calculated low- $l$  eigenfunctions with the value obtained by equation (I.21), and found that the difference is smaller than 2%, both if the Cowling approximation is applied or not.

We note that  $b(\omega) = 1$  is the characteristic of the surface gravity (f) mode ridge for  $l \gtrsim 20$  (Christensen-Dalsgaard, 1998). For low  $l$ , however, we get well into the region of avoided crossings, where the f-mode frequency is no longer given by  $b(\omega) = 1$ . Instead, the graph defined by  $b(\omega) = 1$  in the  $l - \omega$  diagram is within the area of the g-mode ridges. In particular, for the low degree modes we examined, a transition occurs from mostly horizontal to mostly radial displacement within the frequency range of interest. In figure III.1 the line-of-sight projected mode pattern of a  $l = 2$ ,  $m = 0$  mode is displayed as a function of frequency. Between  $110\mu\text{Hz}$  and  $156\mu\text{Hz}$ , the mode's displacement changes from predominantly horizontal (lower frequencies) to predominantly vertical (higher frequencies). Note that the change occurs simultaneously in the mode's pattern (as the eigenfunction changes from spherical harmonics to its derivatives), and in the different projection properties of radial and horizontal components (as the mode changes from radial to horizontal movement).

### III.3 Estimation of the Noise Level

From single pixel time series on the  $41 \times 38$  grid, the local noise level across the solar disk can be estimated. The variance of such a time series is inversely proportional to the area it is taken from. Because the grid is defined such that each pixel covers the same portion of the solar disk, a well defined local noise level at a given frequency is the spectral variance times the solid angle of the area covered by the pixel. The resulting noise distribution is shown in figure III.2.

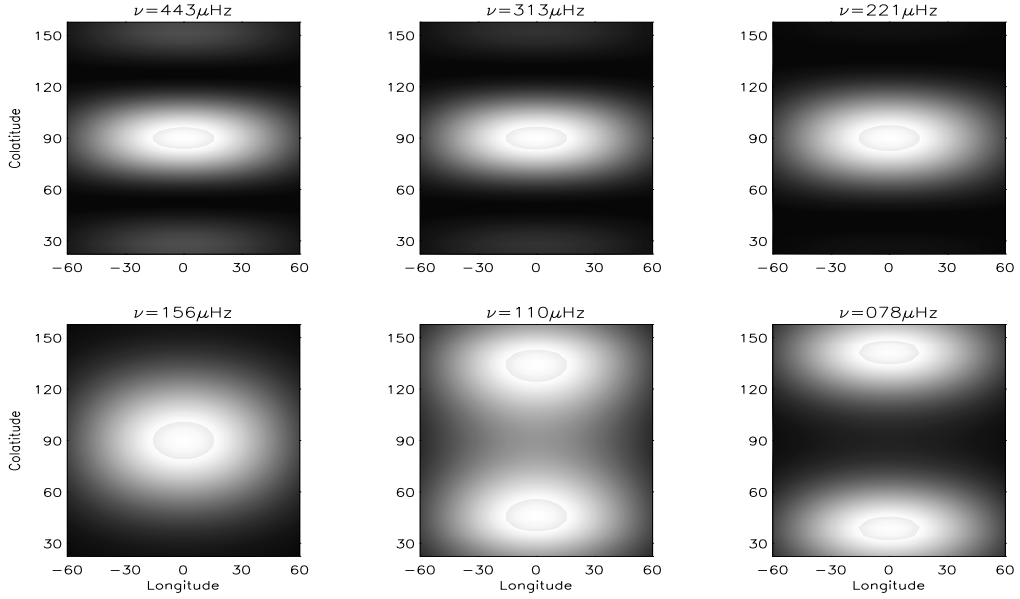


**Figure III.1:** Map of the mode pattern of a  $l = 2, m = 0$  mode as a function of frequency. White correspond to maximum oscillation amplitudes, black correspond to nodes of the mode.

The variation of the noise across the solar disk can be modelled with a straightforward assumption. We assume that noise is equally distributed over the surface of the Sun, having radial as well as horizontal components. The projection properties of the horizontal and radial noise components cause the level of noise to vary across the solar disk.

Supergranulation is the most likely cause of noise in the frequency range of our interest. It consists mostly of horizontal flow, together with a smaller component of radial flow. In our model, the projected noise process is given by:

$$\epsilon = \begin{pmatrix} \sigma_r \\ \sigma_\Theta \\ \sigma_\Phi \end{pmatrix} \cdot \mathbf{e}_x, \quad (\text{III.2})$$

where  $\mathbf{e}_x$  is the unit vector in the line-of-sight direction. Its variance  $\sigma^2 = E|\epsilon|^2$  is given by:

$$\sigma^2(\Theta, \Phi, \omega) = \sigma_r^2(\omega) \sin^2 \Theta \cos^2 \Phi + \sigma_\Theta^2(\omega) \cos^2 \Theta \cos^2 \Phi + \sigma_\Phi^2(\omega) \sin^2 \Phi, \quad (\text{III.3})$$

where  $\sigma_r^2$ ,  $\sigma_\Theta^2$  and  $\sigma_\Phi^2$  is the variance of the radial, latitudinal and longitudinal displacement, respectively.

Equation (III.3) implies that the different vector components of the noise are uncorrelated. This assumption was made for simplicity and because the correlation coef-

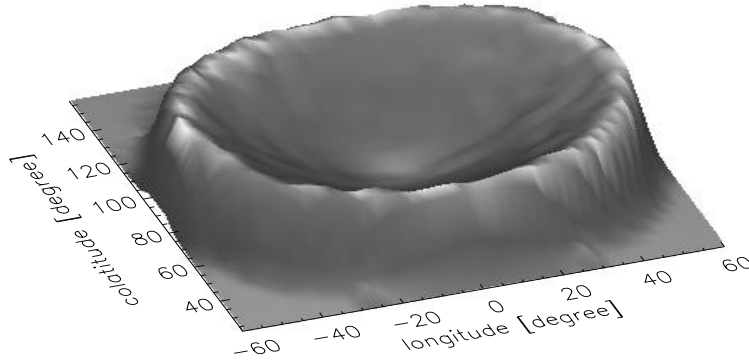


**Figure III.2:** Map of the estimator for the local noise level at  $78 \mu\text{Hz}$ . The estimator has been obtained from one year time series of single pixels before the 1998 SOHO gap. In the center, the crater-like structure reflects the variation of the local supergranular noise. The decay at the boundaries is due to apodization by the instrument and the data processing. For the vertical scale, see figures III.3.

ficients turned out to be hard to estimate. Because no obvious modes are present, the noise level can be derived directly from the power spectrum. As illustrated in figure III.3, expression (III.3) models the functional dependence of the noise on the surface coordinates  $\Theta$  and  $\Phi$  quite well. The small systematic error in the fit is probably a consequence of the smoothing effect caused by averaging the whole range of solar B angles (see next section for an explanation) with a varying filling factor of the time series, or may be caused by noise sources other than solar supergranulation.

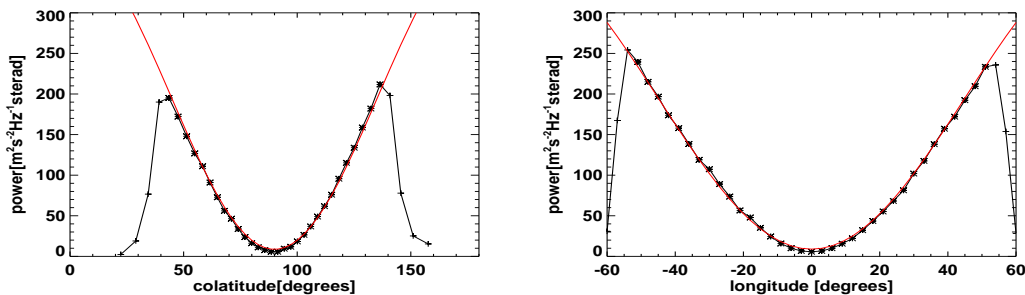


**Figure III.3:** Estimator for the noise at  $78 \mu\text{Hz}$  (asterisks) as displayed in figure III.2. The left panel shows the noise level at the central meridian as a function of colatitude and the fitted curve (red line) according to the model given by equation (III.3). The right panel shows the noise level for a horizontal cut close to the solar equator (colatitude:  $91.4^\circ$ ). The values close to the limb (plus signs), which are influenced by the data apodization, were not used in the fit.

The fitted coefficients (see figure III.4) show that the horizontal noise is indeed



two orders of magnitude higher in power than the radial noise. The level after the 1998 SOHO observation gap is a few percent higher than before, for both radial and horizontal noise. This is an interesting observation, regarding the fact that for intensity measurements there is an obviously enhanced noise level during solar maximum below about  $400 \mu\text{Hz}$  (see figure I.4). Nevertheless, it is unclear whether increased solar activity or instrumental changes during the gap are responsible for this increase in noise. However, as long as the model given by equation (III.4) can be fitted well, as is true for all frequencies of interest, the exact origin of the noise is unimportant for the masks.

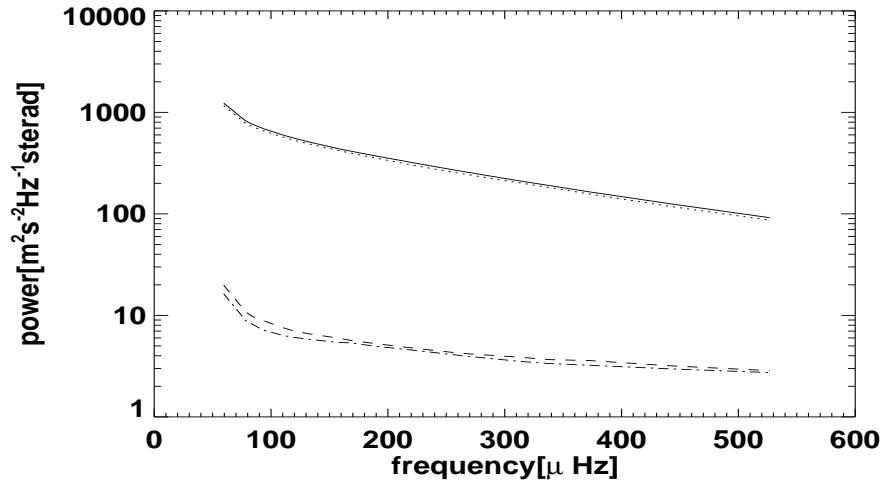


**Figure III.4:** Horizontal noise levels  $\sigma_{\Theta}^2 + \sigma_{\Phi}^2$  (upper lines) and radial noise levels  $\sigma_r^2$  (lower lines) as a function of frequency (see equation (III.3)). The noise after the 1998 SOHO gap (solid line and dashed line) is a little bit higher than before the gap (dotted line and dashed-dotted line).

### III.4 Optimal Masks

The velocity image obtained by the MDI instrument corresponds to the time derivative of the displacement vector projected onto the line-of-sight. Therefore, the spatial pattern we expect to see from a mode of frequency  $\omega$ , angular degree  $l$ , and tesseral order  $m$  in the instrument's image is the real part of:

$$\tilde{Y}_l^m = \delta \mathbf{r}(t = 0) \cdot \mathbf{e}_x, \quad (\text{III.4})$$

and the line-of-sight velocity is given by:

$$v = \Re(i\omega \delta \mathbf{r} \cdot \mathbf{e}_x), \quad (\text{III.5})$$

where  $\delta \mathbf{r}$  is given by equation (I.20). It is important to note that the projection of a displacement at a given point on the solar surface is not constant, but varies during the year due to the inclination of the Sun's axis of rotation with respect to the ecliptic. This is usually described by the so called solar B angle, being the heliographic latitude of the disc center seen from the ecliptic, which undergoes an oscillation with a yearly period. Therefore,  $\mathbf{e}_x$  is a slowly varying, a priori known function of time.

In addition to the mode pattern, there is a noise component to the image. The *medium-l* data we used already contain an apodization  $a(\Theta, \Phi)$ , so if we calculate a time series

$$y(t) = \int M(\Theta, \Phi) (v(\Theta, \Phi, t) + \epsilon(\Theta, \Phi, t)) a(\Theta, \Phi) d\Omega \quad (\text{III.6})$$

made from an image consisting of a mode signal  $v$  and a noise term  $\epsilon$ , the ‘‘optimal mask’’  $M(\Theta, \Phi)$  in terms of the best signal-to-noise ratio is:

$$M(\Theta, \Phi, \omega) = \frac{(\tilde{Y}_l^m a)^* / \sigma^2}{\int |\tilde{Y}_l^m a|^2 / \sigma^2 d\Omega}. \quad (\text{III.7})$$

(see Appendix D).

In the limit of a spatially uniform noise level, and neglecting the horizontal component of the eigenfunctions, projection factor, and apodization, the masks given by equation (III.7) reduce to the usual spherical harmonic masks.

Following equations (III.7) and (III.4), we build the mask using the displacement vector given by equation (I.20) with a normalization factor for the radial component of displacement:

$$\xi_r^0 = \left( 2 + \frac{2l(l+1)g^2(R)}{R^2\omega^4} \right)^{-1/2}, \quad (\text{III.8})$$

and the corresponding horizontal amplitude given by equation (I.21).

Using this normalization in expression (III.7) guarantees that the height of the peak in the amplitude spectrum, which is defined by:

$$A(\omega) = \frac{1}{n} \left| \sum_{j=0}^{n-1} y(t_j) e^{-i\omega t_j} \right|, \quad (\text{III.9})$$

corresponds to the mode's rms velocity (see Appendix E). This normalization has been chosen so that in case of failed mode detection, the upper limit for the surface amplitudes can be derived directly from the amplitude spectrum.

### III.5 Masks for $l = 1$ , $l = 2$ , and $l = 3$

According to Christensen-Dalsgaard (1998), low- $l$  g-modes have the highest amplitudes at the solar surface. Therefore, we decided to calculate optimal masks for all tesseral orders of angular degrees  $l = 1$ ,  $l = 2$ , and  $l = 3$ . Because both the eigenfunctions and the noise are frequency dependent, the masks also depend on mode frequency. In order to obtain spectra from the spatially resolved time series, we have to evaluate the integral:

$$y(\omega) = \int dt e^{-i\omega t} \int_D d\Omega M(\Theta, \Phi, \omega, t) y(\Theta, \Phi, t). \quad (\text{III.10})$$

In the case of a time independent mask, we can change the order of integration:

$$y(\omega) = \int_D d\Omega M(\Theta, \Phi, \omega) \int dt e^{-i\omega t} y(\Theta, \Phi, t) \quad (\text{III.11})$$

This expression can be easily evaluated for each frequency  $\omega$  by calculating spectra from single pixel time series using the Fast Fourier Transform method (Press et al., 1986) before applying the masks. Due to the fact that we consider time dependent masks which take the slowly varying projection properties of the modes into account, masks for each frequency get computationally expensive. To avoid this, we used a single mask for the entire band when neither the pattern of the eigenmode nor the noise level changed substantially within a particular frequency band.

The eigenfunction is much more sensitive to changes in frequency than the noise level is. To account for this sensitivity, we used optimal masks for frequencies with the ratio of horizontal and radial amplitude of the displacement eigenfunction given by

$$b(\omega) = 2^\alpha \quad (\text{III.12})$$

(see equation (III.1)). For  $\alpha$  we chose the values -3, -2, -1, 0, 1, and 2 (for  $l = 1$  we included  $\alpha = -4$ ) to cover roughly the frequency range from 50  $\mu\text{Hz}$  to 500  $\mu\text{Hz}$ . Below 50  $\mu\text{Hz}$  the noise level may be too high for any g-mode to be seen, whereas the peak of the buoyancy frequency sets the upper limit of this frequency band.

For a given  $l$ , the values of  $\alpha$  correspond to particular frequencies (see equations (I.21) and (III.12)). Although these frequencies are *not* theoretically predicted g-mode frequencies, the corresponding masks are almost optimal for possibly present g-modes in the vicinity of these frequencies. More precisely, the loss of amplitude for these ‘‘almost optimal’’ masks does not exceed 10% at the edges of the frequency band.

## III.6 Detection Limits

A Gaussian distribution of the noise results in a  $\chi^2$  statistics with two degrees of freedom of the corresponding power spectrum. The probability  $P$  that none out of  $N$  realizations exceeds a value of  $s$  times the variance of the noise is given by:

$$P = (1 - e^{-s})^N. \quad (\text{III.13})$$

We set the detection limit so that there is a 90% probability  $P$  that no noise peak exceeds this limit within a frequency band of  $70 \mu\text{Hz}$ . These values were chosen to compare our results with the upper limit given by Appourchaux et al. (2000). For our time series of 765 days, a band of  $70 \mu\text{Hz}$  corresponds to  $N = 4627$  frequency bins. Because the noise can be regarded as locally white within this frequency range, the distribution of the adjacent bins is approximately equal to the distribution of independent realizations of a Gaussian process.

To increase the frequency resolution, we padded the time series to five times its original length. Because g-modes are not expected to have an intrinsic width, padding prevents a loss of amplitude for noncommensurate mode frequencies. However, doing this, the bins are no longer independent. For  $P$  fixed, we performed Monte Carlo simulations. A set of Gaussian white noise processes was generated in the time domain, and the zero-padded time series were Fourier transformed. From the spectra, we identified the maxima in frequency bands of  $70 \mu\text{Hz}$ , and set the limit such that 90 % of the maxima were below the limit. For our time series of 765 days,  $s$  increases from 10.7 to 11.7. This independently-calculated value confirms the more general expression given by Gabriel et al. (2002). The power spectrum is divided by the filling factor to compensate for the amplitude loss caused by gaps. The gaps due to bad minutes of the time series (4.2% and 3.7%, respectively, see Section III.1) turn out to have no appreciable influence on the noise distribution. Estimating the variance as a local mean value over  $2d + 1$  frequency bins of the power spectrum, the upper limit  $L(\omega_k)$  at frequency  $\omega_k$  is given by:

$$L(\omega_k) = \sqrt{\frac{s}{f} \frac{1}{2d + 1} \sum_{j=-d}^d A^2(\omega_{k+j})}. \quad (\text{III.14})$$

## III.7 Results

For each  $l$  and  $m$ , we examined the adjacent frequency bands for peaks using the spectra for the six values of  $\alpha$ , as shown in figure III.5 for the  $l = 2, m = 2$  mode.

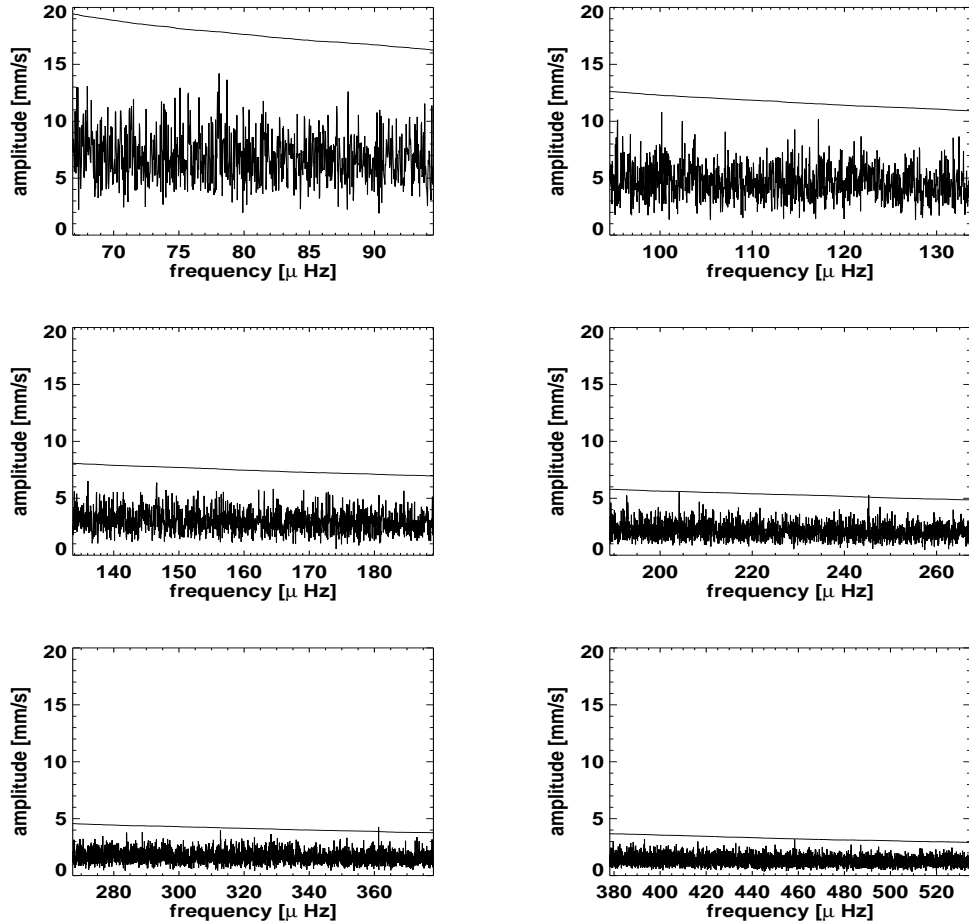


**Figure III.5:** Spectra for the 6 consecutive optimal masks for a  $l = 2$ ,  $m = 2$  mode, from a two year time series after the 1998 SOHO gap. The masks are optimal for the frequencies  $78 \mu\text{Hz}$ ,  $110 \mu\text{Hz}$ ,  $156 \mu\text{Hz}$ ,  $221 \mu\text{Hz}$ ,  $313 \mu\text{Hz}$ , and  $443 \mu\text{Hz}$ . The detection limit was determined as a running mean according to equation (III.14). We see peaks exceeding the detection limit at  $245.2 \mu\text{Hz}$  and  $361.2 \mu\text{Hz}$ .

Most of the peaks that exceed the detection limit are of instrumental origin. They are harmonics of  $52.125 \mu\text{Hz}$ , a period which arises from beats between the spacecraft's timing system and the instrument's sampling rate (Appourchaux et al., 2000).

Some peaks, which exceed the detection limit, cannot be identified as instrumental artifacts. They occurred at  $57.9$ ,  $92.6$ ,  $160.8$ ,  $173.6$ ,  $328.1$ ,  $339.6$ ,  $343.6$ , and  $445.0 \mu\text{Hz}$  (8 peaks) in the period before the SOHO gap, and at  $118.7$ ,  $204.1$ ,  $245.2$ ,  $361.2$ ,  $443.5$ ,  $466.2 \mu\text{Hz}$  (6 peaks) in the period after the SOHO gap. We note that because the spectra are far from being independent, most of these peaks occur in several spectra simultaneously. We checked these peaks for correspondence with the frequencies given by the solar standard model M1 of Provost, Berthomieu, & Morel (2000), and found no agreement. However, classifying peaks as modes, whenever their frequencies

are close to mode frequencies predicted by a solar standard model is problematic, because the various solar models predict frequency deviations of up to  $10 \mu\text{Hz}$  (Provost, Berthomieu, & Morel, 2000). None of these non instrumental peaks occur in both spectra before and after the 1998 SOHO gap. Because of the very long lifetime of the low frequency modes ( $\approx 10^6$  years Kumar et al. (1996)), this is a strong indication that the peaks are manifestations of the realization noise rather than caused by a coherent mode of oscillation. Therefore, they are most likely statistical outliers of the realization noise. The expected number of outliers for a single spectrum can be simply determined from the probability  $P$  of equation (III.13) and the number of independent frequency bins in this spectrum. The total number of outliers in all spectra is hard to estimate, because the spectra for the different  $l$  and  $m$  are far from being independent. A rule of thumb estimation for number of outliers is the number of  $70 \mu\text{Hz}$  bands within the investigated frequency range of  $450 \mu\text{Hz}$ , times the number of searched spectra, times the outlier-probability 0.1. This leads to an expected number of 9.6 outliers. Because the spectra are not independent, this number can be regarded as an upper limit. The number of 6 and 8 outliers, respectively, is consistent with this estimation.

The detection limits become observational upper limits for the surface amplitude of the modes in case of failed mode detection, because higher mode amplitudes would result in amplitude spectrum peaks above the detection limit.

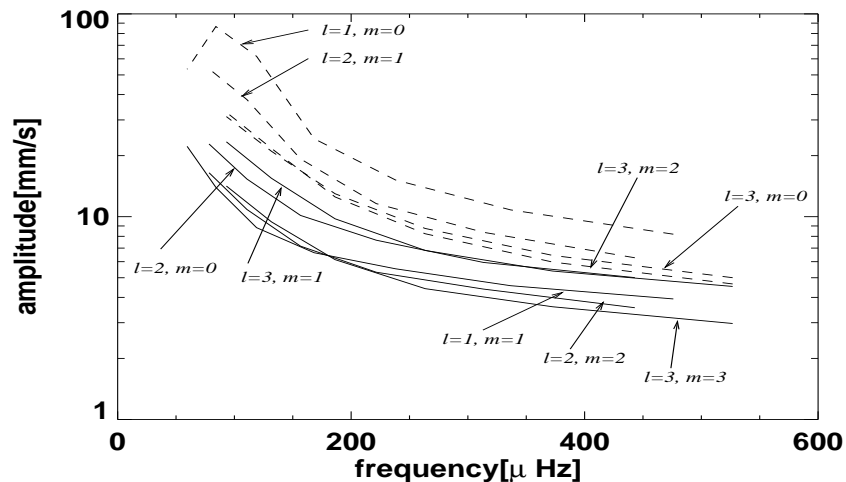


**Figure III.6:** Upper limits of the rms surface amplitudes for all modes of angular degree 1, 2, and 3 in the g-mode range as a function of frequency. The upper limit is determined for the selected frequencies, and the points are connected by straight lines. The solid lines correspond to the  $l + m$  even modes, the dashed lines to the  $l + m$  odd modes.

As we can see in figure III.6, the detection limit for the even modes is lower than for the odd modes. The reason for this is that the radial components of the even modes

have significant amplitude in the center of the disk, where the noise level is low.

The  $l = 1, m = 0$  mode is somehow a singular case. When the amplitudes of the horizontal and radial components are equal, which is the case at about  $100 \mu\text{Hz}$ , the mode turns out to be a spatially-uniform displacement of the Sun's surface against its core — parallel to the rotation axis. This mode is hardly visible because the displacement is almost perpendicular to the line-of-sight.

To compare with Appourchaux et al. (2000), the detection limits for each single mode at  $200 \mu\text{Hz}$  are denoted explicitly in table III.1.

m	$l = 1$	$l=2$	$l=3$
0	18.3	8.1	11.7
1	6.1	13.1	9.0
2		5.7	11.3
3			5.6

**Table III.1:** Upper limit in mm/s for the rms surface amplitudes of g-modes of angular degrees 1, 2 and 3 at  $200 \mu\text{Hz}$ .

### III.8 Discussion and Conclusions

G-modes have a very low amplitude in the convection zone and in the photosphere. This makes their detection in Doppler velocity data and continuum intensity data difficult. Their excitation is expected to occur at the upper boundary of their resonance cavity, i.e. at the base of the convection zone. Other than in the p-mode range, the surface noise has no direct connection to the excitation process of the g-modes. However, there is a strong interplay of g-modes and surface noise in terms of mode detectability.

The line-of-sight projection of both modes and additive background, and the restricted available image of the solar surface is the cause of different detectability of the modes. This is the reason for the substantial variation of the upper limits shown by table III.1. Each  $l, m$  mode requires its appropriate mask because it is not known a priori which one of the long-lived and probably rarely excited modes has a detectable amplitude. Whole disk measurements are sensitive only to the modes of even  $l + m$  values, and the implicit “mask” corresponding to disk-averaged data can be far from optimal.

At 200  $\mu\text{Hz}$ , Appourchaux et al. (2000) gives an upper limit of 10 mm/s in rms velocity derived from whole disk MDI time series. For cross-calibration, we used the same mask for our images, and got similar results. The average multiplet rms velocity at 200  $\mu\text{Hz}$  is 10.2 mm/s for  $l=1$ , and 9.1 mm/s for  $l=2$  and  $l=3$ . This shows, that the whole disk value is a good estimation of the mean observational upper limit for g-modes. However, adjusting the mask to the mode's eigenfunction leads to significant deviations from this general estimate. The optimization of the masks, in terms of the spatially varying noise level, improves the signal-to-noise ratio by up to about 25%. Altogether, the limits given in table III.1 are not generally lower, but more carefully derived than those reported by Appourchaux et al. (2000) and Gabriel et al. (2002). The lowest limits in the range of 5-6 mm/s are obtained for sectorial modes of  $l = 1, 2$ , and 3.

Even lower limits can be obtained using time series analysis techniques; e.g. Appourchaux et al. (2000) gives an upper limit of 7 mm/s in rms velocity at 200  $\mu\text{Hz}$  for the so called "collapsogram" technique. In this technique, spectra for different  $m$  are averaged to dilute the noise peaks. The upper limit derived from these spectra only provides an estimate for the maximal average multiplet amplitude, whereas we are able to determine observational upper limits for each single mode. Of course any kind of time series analysis can be applied to the time series obtained by the optimal masks, too, but this is beyond the scope of this work.

Although we were not able to discover g-modes, we have shown that by using the method of optimal masks the chances for revealing the weak signal of these modes can be significantly improved. Even for low degree modes, spatially resolved data are useful to reveal a weak mode signal.

For future work, the analysis could be expanded to higher  $l$ . According to Christensen-Dalsgaard (1998), there is a chance to detect g-modes for  $l \lesssim 20$ . The method presented could be applied to low frequency p-modes, too, but it has to be noted that for higher frequencies the variation of the noise level across the solar disk is less pronounced, so that the improvement obtained in the signal-to-noise is probably modest. Because of the poor leakage properties of the optimal masks, they should only be applied if the modes are well separated in frequency.





# Appendix A

## Basic Equations of Nonadiabatic Oscillations

The following five differential equations in the radial amplitudes describe a nonrotating, nonmagnetic star:

$$\frac{d}{dr} \left( \frac{\tilde{p}'}{\rho} + \tilde{\Phi}' \right) - \frac{N^2 \tilde{p}'}{g\rho} + (N^2 - \omega^2) \tilde{\xi}_r = g v_T \frac{\delta \tilde{S}}{c_p} \quad (\text{A.1})$$

$$\frac{1}{r^2} \frac{d}{dr} (r^2 \tilde{\xi}_r) + \frac{d \ln p}{dr} \frac{\tilde{\xi}_r}{\Gamma_1} + \left( 1 - \frac{S_l^2}{\omega^2} \right) \frac{\tilde{p}'}{\rho c^2} - \frac{S_l^2}{c^2 \omega^2} \tilde{\Phi}' = v_T \frac{\delta \tilde{S}}{c_p} \quad (\text{A.2})$$

$$\frac{1}{r^2} \frac{d}{dr} \left( r^2 \frac{d \tilde{\Phi}'}{dr} \right) - \frac{S_l^2}{c^2} \tilde{\Phi}' - 4\pi G \rho \left( \frac{\tilde{p}'}{\rho c^2} + \frac{N^2}{g} \tilde{\xi}_r \right) = -4\pi G \rho v_T \frac{\delta \tilde{S}}{c_p} \quad (\text{A.3})$$

$$\delta \tilde{\epsilon}_N - \frac{d \tilde{L}_R}{d M_r} + \frac{l(l+1)}{d \ln T / d \ln r} \frac{F_R}{\rho r} \frac{\delta \tilde{T}}{T} + l(l+1) \left( \frac{\tilde{\xi}_h}{r} \frac{d L_R}{d M_r} - \frac{\tilde{\xi}_r}{r} \frac{L_R}{4\pi r^3 \rho} \right) = i \omega T \delta \tilde{S} \quad (\text{A.4})$$

$$\frac{\delta \tilde{L}_R}{L_R} = \frac{\delta \tilde{\kappa}}{\kappa} + 4 \frac{\tilde{\xi}_r}{r} - l(l+1) \frac{\tilde{\xi}_h}{r} + 4 \frac{\delta \tilde{T}}{T} + \frac{d \delta \tilde{T} / d \ln r}{d \ln T / d \ln r} \quad (\text{A.5})$$

Here,  $[v_T = \partial \ln(1/\rho) / \partial \ln T]_p$ ,  $\nabla_{ad} = [\partial \ln T / \partial \ln p]_S$ , and  $\tilde{\xi}_h$  is related to the frequency by  $\tilde{\xi}_h = (\tilde{p}' / \rho + \tilde{\Phi}') / \omega^2 / r$ .

From thermodynamic relations we obtain:

$$\delta \tilde{S} = c_p \left( \frac{\delta \tilde{T}}{T} - \nabla_{ad} \frac{\delta p}{p} \right) \quad (\text{A.6})$$

( $c_P = v_T p / (\nabla_{ad} \rho T)$ ), and

$$\frac{\delta \tilde{\kappa}}{\kappa} = \kappa_{ad} \frac{\delta \tilde{p}}{p} + \kappa_S \frac{\delta \tilde{S}}{c_P}, \quad (\text{A.7})$$

and

$$\frac{\delta \tilde{\epsilon}}{\epsilon} = \epsilon_{ad} \frac{\delta \tilde{p}}{p} + \epsilon_S \frac{\delta \tilde{S}}{c_P}, \quad (\text{A.8})$$

with the thermodynamic derivatives  $\kappa_{ad} = (\frac{\partial \ln \kappa}{\partial \ln p})_S$ ,  $\kappa_S = c_P (\frac{\partial \ln \kappa}{\partial S})_p$ ,  $\epsilon_{ad} = (\frac{\partial \ln \epsilon_N}{\partial \ln p})_S$ ,  $\epsilon_S = c_P (\frac{\partial \ln \epsilon_N}{\partial S})_p$ . They are given by a solar model.

These equations are first order in the perturbed variables, except for the perturbation of the gravitational potential, which is second order. Therefore, a formally simple set of six first order ordinary linear differential equations can be obtained by introducing a variable  $d\Phi/dr$ . Additionally, the two equations of state, and  $\kappa(T, \rho)$  and  $\epsilon_N(T, \rho)$  have to be known. The formulation of the problem in dimensionless variables is given in Chapter 24 of Unno et al. (1989).

The Cowling approximation is obtained by removing equation (A.3) from the set and setting  $\tilde{\Phi}'$  to zero. Then, the set is reduced to four first order equations.

The adiabatic approximation is obtained by removing equation (A.4) and (A.5) from the set, and setting  $\delta \tilde{S}$  to zero.

There is another frequently applied approximation, called the 'plane parallel approximation'. High degree modes do not penetrate very deep into the interior of the star. Therefore, these modes behave like oscillations in a plane parallel layer under constant gravity. Formally, this is obtained by neglecting radial derivatives of  $g$  and of derivatives of the explicit radial coordinate  $r$ .

# Appendix B

## Filling of Attractors in the SPM Data

For unknown reasons, the voltage to frequency converter of the instrument has preferred levels of counts. Therefore, there are data sequences with lengths ranging from several hours to several days which have an accumulation of erroneous data. This phenomenon has been named “attractor”. An example is given in figure B.1.

To obtain a clean time series with the best filling factor possible, our first task is to find the sequences where attractors occur. For that purpose, consecutive overlapping count histograms of two hour length with a separation of 5 minutes are calculated for the raw data (level zero). The bin size of the histograms is 3 counts. We consider a time series with the maximum of these histograms, where attractor periods are characterized by an enhanced value. Generally, periods with a level above 6 are declared as attractor periods. Whenever attractor periods are very close to each other, they are considered to be part of the same period. The “severeness number” of the attractors is calculated by integrating the histogram maximum time series over the attractor period. If the “severeness number” is below 400, the attractor is ignored. This criterion has been established according to the experience that sometimes a random cumulation of counts is mistaken as an attractor, and that very weak attractors have almost no influence on the spectrum.

Within these attractor periods, the real “bad minutes”, i.e. the invalid measurements, are identified by looking for the most frequently hit counts. The detrend of the level 1 data is performed by removing only these values. In the resulting stationary time series with a mean value of zero, the whole attractor period is set to zero. Setting only “bad minutes” to zero would result in a considerably increased high frequency noise.

Removing the attractors influences considerably the SPM spectra at periods of the typical length of an attractor, i.e. at periods below the p-mode range. More importantly, the estimates of amplitudes and width of the p-modes are biased towards lower

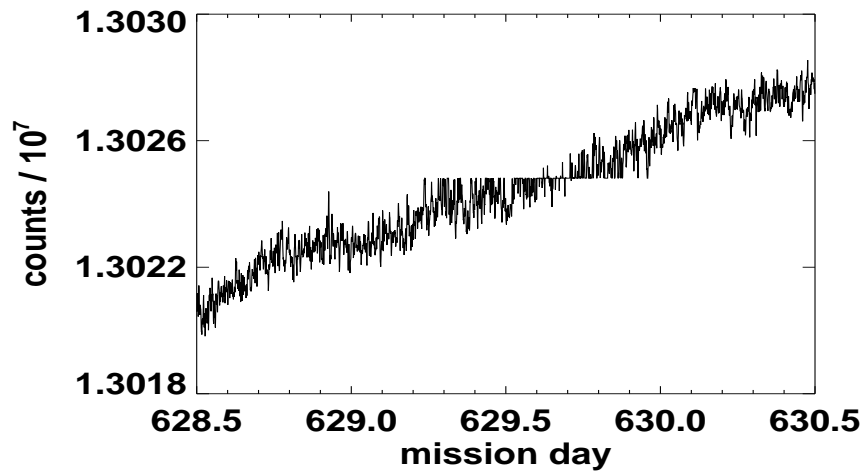


**Figure B.1:** Example for an attractor in the raw data (level 0) of the SPM red channel. The horizontal axis displays SOHO mission days (mission day one is Dec 2, 1995).

amplitudes and increased width. Moreover, the statistical distribution of the spectra is perturbed. To reduce this influence, we developed an algorithm to fill the gaps.

Because of an unexplained degradation behavior of the instrument, the SPM time series have to be detrended and normalized to the local mean value. The three channels differ mainly in variance, and their coherence is very high. Usually, attractors do not occur simultaneously in all three channels. All three SPM channels have a very high coherence and differ only by absolute value and local variance. The general idea is therefore to scale the detrended time series of one SPM channel to fill the other. The method described below has been tested with artificial attractors in clean data, and was found to give better results than alternative methods in the frequency domain. Several steps are involved in the filling procedure:

1. We used the green channel to fill the red one, the blue to fill the green one, and the green to fill the blue one. This choice was made according to highest mutual coherence.
2. The local standard deviation left and right of the attractor is compared to the global standard deviation. If there is a difference greater than 18% on both sides, the filling is cancelled.
3. The local standard deviation of the substitutional time series is calculated for the same period. A scaling factor is calculated from the ratio of the standard deviations of original and substitutional time series.

4. Validation and fine tuning of the scaling factor is performed by comparing the scaled time series from the substitutional channel to the valid points of the original time series within the attractor period. Values ranging from 0.5 to 1.5 times the factor estimated from the ratio of the standard deviations are tested. The factor which minimizes the squared difference is chosen. If the fine tuning fails, the filling will be cancelled. Linear tapering at the beginning and at the end of the filled period provides a smooth transition between original and filled sequences.
5. In this first step, the filling factor could be increased from 92% to 98% (red channel, the values for the other channels are similar). There are still gaps outside the attractor sequences due to other kind of occasional instrument malfunction and some remaining gaps in attractor periods whenever there are simultaneous gaps in the channels. Both other SPM time series are now used for substitution by scaling according to the ratio of the standard deviations left and right of the gap. This step raises the filling factor from 98% to 98.5%. The quality of the filling is lower in this second step, because here no valid points are available for validation. Although the improvement of the filling factor is modest, this second step is quite efficient in filling small gaps of only few minutes, which, if left unfilled, can be responsible for high frequency noise.



# Appendix C

## Leakage in the Pseudo-Mode Range

Equation (I.33) describes the dependence of the observed spectra on the modes on the Sun. Ignoring the multiplet's frequency splitting, the sum can be rewritten as:

$$y_l^m = \sum_{l'} x_{l'} \sum_{m'} C_{l,l'}^{m,m'} =: \sum_{l'} x_{l'} \beta_{l,l'}^m, \quad (\text{C.1})$$

where  $\beta_{l,l'}^m$  is defined by the sum over  $m'$ .

A  $m$ -averaged spectrum  $S_{av}$  is then given by:

$$S_{av} = \sum_m |y_l^m|^2 = \sum_{l'} \sum_{l''} x_{l'} x_{l''}^* \sum_m \beta_{l,l'}^m (\beta_{l,l''}^m)^*. \quad (\text{C.2})$$

The answer to the question how correlated noise enters the single spectra depends on assumptions about its spatial distribution. Equation (I.34) shows that the leakage matrix depends on the mode's pattern on the surface of the Sun and on the applied spatial mask (i. e. spherical harmonic functions). If we assume that each mode is excited by a single component of the spherical harmonic decomposition of the noise,  $x_{l'}$  can be simply replaced by  $x_{l'} + c_{corr}$ , with a properly normalized correlated noise component  $c_{corr}$ , assuming that the correlated noise is strictly proportional to the excitation on the entire disk.

If we assume a wide range of horizontal wavelength components to be responsible for the excitation of a given mode, leakage should be treated differently. After calculating  $y_l^m$  using equation (C.1), the averaged spectrum is given by:

$$S_{av} = \sum_m |y_l^m + c_{corr}|^2, \quad (\text{C.3})$$

with a correlated noise component of constant amplitude and phase. This formula has been used for fitting the pseudomode spectra.





# Appendix D

## Optimal Masks

$x_i$  is the measured time series obtained from the pixel  $i$ , which is assigned to a coordinate  $(\Theta, \Phi)$ . It is modelled by a product of a time series  $c(t)$  and a spatial distribution  $y_i = y(\Theta, \Phi)$ , given by the eigenfunction of the expected mode:

$$x_i = c(t)y_i + \sigma_i\eta. \quad (\text{D.1})$$

$\sigma_i$  represents the given local noise level, and  $\eta$  is the stochastic error term, represented by a different realization for each pixel.

The time series  $c(t)$  minimizing the error can be obtained using linear regression. The global error is obtained by summing up over all pixels:

$$\sum_i |\eta|^2 = \sum_i \frac{|x_i - c(t)y_i|^2}{|\sigma_i|^2}. \quad (\text{D.2})$$

To obtain the minimum, we set the variation with respect to  $c(t)$  to zero:

$$\sum_i \frac{2(x_i - c(t)y_i)y_i^*}{|\sigma_i|^2} = 0, \quad (\text{D.3})$$

or,

$$c(t) = \frac{\sum_i x_i y_i^* / |\sigma_i|^2}{\sum_i |y_i|^2 / |\sigma_i|^2}. \quad (\text{D.4})$$

The mask  $M$  to obtain this time series is defined by:

$$c(t) = \sum_i M_i x_i, \quad (\text{D.5})$$

and is thus given by:

$$M_i = \frac{y_i^*/|\sigma_i|^2}{\sum_i |y_i|^2/|\sigma_i|^2}. \quad (\text{D.6})$$

# Appendix E

## Normalization of Optimal Masks

The velocity perturbation of a solar mode of oscillation of frequency  $\omega$  may be given by:

$$\mathbf{v} = \frac{D\sqrt{4\pi}\sqrt{2}}{\sqrt{1 + \frac{l(l+1)\omega_0^4}{\omega^4}}} \Re \left\{ \left[ Y_l^m \mathbf{e}_r + \frac{\omega_0^2}{\omega^2} \left( \frac{\partial}{\partial \Theta} Y_l^m \mathbf{e}_\Theta + \frac{1}{\sin \Theta} \frac{\partial}{\partial \Phi} Y_l^m \mathbf{e}_\Phi \right) \right] i\omega e^{i\omega t} \right\}, \quad (\text{E.1})$$

where  $\omega_0^2$  is  $MG/R^3$ .

The rms (root mean square) velocity of this mode, defined by:

$$\text{rms}(\mathbf{v}) = \sqrt{\frac{1}{4\pi} \int_S d\Omega \frac{1}{T} \int_0^T dt |\mathbf{v}|^2}, \quad (\text{E.2})$$

is given by:

$$\text{rms}(\mathbf{v}) = D\omega. \quad (\text{E.3})$$

The instrument's image of the mode is:

$$v = \mathbf{v} \cdot \mathbf{e}_x a \quad (\text{E.4})$$

where  $\mathbf{e}_x$  is the projection vector onto the line of sight, and  $a$  is the data apodization.

Let the mask function be defined by:

$$\tilde{Y}_l^m = \frac{\sqrt{4\pi}}{\sqrt{2}\sqrt{1 + \frac{l(l+1)\omega_0^4}{\omega^4}}} \left[ Y_l^m \mathbf{e}_r + \frac{\omega_0^2}{\omega^2} \left( \frac{\partial}{\partial \Theta} Y_l^m \mathbf{e}_\Theta + \frac{1}{\sin \Theta} \frac{\partial}{\partial \Phi} Y_l^m \mathbf{e}_\Phi \right) \right] \cdot \mathbf{e}_x a. \quad (\text{E.5})$$

The normalized mask is given by:

$$M = \frac{(\tilde{Y}_l^m)^*/\sigma^2}{\int_S |\tilde{Y}_l^m|^2/\sigma^2 d\Omega}, \quad (\text{E.6})$$

where  $\sigma^2$  is the spatial dependent variance of the noise. The integral may be taken over the whole surface of the Sun, because the apodization function has a nonvanishing value only at the visible portion of the Sun's surface.

A time series is obtained by applying the mask on the data, and integrating over the solar disk. In case of single mode time series without noise contribution, the corresponding time series is given by:

$$y(t) = \int_S d\Omega M v. \quad (\text{E.7})$$

Using the mask  $M$  given by equation (E.6) and the mode  $\mathbf{v}$  with rms velocity  $D\omega$  given by equation (E.1), we obtain, in case of a mode with tesseral order  $m = 0$ , a time series

$$y(t) = 2D\omega \sin(\omega t). \quad (\text{E.8})$$

In case of  $m \neq 0$ , the time series gets complex and is more difficult to denote. This, however, does not change the normalization of the mask.

For the MDI,  $y(t)$  is sampled on an equally distanced time grid  $t_j$ , with  $j = 0 \dots n - 1$ . The amplitude spectrum is defined by:

$$A(\omega) = \frac{1}{n} \left| \sum_{j=0}^{n-1} y(t_j) e^{-i\omega t} \right|. \quad (\text{E.9})$$

Hence, a mode of velocity  $\mathbf{v}$  with an rms displacement  $D\omega$  is reflected in a peak of height  $D\omega$  in the amplitude spectrum.

# Bibliography

- Abrams, D., & Kumar, P. 1996, ApJ, 472, 882
- Andersen, B. N. 1996, A&A, 312, 610
- Anderson, E. R., Duvall T. L., & Jefferies S. M. 1990, ApJ, 364, 699
- Appourchaux, T., et al. 1997, Sol. Phys., 170, 27
- Appourchaux, T., Gizon, L., & Rabello-Soares, M. C. 1998, A&A, 132, 107
- Appourchaux, T., et al. 2000, ApJ, 538, 401
- Berthomieu, G., & Provost, J. 1990, A&A, 227, 563
- Chaplin, W. J., & Appourchaux T. 1999, MNRAS, 309, 761
- Chaplin, W. J., Elsworth, Y., Isaak, G. R., Miller, B. A., & New, R. 2000, MNRAS 313, 32
- Charbonneau, P. 1995, ApJS, 101, 309
- Christensen-Dalsgaard, J. 1998, Lecture Notes on Stellar Oscillations, Aarhus Univ.
- Duvall, T. L., Jefferies, S. M., Harvey, J. W., Osaki, Y., & Pomerantz, M. A. 1993, ApJ, 410, 829
- Fossat, E. et al. 1992, A&A, 266, 532
- Fröhlich, C., et al. 1995, Sol. Phys., 162, 101
- Gabriel, A. H. et al. 1995, Sol. Phys., 162, 61
- Gabriel, A. H., et al. 2002, A&A, 390, 1119
- Georgobiani, D., Stein, R. F., & Nordlund, Å. 2003, ApJ, 596, 698
- Goldreich, P., & Kumar, P. 1990, ApJ, 363, 694

- Goldreich, P., Murray, N., & Kumar, P. 1994, *ApJ*, 424, 466
- Goode, P. R., Strous, L. H., Rimmele, T. R., & Stebbins, R. T. 1998, *ApJ*, 495, L27
- Gough, D. O. 1991, *A&ARv*, 29:627-84
- Haberreiter, M. & Schmutz, W. 1995, in *ISCS 2003 Symposium, Solar Variability as an Input to the Earth's Environment*, ed. A. Wilson (ESA SP-535, Noordwijk: ESA)
- Hamann, W. R., & Schmutz, W. 1987, *A&A*, 174, 173
- Hathaway, D. H., Beck, J. G., Bogart, R. S., Bachmann, K. T., Khatri, G., Petitto, J. M., Han, S., & Raymond, J. 2000 *Sol. Phys.*, 193, 299
- Jefferies, S. M., Severino, G., Moretti, P. F., Oliviero, M., & Giebink, C. 2003, *ApJ*, 596, L117
- Jiménez, A. 2004 (privat communication)
- Jiménez, A., Roca Cortés, T., Severino, G., & Marmolino, C. 1999, *ApJ*, 525, 1024
- Jiménez-Reyes, S. J., García, R. A., Jiménez, A., & Chaplin, W. J. 2003, *ApJ*, 595, 446
- Kosovichev, A. G. 1995, in *4th SOHO workshop: Helioseismology*, ed. J. T. Hoeksema, V. Domingo, B. Fleck, and B. Battrick (ESA SP-276, Noordwijk: ESA)
- Kosovichev, A. G., et al. 1997, *Sol. Phys.*, 170, 43
- Kosovichev, A. G. 1999, *JCoAM*, 109:1-39
- Kumar, P. 1994, *ApJ*, 428, 827
- Kumar, P., Quataert, E. J., & Bahcall, J. N. 1996, *ApJ*, 458, L83
- Kumar, P., & Basu, S. 1999, *ApJ*, 519, 389
- Kumar, P., & Basu, S. 1999, *ApJ*, 519, 396
- Nigam, R., & Kosovichev, A. G. 1998, *ApJ*, 505, L51
- Nigam, R.: *The Source of Solar Oscillations*, Ph.D. Thesis 1999 (Stanford University)
- Nordlund, Å., & Stein, R., F. 2001, *ApJ*, 546, 576

- Oliviero, M., Severino, G., Straus, T., Jefferies, S. M. & Appourchaux, T. 1999, ApJ, 516, L45
- Palle, P. L., et al. 1999, A&A, 341, 625
- Press, W. H., Flannery, B. P., Teukolsky, S. A., & Vetterling, W. T. 1986, Numerical Recipes (Cambridge: Cambridge Univ. Press)
- Provost, J., Berthomieu, G., & Morel, P. 2000, A&A, 353, 775
- Rasmussen, L. P.: Measuring Doppler velocities with the MDI, Ph.D. Thesis 1999 (Århus University)
- Rast, M. P., & Bogdan, T. J. 1998, ApJ, 496, 527
- Rast, M., P. 1999, ApJ, 524, 462
- Rimmele, T. R., Goode, P. R., Harold, E., & Stebbins, R. T. 1995, ApJ, 444, L119
- Roth, M., Howe, R., & Komm, R. 2002, A&A, 396, 243
- Scherrer, P. H., et al. 1995, Sol. Phys., 162, 129
- Schou, J.: On the analysis of Helioseismic Data, Ph.D. Thesis 1992 (Århus University)
- Schou, J., & Brown, T. M. 1994, A&AS, 107, 541
- Severino, G., Magri, M., Oliviero, M., Strauss, T. & Jefferies, S. M. 2001, ApJ, 561, 444
- Skartlien, R., & Rast, M. P. 2000 ApJ, 535, 464
- Stein, R., F., & Nordlund, Å., 2001, ApJ, 546, 585
- Stix, M. 1989, The Sun (Berlin: Springer Verlag)
- Title, A. M., Tarbell, T. D., Topka, K. P., Ferguson, S.H., Shine, R. A., & SOUP Team 1989, ApJ, 336, 475
- Toutain T., & Appourchaux, T. 1994, A&A, 289, 649
- Unno, W., Osaki, Y., Ando, H., & Shibahashi, H. 1989, Nonradial Oscillations of Stars (2ed.; Tokyo: Univ. Tokyo Press)
- van der Waerden, B. L. 1969, Mathematical Statistics (Berlin: Springer Verlag)
- Wachter, R., Schou, J., Kosovichev, A. G., & Scherrer, P. H. 2003, ApJ, 588, 1199



Wallace, L., Hinkle, K., & Livingston, W. 1998, An Atlas of the Spectrum of the Solar Photosphere from 13,500 to 28,000  $\text{cm}^{-1}$  (N.S.O Technical Report 98-001)

# Curriculum Vitae

born June 19, 1973 in Bobingen, Germany, grown up in Kleinaitingen.

## Education:

- 1979-1983 Primary school in Bobingen, Germany
- 1983-1993 Secondary school in Großaitingen, Königsbrunn, and Pfarrkirchen, Germany
- 1993-1994 Alternative civilian service in Würzburg
- 1994-2000 Basic and advanced studies in Physics at the University of Augsburg, Germany
- 2000-2004 Ph.D. student at the ETH Zürich, Switzerland, and at the PMOD/WRC (Physikalisch-Meteorologisches Observatorium Davos/World Radiation Center) in Davos Dorf, Switzerland